UNIVERSITY OF SOUTHAMPTON

FACULTY OF PHYSICAL SCIENCES AND ENGINEERING

Optoelectronics Research Centre

High-order harmonic generation with self-compressed femtosecond pulses

by

Patrick N. Anderson

Thesis for the degree of Doctor of Philosophy

February 2015

UNIVERSITY OF SOUTHAMPTON

ABSTRACT

FACULTY OF PHYSICAL SCIENCES AND ENGINEERING
Optoelectronics Research Centre

Doctor of Philosophy

HIGH-ORDER HARMONIC GENERATION WITH SELF-COMPRESSED FEMTOSECOND PULSES

by Patrick N. Anderson

Here, a state-of-the-art model is developed that can predict both the evolution of an intense laser pulse propagating through a gas-filled fibre, and the extreme ultraviolet field that it generates.

This model is first used to discover a new mechanism for compressing energetic laser pulses to few-cycle durations within short gas-filled fibres at pressures where high-order harmonic generation is routinely performed. Next, the fibre design is optimised for enhanced phase-matching using the model. Once fabricated and integrated into the source characterisation apparatus, the conversion efficiency at 30-40 nm is found to be almost an order of magnitude higher than comparable sources. Preliminary simulations also predict that isolated attosecond pulses may emerge from the fibre if parameters are carefully tuned.

Additionally, a 13.5 nm source is developed in an extended gas cell geometry. Filters suitable for this wavelength are tested and a single harmonic is then selected and brought to a focus. This apparatus is now being used by the wider scientific community to image test objects and biological samples.

Contents

List of Figures

List of Tables

List of Algorithms

Declaration of Authorship

I, Patrick N. Anderson , declare that the thesis entitled *High-order harmonic generation with self-compressed femtosecond pulses* and the work presented in the thesis are both my own, and have been generated by me as the result of my own original research. I confirm that:

- this work was done wholly or mainly while in candidature for a research degree at this University;
- where any part of this thesis has previously been submitted for a degree or any other qualification at this University or any other institution, this has been clearly stated;
- where I have consulted the published work of others, this is always clearly attributed;
- where I have quoted from the work of others, the source is always given. With the exception of such quotations, this thesis is entirely my own work;
- I have acknowledged all main sources of help;
- where the thesis is based on work done by myself jointly with others, I have made clear exactly what was done by others and what I have contributed myself;
- parts of this work have been published as: [4], [19], [3], [5], [18], [6], [46], [7]

Signed:.....

Date:.....

Acknowledgements

I would like to acknowledge the fantastic supervision and opportunities provided to me by Peter Horak and Bill Brocklesby.

Additionally, I would like to thank Jeremy Frey and Russell Minns for their enthusiasm and ideas, Tom Butcher and Richard Chapman for providing such a good introduction to the project, Aaron Parsons for all of his hard work keeping the laser system going and all of my friends in Southampton.

Nomenclature

BBO	Barium Borate
CCD	Charge-Coupled Device
CEP	Carrier Envelope Phase
CPA	Chirped Pulse Amplification
CXDI	Coherent X-ray Diffractive Imaging
EH	Electric Hybrid
FEL	Free Electron Laser
FFT	Fast Fourier Transform
FROG	Frequency Resolved Optical Gating
FWHM	Full Width Half Maximum
GRENOUILLE	Grating-Eliminated No-nonsense Observation of Ultrafast Incident Laser Light E-fields
HH	High-order Harmonic
HHG	High-order Harmonic Generation
HIO	Hybrid Input-Output
HT	Hankel Transform
HWHM	Half Width Half Maximum
IAP	Isolated Attosecond Pulse
IHT	Inverse Hankel Transform
MCP	Micro-Channel Plate
MM-GNLSE	Multimode-Generalised Nonlinear Schrödinger Equation
MPI	Multiphoton Ionization
NEE	Nonlinear Envelope Equation
NIR	Near Infra-Red
ODE	Ordinary Differential Equation
OPA	Optical Parametric Amplifier
OPCPA	Optical Parametric Chirped Pulse Amplification
ORC	Optoelectronics Research Centre
QPM	Quasi-Phase-Matching
RHS	Right-Hand Side
SAE	Single Active Electron

SFA	Strong Field Approximation
SHG	Second Harmonic Generation
SPM	Self-Phase Modulation
SSFM	Symmetrised Split-Step Fourier Method
SXR	Soft X-Ray
TDPM	Time-Dependent Phase-Matching
TDSE	Time-Dependent Schrödinger Equation
THG	Third Harmonic Generation
UPPE	Unidirectional Pulse Propagation Equation
UV	Ultraviolet
VIS	Visible
XUV	Extreme Ultraviolet
YAG	Yttrium Aluminium Garnet

Chapter 1

Introduction

Since the development of the laser by T. H. Maiman in 1960 [60], light sources with intensities sufficient to drive a nonlinear response within optical materials have become commonplace. Such a response is at the heart of nonlinear optics, a rapidly evolving field that has made it possible to dramatically alter the frequency of light, and accomplish incredibly efficient amplification schemes - to name just a few examples. Today, nonlinear frequency conversion is widely exploited to gain access to wavelengths where laser sources are not available or would be impractical.

One particularly lucrative wavelength region is the extreme ultraviolet (XUV, 10-120 nm) and soft x-ray (SXR, 0.1-10 nm), where numerous applications exist throughout the physical and biological sciences, including a fascinating microscopy technique known as coherent x-ray diffractive imaging (CXDI) [63, 80]. This computationally intensive technique removes the need for imaging optics altogether, and instead the sample is illuminated by a coherent XUV or SXR beam, its diffraction pattern collected and an iterative algorithm is called to reconstruct a high-resolution image of the sample. CXDI is beginning to supersede x-ray microscopes that rely on complex reflective and diffractive optics, and offers many advantages over conventional high resolution microscopy techniques. One such advantage is that high contrast images can be achieved by tuning the wavelength of the XUV or SXR beam to the absorption characteristics of the sample. An example of this, attracting particular interest from the biological sciences is the so called 'water window' shown in Fig. 1.1 (a) where 2-4 nm SXRs are strongly absorbed by carbon (due to the presence of the K-edge) but are transmitted by oxygen. A CXDI result obtained by myself is shown in Fig. 1.1 (c), however the methods and theoretical background required to obtain this example are beyond the scope of this thesis, where the focus will be the frequency conversion process itself.

In this introductory chapter the extension of optical nonlinear frequency conversion to XUV and SXR wavelengths is developed both chronologically and theoretically, and an outline of the results in this thesis is given.

(a)

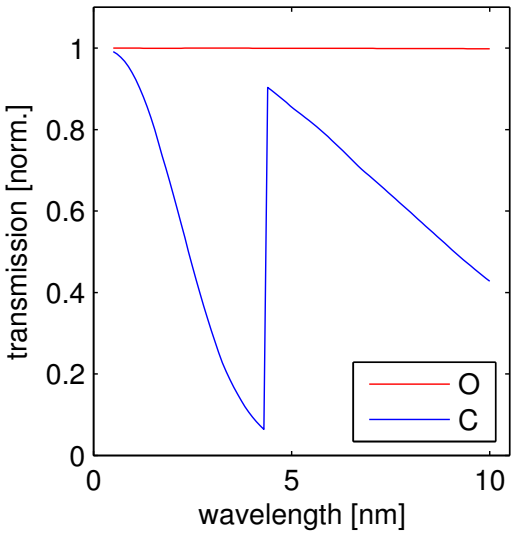

(b)

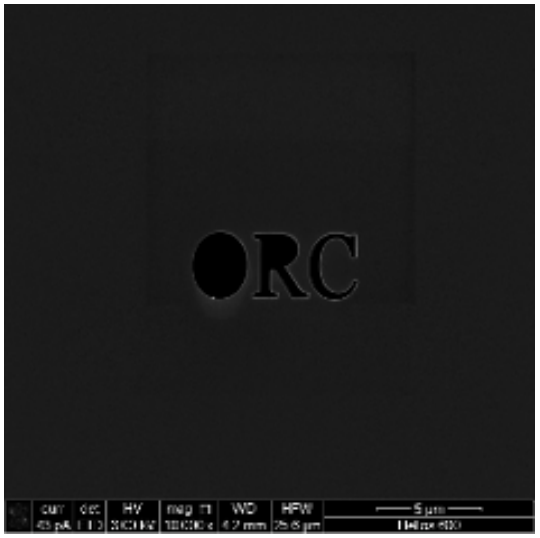

(c)

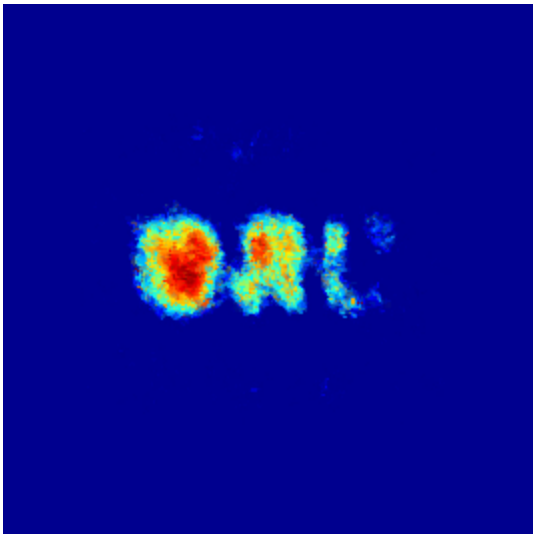

Figure 1.1: (a) The water window - a region of the SXR spectrum where carbon absorbs strongly and oxygen does not. This high contrast is an attractive property when imaging biological samples. (b) Scanning electron microscope image of a gold-coated silicon nitride membrane with the letters ORC removed by focused ion beam. (c) Corresponding CXDI result produced in a novel geometry where the test object is positioned far from the focus of a bright 29 nm beam.

1.1 SXR and XUV technologies

The majority of today's experiments requiring XUV and SXR wavelengths are performed at national facilities, where the electromagnetic radiation is generated within a synchrotron storage ring or free-electron laser (FEL), but the vast scale of these facilities makes them incredibly costly and access to visiting experimental scientists is often limited to as little as a few days each year. The high demand for these wavelengths has accelerated the development of a rival technique, which extends optical harmonic generation to give access to XUV and SXR wavelengths in a compact environment. This technique is known as high-order harmonic generation (HHG), and the experiment in its most basic form shares many similarities with frequency conversion at near infra-red (NIR, 700-1100 nm) and visible (VIS, 375-700 nm) wavelengths, however the extreme intensities required to drive HHG and strong material absorption in the SXR/XUV require the nonlinear crystal to be replaced with a low pressure atomic gas and the experiment to be enclosed by a vacuum chamber.

The road to the experimental demonstration of HHG was a long one, as the laser technology required to deliver optical intensities above 10^{13} Wcm^{-2} was simply not developed. Then in 1985 D. Strickland and G. Mourou demonstrated the chirped pulse amplification (CPA) scheme [85] and pulse intensities have grown ever since, long surpassing the requirements for HHG. Soon after, in 1988 HHG was observed in the laboratory by M. Ferray et al. [37], when a pulsed Nd:YAG laser with a peak intensity of 10^{13} Wcm^{-2} and a central wavelength of 1064 nm was used to generate 32 nm radiation in argon. Since this first observation ultrafast laser technology has advanced dramatically and compact laser systems capable of delivering NIR pulses with multi mJ energies and sub 30 fs pulse durations at kHz repetition rates are available commercially.

These advancements in technology have allowed research groups around the world to shift the envelope of harmonics to include wavelengths shorter than 1 nm [75] and achieve photon fluxes in the XUV comparable to a spatially filtered synchrotron light source [18]. Both of these enhancements build upon a particularly interesting geometry pioneered by the group of H. C. Kapteyn and M. M. Murnane, where HHG is restricted to a short section of hollow fibre [79]. For their first experiment a simple capillary type fibre with a core diameter of 150 μm and a 64 mm length was filled with $\sim$ 40 mbar of argon, and pulses from a Ti:sapphire oscillator-amplifier system tuned to 800 nm were launched into the fundamental mode supported by the fibre. The peak intensity of the driving laser was $\sim 2 \times 10^{14}$ Wcm^{-2} and a 20 fs pulse duration was maintained. The advantages of this scheme over existing HHG geometries has two parts, the first of these is an enhanced interaction length due to the waveguiding structure, but the second is more subtle. All coherent frequency conversion schemes are required to be phase-matched if they are to be efficient. This means the phase velocity of the driving pulses must match that of the harmonics, which in the case of HHG is usually forbidden due to

the chromatic dispersion of the medium. However, at low gas pressures and moderate intensities the fibre geometry sufficiently modifies the phase velocity of the driving laser to achieve phase-matching throughout the full length of the interaction region. This led to an increase in flux at $\sim$ 27 nm of between 2 and 3 orders of magnitude when compared with a more conventional geometry, and any further increases were limited by absorption.

Scaling this scheme to SXR wavelengths has proved challenging, as the extreme intensities required (10^{15} Wcm^{-2}) lead to non-negligible free electron densities, and this extra contribution to the chromatic dispersion spoils the phase-matching. Additionally, the free electrons modify the shape of the driving field in both space and time as it propagates along the fibre, further disrupting the simple phase-matching scheme. Two separate approaches have been suggested to tackle these problems, the first of which extends the quasi-phase-matching (QPM) technique to XUV and SXR wavelengths. The general principle of QPM is to turn HHG on and off periodically along the length of fibre so the HH field does not experience destructive interference as it builds up. As the free-electron density and harmonic order increase the distance over which this switching must occur becomes small, often 10^{-5} m or less if the harmonics are required to extend to the water window. QPM schemes confined to waveguides have included the modulation of the core diameter [69, 42], launching counter-propagating pulse trains [93], exploiting mode beating [92] and alternating the polarisation state [58]. Although enhancements in flux have been observed experimentally at XUV and SXR wavelengths, the QPM achieved is often imperfect due to the period being too long, or maintained over insufficient periods to surpass the flux of simpler time-dependent phase-matching experiments (TDPM).

TDPM will be studied in this thesis, and is the second approach to performing HHG efficiently at high intensities. This mechanism typically uses a driving pulse consisting of only a few optical cycles to generate the required HHs before the free electron density exceeds a certain threshold, below which absorption limited phase-matching is achievable. This technique can also be combined with a numerical study of the driving pulse propagation, to aid the stabilisation of spatio-temporal reshaping towards the exit of the fibre, and to incorporate a temporal self-compression scheme into the geometry. This approach has led to unprecedented flux in the XUV from conventional Ti:sapphire lasers [18], and the phase-matched generation of $\sim$ 0.4 nm harmonics when driving HHG with mid infra-red (MIR, 1100-10,000 nm) pulses [75].

In addition to their compact size HH sources are superior to synchrotron and FEL facilities when performing time-resolved measurements such as spectroscopy [82], and a long-term application of this technology is time-resolved CXDI, producing 'movies' of samples with unparalleled spatio-temporal resolutions. These enhancements are a result of the high temporal coherence and the ability to restrict HHG to an isolated burst [34], with a typical duration of several hundred attoseconds [44, 81]. These bursts represent

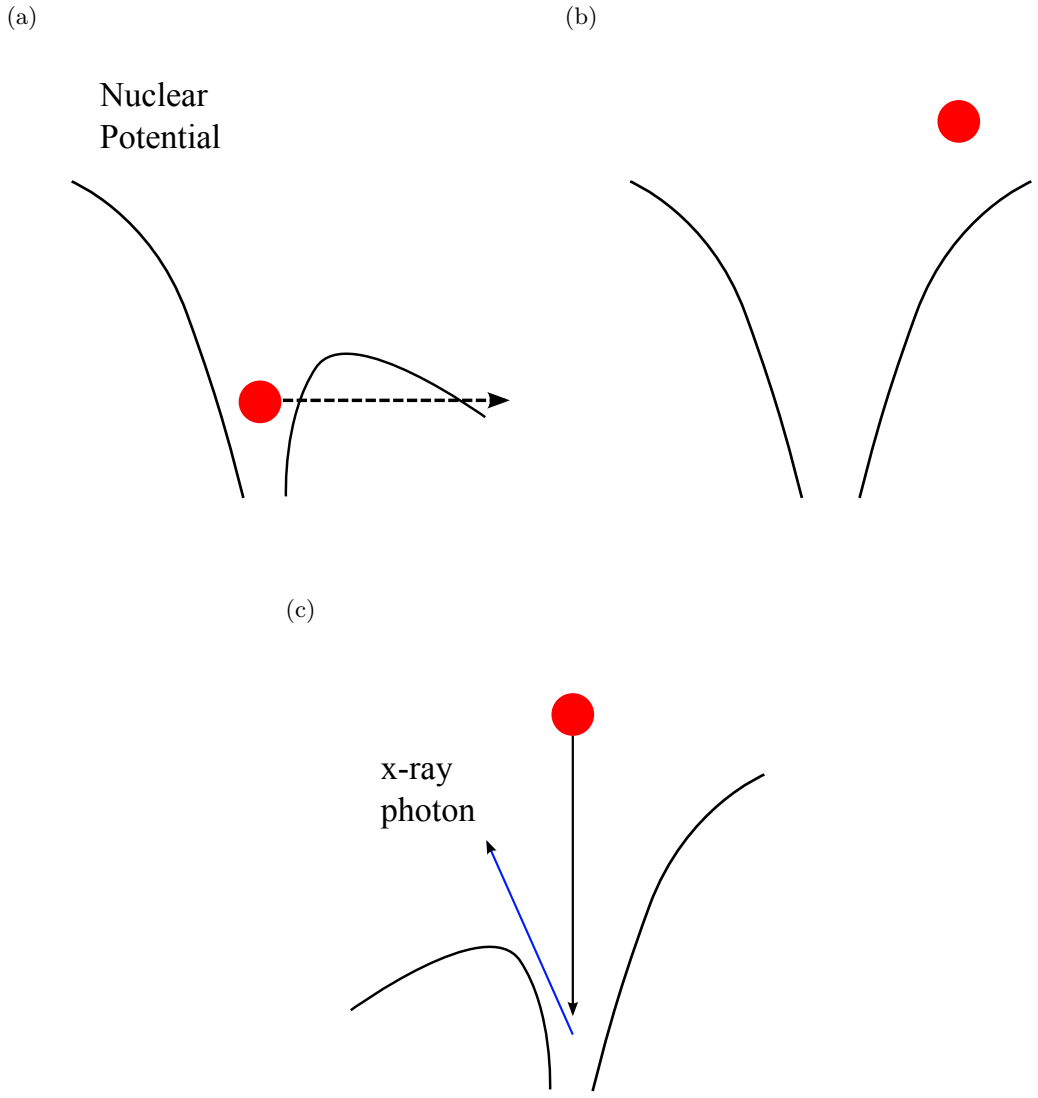

Figure 1.2: A simple semi-classical model of the HHG process. (a) The atom's nuclear potential is distorted by the strong laser field allowing tunnelling ionization to occur. (b) The free electron is then accelerated by the field increasing its kinetic energy. (c) As the field reverses the energetic electron may recombine with its parent ion emitting a soft x-ray photon.

some of the shortest events ever observed in the laboratory, and pulse durations below 100 as can be achieved by carefully manipulating the spectral phase [94]. The origins of these properties will be developed in the next section.

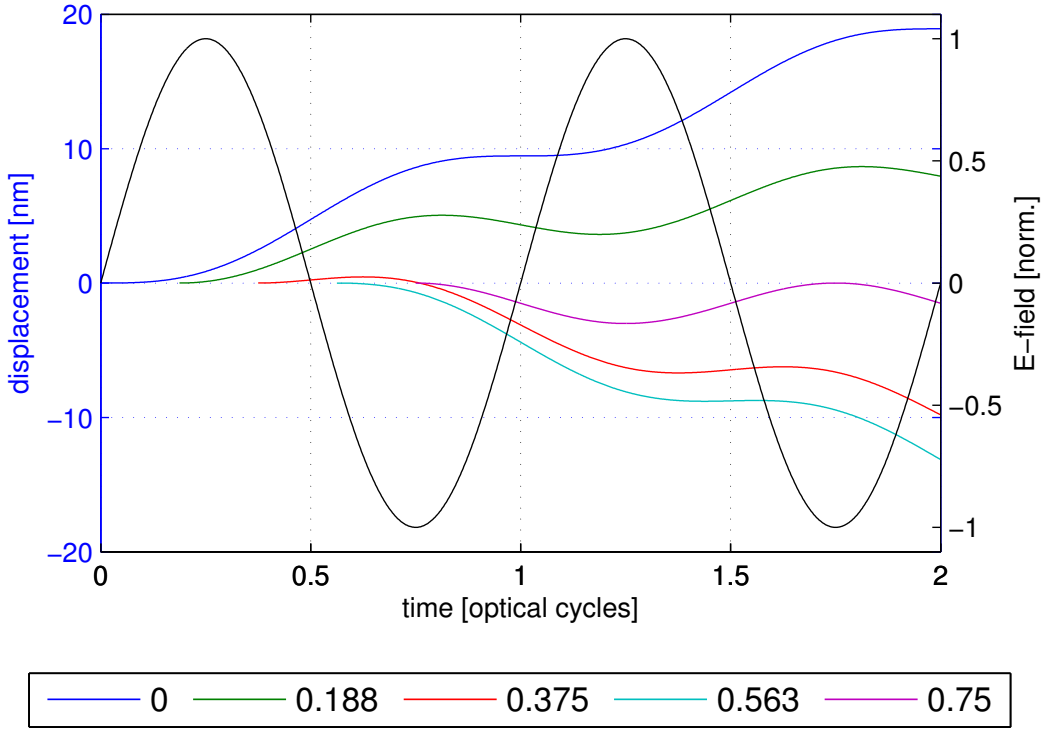

Figure 1.3: Classical analyis of free electron dynamics in a time dependent electric field (black curve). The 5 coloured curves show the trajectories taken by electrons freed at different times. This simple model begins to demonstate the origin of the attosecond bursts, as only electrons freed at ~ 0.3 optical cycles re-encounter the parent ion.

1.2 High-order harmonic generation

Several approaches are used throughout the literature to describe the origins of HHG, one of which is the semi-classical 'simple mans model' developed by P. B. Corkum [24]. More rigorous quantum mechanical models are developed in the next section, however this simple model will be used as an introduction because it allows for a straightforward description of HHG and some of its complexities. The three key stages of the model are illustrated in Fig. 1.2. In the first step, the time-dependent electric field interacting with the isolated atom must reach a strength sufficient to distort the nuclear potential and make ionization via tunnelling a likely outcome. Upon ionization the electron is considered to be free, and is accelerated away from the parent ion by the strong electric field. In the final step, the direction of the field reverses and the energetic electron may recombine with its parent ion, emitting radiation in the form of a high energy (XUV/SXR) photon. In addition to this qualitative description, important predictions can be made from a classical analysis of the dynamics of free electrons released into a strong linearly polarized electric field

$$E(t) = A\sin(\omega t), \tag{1.1}$$

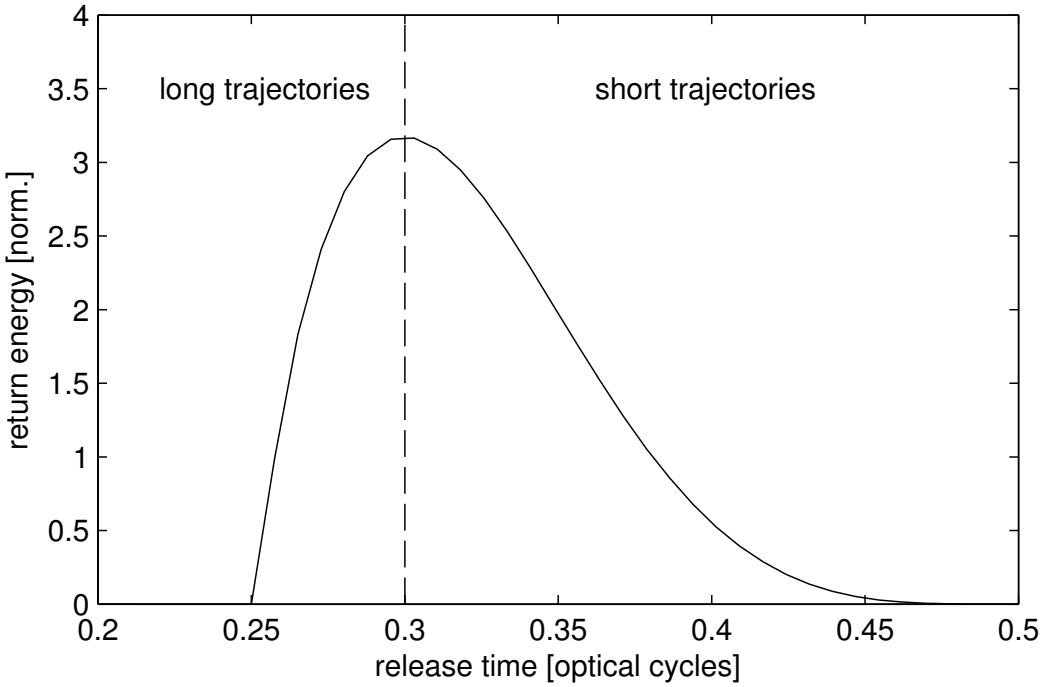

Figure 1.4: The return energies of electrons released at increasing times, as calculated by the classical model. The energies have been normalised with respect to U_p, and the peak of this curve explains the origin of the numeric coefficient in Eq (1.6).

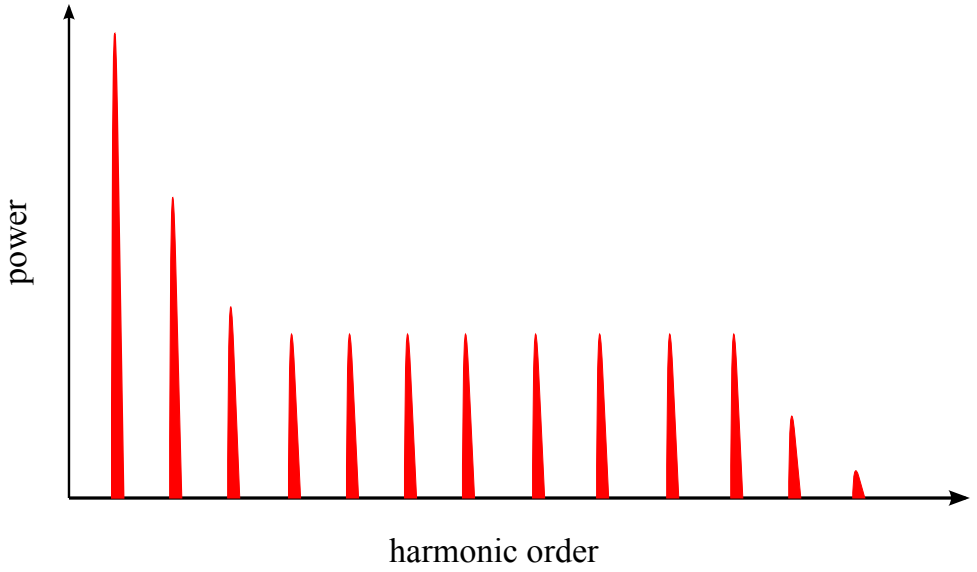

Figure 1.5: The characteristic HH spectrum. Note the three distinct parts: a perturbative section containing the low-order harmonics, a long plateau and an abrupt cut-off above which no further harmonics are generated.

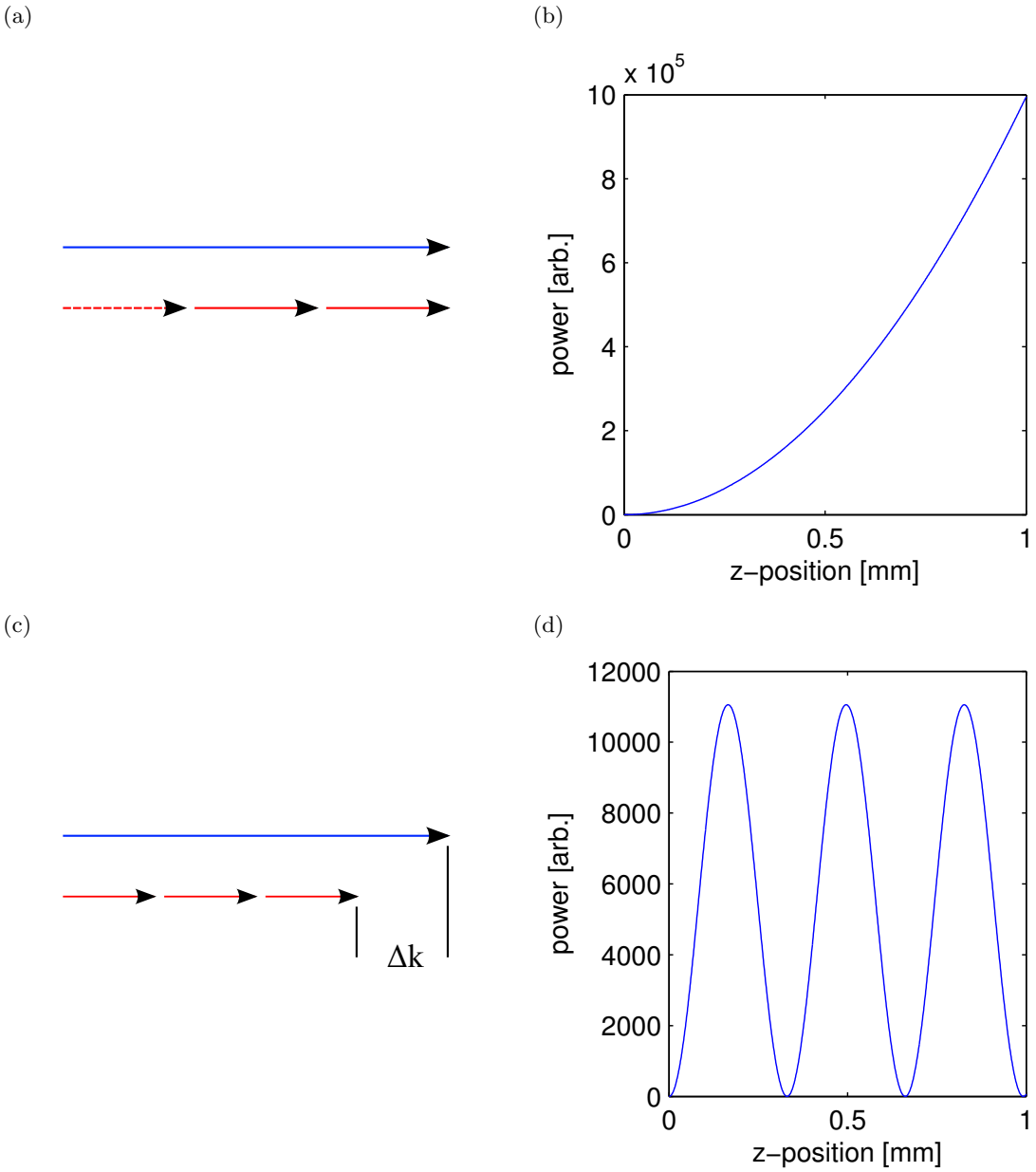

Figure 1.6: (a) The wavevector of the harmonic radiation (blue arrow) and driving laser (red arrows) when there is no mismatch. This leads to perfect phase-matching, and the quadratic increase in harmonic power with respect to propagation distance shown in (b). (c) and (d) The non-phase-matched case, resulting in the periodic oscillation of the harmonic power. Note that these illustrations are made in the absence of absorption which saturates the build up of harmonic power.

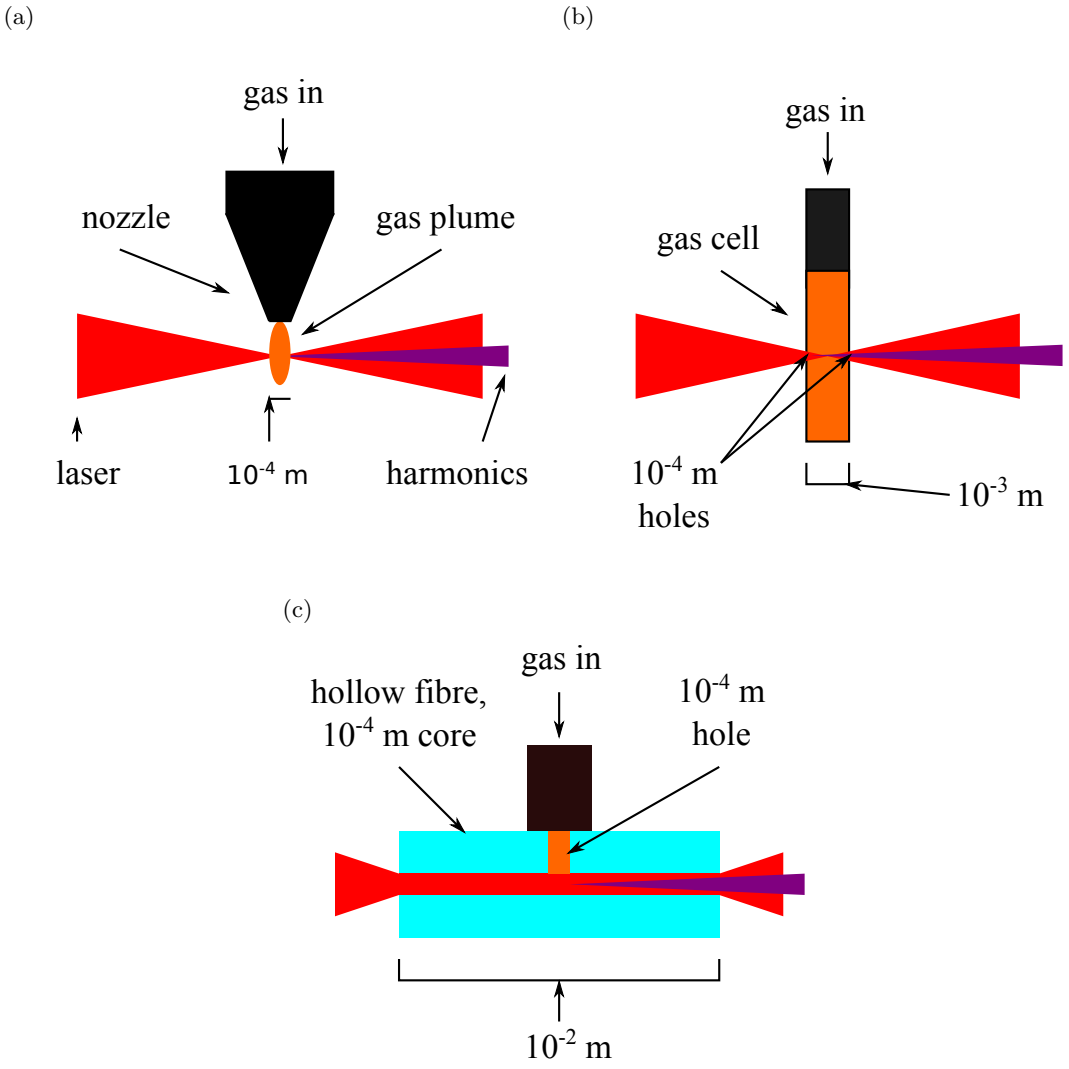

Figure 1.7: The conventional gas jet (a) and gas cell (b) geometries where a pressure regulated supply (often pulsed) is connected to a nozzle or cell placed within a vacuum chamber. Phase-matching limitations and short interaction lengths make the hollow fibre geometry (a) an attractive alternative.

where A is the field amplitude and ω is the angular frequency. Provided the electron velocity is 0 at release time t_0, and its position is 0 at both t_0 and return time t_1 the electron trajectories and return energies can be calculated as follows. Newton's second law gives the acceleration

$$\mathbf{a}(t) = \frac{eA}{m_e} \sin(\omega t), \tag{1.2}$$

where m_e and e are the electronic mass and charge. Integrating this once with respect to time gives the velocity

$$\mathbf{v}(t) = \frac{eA}{m_e \omega} \left[-\cos(\omega t) + \cos(\omega t_0) \right], \tag{1.3}$$

and a second integration gives the displacement

$$\mathbf{d}(t) = \frac{eA}{m_e\omega}\left[\left[\frac{1}{\omega}\left[-\sin(\omega t) + \sin(\omega t_0)\right]\right] + \left[t - t_0\right]\cos(\omega t_0)\right]. \tag{1.4}$$

Fig. 1.3 shows the electron dynamics for a series of release times, and evaluating the kinetic energy of the electron when it re-encounters the x-axis is a straightforward procedure, and is plotted as a function of release time and normalised to the pondermotive potential [16]

$$U_p = \frac{e^2A^2}{4m_e\omega^2} \tag{1.5}$$

in Fig. 1.4. Much of the physics observed in a HHG experiment is in fact recreated in these simple plots. The narrow time window where free electrons re encounter the parent ion gives rise to XUV/SXR radiation being emitted in a short burst, with a duration of several hundred attoseconds. In this continuous wave example (or for many-cycle laser pulses) extending the range of release times shows that these bursts are emitted twice per optical cycle, generating a pulse train whose frequency-domain representation consists solely of the odd harmonics of the driving field. This is consistent with what is observed experimentally, and a typical HH spectrum is illustrated in Fig. 1.5. The shape of this spectrum is interesting as it consists of three parts: a section containing the low-order harmonics, a long plateau of increasingly higher order harmonics and then an abrupt cut-off, above which no emission is observed. The location of this cut-off can also be deduced from the classical model and Fig. 1.4 in particular, where the maximum value describes the highest possible return energy. Adding this to the ionization potential I_p gives a simple expression for the position of the cut-off in terms of photon energy [54]

$$E_c = I_p + 3.17U_p. \tag{1.6}$$

This equation is reasonably accurate when compared with advanced models and experiments, and highlights the linear relationship between harmonic cut-off and the intensity of the driving laser. There are however several factors that restrict the intensities used to perform HHG, the most significant being phase-matching. Phase-matching allows HH radiation generated by separate atoms to combine coherently, provided that a fixed phase relationship can be maintained between the driving laser and harmonic field. This relationship can only be achieved when the mismatch between the wavevectors Δk is zero. This mismatch is given by [23]

$$\Delta k = k_h - qk_l, \tag{1.7}$$

where k_h is the wavevector of the q^{th} harmonic and k_l is the wavevector of the driving laser. Fig. 1.6 (a) shows these vectors when perfect phase-matching is achieved, and Fig. 1.6 (b) shows the corresponding quadratic growth in the power of the harmonic

field. Unfortunately, this is rarely achieved and the mismatch in Fig. 1.6 (c) causes an oscillation in the power of the harmonic field as it propagates through the gas (Fig. 1.6 (d)). Here, the maxima represent points at which the phase shift between the two fields exceeds π rad and they begin to interfere destructively. The distance up until this point is called the nonlinear coherence length L_c and is given by [23]

$$L_c = \frac{\pi}{\Delta k}. \tag{1.8}$$

This definition is an important one as it governs the maximum flux achieved by the majority of HHG sources, especially at SXR wavelengths where reabsorption losses are minimal. The first source of a non-zero Δk when performing HHG appears in Fig. 1.4, where two separate trajectories exist for each possible return energy. Those to the left-hand side of the peak are referred to as the long trajectories and those to the right-hand side are called the short trajectories. These trajectories interfere producing complex structure in the plateau of the single atom harmonic spectrum, and their relative phases are highly intensity dependent. The second and often dominant cause of poor phase-matching is the chromatic dispersion, and compensating for this has led to various geometries being explored. Conventionally HHG is carried out in either a gas jet (Fig. 1.7 (a)) or gas cell (Fig. 1.7 (b)). In these geometries a pulsed or continuous supply of gas is connected to a nozzle or cell within a vacuum chamber and the driving laser focused into them. One scheme, utilising the Gouy phase shift to enhance phase-matching throughout a small region close to the focus has gained popularity [57].

However, if phase-matching is to be achieved over a considerable length the hollow fibre geometry illustrated in Fig. 1.7 (c) should be used. As described in section 1.1, good phase-matching of XUV harmonics can be achieved in this geometry thanks to the appearance of the final term (describing modal dispersion) in the following wavevector

$$k(\lambda) = \frac{2\pi}{\lambda} + \frac{2\pi p(n_{gas}(\lambda) - 1)}{\lambda} + p\eta N_{atm} r_e \lambda - \frac{u_{11}^2 \lambda}{4\pi a^2}. \tag{1.9}$$

Here, λ is the wavelength, p is the gas pressure measured in atmospheres, n_{gas} is the refractive index of the neutral gas, η is the ionization fraction, N_{atm} is the number density measured at 1 atm, r_e is the classical electron radius, u_{11} is the first root of the zero order Bessel function of the first kind and a is the radius of the hollow core [79]. At moderate intensities the second term (describing chromatic dispersion) is the dominant source of phase mismatch, and because n_{gas} is typically just below 1 for XUV and SXR wavelengths the final term (describing modal dispersion) is correctly proportioned to restore phase-matching. If the intensity is increased this is no longer the case and the strong chromatic dispersion of the free electrons (third term) can lead to a very short L_c. As outlined in the next section tackling this problem is a major theme of this thesis.

1.3 Thesis outline

In chapter 2 a state-of-the-art numerical model is developed that is capable of predicting both the evolution of the driving pulse as it passes through a gas-filled fibre and the HH field that emerges. This model is relied on heavily throughout the remaining three chapters of this thesis.

Chapter 3 is focused on the development and characterisation of HHG sources in the laboratory. The first half of this chapter describes the gas-filled fibre beamline at the University of Southampton and procedures are outlined for processing, mounting and launching into the fibre before a simple source characterisation experiment is performed. The second half of this chapter describes the development of a 13.5 nm XUV source at the Artemis laser facility. The geometry used here is an extended gas cell, and interesting development work is done preparing the new apparatus for applications in CXDI.

Chapter 4 contains the penultimate piece of work. Here, a new mechanism for compressing energetic many-cycle laser pulses to few cycle durations within short gas-filled fibres is discovered. Experimental measurements are recorded in the far-field and compared to the theoretical predictions. The mechanism is then extended to novel wavelengths and towards pulses delivered by high repetition rate fibre lasers.

In chapter 5 (the final chapter excluding conclusions) this new self-compression mechanism is used to optimise the phase-matching achieved within a gas-filled fibre. The optimised design is then fabricated and its characterisation is compared to other published data. Finally, the temporal structure of the XUV emerging from these fibres is examined with the aim of synthesising an isolated attosecond pulse.

Chapter 2

Modelling HHG in gas-filled fibres with minimal approximation

This chapter describes the development of an advanced suite of numerical models capable of predicting the characteristics of XUV and SXR fields generated when intense laser pulses propagate through short gas-filled fibres. Such a system is challenging to model because of the multiple scales involved: both the macroscopic propagation of the optical field, and the microscopic (quantum mechanical) response of the gas are significant. Finding numerical solutions to the emerging Maxwell-Schrödinger system is inefficient, and simulations using this approach have (to date) been limited to interaction lengths of ~ 30 μm [59]. In order to extend this, a degree of approximation must be introduced into the *ab initio* model. These modifications and their implementation in code are the topic of the following section.

2.1 Medium response models

In this section models will be developed to describe the microscopic interaction between an intense optical field and a low pressure atomic gas. The standard model used for filamentation studies will be presented first, and then a quantum mechanical model that incorporates HHG will be constructed and results discussed. These models act as 'black boxes' that evaluate the nonlinear polarization $P_{NL}(t)$ and current density $J(t)$ as required by Maxwell's equations in subsequent sections.

2.1.1 The standard model

The 'standard' model for calculating how gasses respond to intense laser pulses has been developed by the filamentation community [26, 52]. This model allows for fast computations and in the following is specialised to a low pressure atomic gas.

2.1.1.1 Nonlinear polarization

An atomic gas is classified as a centrosymmetric medium with an instantaneous Kerr response, and the dominant nonlinear contribution to the polarization reads [16]

$$P_{NL}(t) = \epsilon_0 \chi^{(3)} E(t)^3, \tag{2.1}$$

where E is the electric field resolved at time t, ϵ_0 is the permittivity of free space and $\chi^{(3)}$ is the third-order nonlinear susceptibility of the gas. It is often helpful to replace this susceptibility with the experimentally measured nonlinear refractive index [16]

$$n_2 = \frac{3\chi^{(3)}}{4\epsilon_0 c n_0^2}. \tag{2.2}$$

Here, c is the vacuum velocity of light and n_0 is the linear refractive index of the gas. In this form Eq. (2.1) is the source of all the commonly observed third-order optical nonlinearities including self-phase modulation (SPM), self-focussing, third-harmonic generation (THG), etc. If THG is anticipated to be weak and fast numerical calculations are desired the real valued electric field in Eq. (2.1) should be replaced by [25]

$$E(t) = \frac{1}{2} A(t) e^{ik_0 z - i\omega_0 t} + c.c, \tag{2.3}$$

where $A(t)$ is the envelope of the electric field, k_0 the central wavevector, ω_0 the central angular frequency and $c.c$ denotes the complex conjugate. Once the term oscillating at the third harmonic is discarded Eq. (2.1) reads [25]

$$\mathcal{P}_{NL}(t) = \frac{3}{4} \epsilon_0 \chi^{(3)} \mid A(t) \mid^2 A(t). \tag{2.4}$$

This simplification holds for atomic gasses under the majority of conditions as THG is in fact poorly phase-matched. However, if extensive supercontinuum generation is predicted and computation times are not of great concern Eq. (2.1) should be used, as these conditions can enhance THG and related cascaded nonlinearities.

2.1.1.2 Current density

In chapter 1 HHG was introduced with the requirement that the electric field is sufficiently strong to ionize the gas within the intended interaction region. This leads to

a non-zero current density $J(t)$ appearing in Maxwell's equations, and an additional material response model is required to calculate $J(t)$ for an arbitrary field $E(t)$. The governing equation used for this purpose is [28]

$$\partial_t J(t) = -\frac{e^2 \rho(t) E(t)}{m_e} - \frac{J(t)}{\tau_c} - \epsilon_0 c \partial_t \left[\frac{\sum_q \left[\rho_q(t) W_q(t) U_q \right] E(t)}{\mid E(t) \mid^2} \right], \tag{2.5}$$

where e is the electron charge, m_e is the electron mass, τ_c is the collision time, ρ is the total free electron density $\sum_q [q\rho_q]$ and ρ_q, W_q and U_q represent the density, ionization rate and ionization potential of the q^{th} charge state of the gas. The three terms on the RHS of Eq. (2.5) describe different processes; the first term describes the acceleration of charge, the second accounts for collisional damping and the third is an effective term that will account for ionization induced losses once inserted into Maxwell's equations. The low gas pressures and short driving pulses used for HHG allow the second term to be neglected, as the collision time is large when compared to the duration of E. The

```
1: function CURRENT_MODEL(E(t), other)
2:                                                    ▷ solve Eq. (2.6)
3:     for each charge state q do
4:         W_q(t) = IONIZATION_RATE(E(t), q, other);
5:         if q = 0 then
6:             ρ_0(t) = EXP(-INTEGRATE(W_0(t)));
7:         else if q = Q then
8:             ρ_Q(t) = 1− SUM(ρ_0(t) to ρ_{Q−1}(t));
9:         else
10:            ρ_q(t) = EXP(-INTEGRATE(W_q(t)))
11:                    × INTEGRATE(W_{q−1}(t)ρ_{q−1}(t)
12:                    ×EXP(INTEGRATE(W_q(t))));
13:        end if
14:    end for
15:                                                   ▷ solve Eq. (2.7)
16:    evaluate B(t) and C(t);
17:    return IFFT(FFT((i/ω)B(t)) + ε_0 c FFT(C(t)));
18: end function
```

Algorithm 2.1: The efficient algorithm developed to calculate the current density $J(t)$ for a driving field $E(t)$. In the first part ionization rates and populations are calculated for the gas of interest. Here, the function INTEGRATE is a cumulative numerial integral with respect to time. The second part of the algorithm then solves for the current density by eliminating partial derivatives in the frequency domain.

densities of the various charge states are calculated using the rate equations [28]

$$\begin{aligned} \partial_t \rho_0 &= -W_0 \rho_0 \\ \partial_t \rho_q &= W_{q-1}\rho_{q-1} - W_q \rho_q \\ \partial_t \rho_Q &= W_{Q-1}\rho_{Q-1}, \end{aligned} \tag{2.6}$$

where Q represents the highest achievable electronic charge. To solve Eq. (2.5) it is helpful to apply the simplification discussed above and rewrite it as

$$\partial_t J(t) = B(t) + \epsilon_0 c \partial_t \left[C(t)\right], \tag{2.7}$$

where B and C form the coefficients. The partial differentials can be eliminated via the Fourier transform and (if necessary) $J(t)$ can be recovered by applying its inverse. Alg. 2.1 shows the black box developed to calculate $J(t)$ for an input $E(t)$ without calling a numerical ODE solver. For the first part of the algorithm analytic solutions are found for Eq. (2.6) by separation of variables and the integrating factor technique. The second part of the algorithm solves Eq. (2.7) in the frequency domain and returns its time domain counterpart. This approach has proved to be accurate, and is fast when compared to numerical ODE schemes.

2.1.1.3 Ionization rates

The final component required in the model is a method for calculating the rate at which the gas is ionized by the electric field. Several strong field ionization mechanisms are active throughout the parameter space where HHG is routinely performed. The most dominant of these is tunnel ionization, where ionization rates exceed those of multiphoton ionization (MPI) by an order of magnitude or more. Physically, this process occurs when the potential barrier of the atom (or ion) is distorted sufficiently by an external electric field that the electron can tunnel through it. L. Keldysh developed the framework used today for the theoretical study of strong field ionization [48, 76], deriving analytic expressions for the ionization rate valid at the various limits of [76]

$$\gamma = \frac{\omega\sqrt{2m_e U_p}}{eA_{peak}}, \tag{2.8}$$

where γ is the Keldysh parameter and A_{peak} is the peak electric field amplitude. Tunnel ionization is characterised by the limit $\gamma \ll 1$, and for the linearly polarized electric fields used to drive HHG the ionization rate is given by [76]

$$W(t) = \kappa^2 \sqrt{\frac{3}{\pi}} C_{\kappa l}^2 2^{2n^*} F(t)^{\frac{3}{2}-2n^*} e^{-\frac{2}{3F(t)}}. \tag{2.9}$$

The parameters are defined as follows:

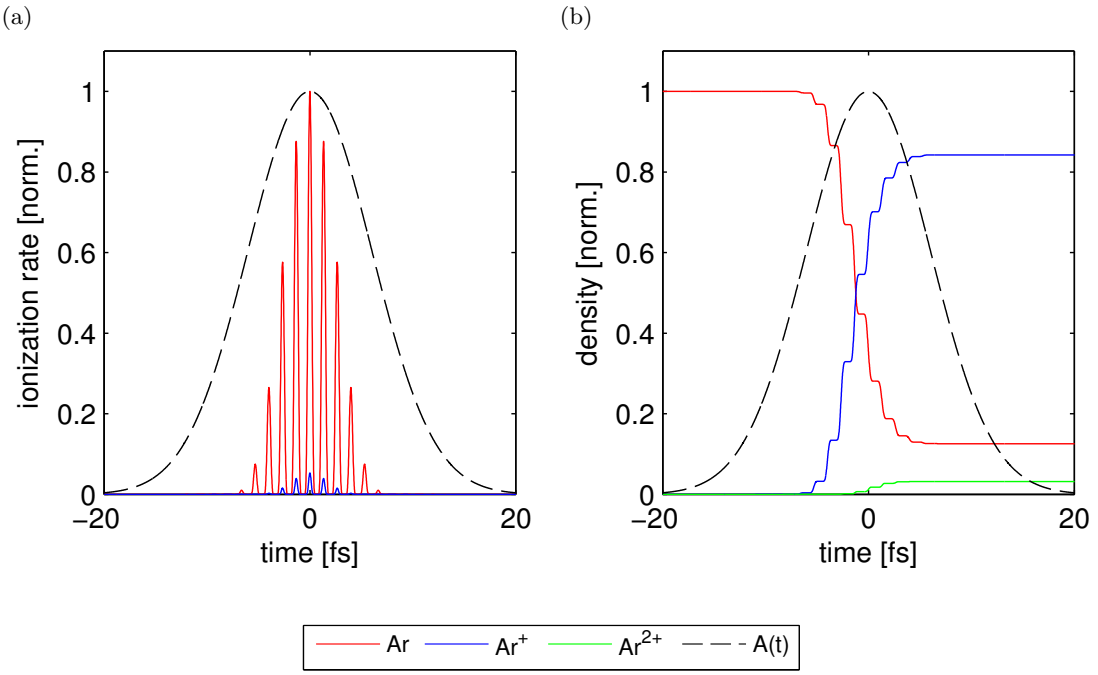

Figure 2.1: (a) The ionization rates of argon and its ions when driven by a strong laser pulse. These are calculated via Keldysh theory using a peak field intensity of 7.5×10^{14} Wcm^{-2}, an 800 nm wavelength and the pulse envelope illustrated by the black dashed curve. (b) The normalised time dependent densities of successive charge states. The strong field selected for this example leads to multiple sequential ionizations and a population of Ar^{2+} begins to build up.

- $\kappa = \sqrt{\frac{U_p}{U_h}}$, where U_p is the ionization potential of the species of interest and U_h is the ionization potential of atomic hydrogen.
- $C_{\kappa l}$ is a coefficient describing the asymptotic behaviour of the radial atomic wavefunction far from the nucleus. Such coefficients are species dependent and are listed in tabulated data [76].
- $n^* = \frac{q+1}{\kappa}$ is the effective principle quantum number, where q is the charge state of the species prior to ionization.
- $F(t) = \frac{E(t)}{\kappa E_a}$ is the reduced electric field, where E_a is the atomic unit for electric field.
- Finally, converting the ionization rate into SI units requires an additional coefficient equal to the atomic unit of frequency 4.13×10^{16} s^{-1}.

The nonlinearity of strong field ionization is demonstrated in Fig. 2.1 for an intense laser pulse interacting with an argon atom. The rapid variation in ionization rates and normalised populations above particular intensity thresholds is in fact the primary source of spatial and temporal reshaping of the E-field driving HHG in low pressure

gases. Eq. (2.9) provides an efficient method for calculating ionization rates, and unless stated otherwise it will be the implementation used within Alg. 2.1.

2.1.2 Advanced models

The nonlinear polarization model described in section 2.1.1.1 is not well suited to modelling HHG. To include this effect the starting point for developing a material response model is the time dependent Schrödinger equation (TDSE)

$$i\hbar\partial_t\psi(\mathbf{r},t) = H\psi(\mathbf{r},t), \tag{2.10}$$

where ψ is the wavefunction, H is the Hamiltonian operator, $\hbar$ is the reduced Plank constant and $\mathbf{r}$ is the spatial coordinate (x,y,z). This equation can describe the light-matter interaction completely, however the Hamiltonian describing the exact atomic system is routinely replaced by one that describes a 'model atom'. These simplified atoms facilitate the solution of Eq. (2.10) for HHG studies and typically involve a combination of the following: reductions in dimensionality, restricting the number of active electrons, the use of novel atomic potentials that yield exact solutions [17] and the widely used strong field approximation (SFA) [56]. The SFA was developed by M. Lewenstein et al. as a set of conditions that allowed P. B. Corkum's classical three-step model of HHG to be underpinned by quantum mechanics. Although this provides an efficient method for incorporating HHG into a material response model the HH spectra are inconsistent with the *ab initio* model throughout the harmonic plateau [40]. Much of the data generated in experiments originates from this region, so alternative approaches are needed if direct comparisons are to be made. The methods developed here use 1D model atoms to reduce the computational complexity of solving Eq. (2.10) directly. For the linearly polarized electric fields used in conventional HHG geometries this is a good approximation, and despite often overestimating the ionization rate, HH spectra compare favourably [78]. The model described below operates within the single active electron (SAE) approximation, and an efficient black box is presented for calculating $P_{NL}(t)$ from an arbitrary field $E(t)$.

2.1.2.1 The SAE approximation

The model used here is the 1D TDSE in atomic units, with a Hamiltonian reflecting the reduced dimensionality and a SAE [78]

$$\begin{aligned} i\partial_t\psi(x,t) &= H\psi(x,t) \\ &= \left[-\frac{1}{2}\partial_x^2 - \left[\frac{1}{\sqrt{\alpha+x^2}} + xE(t)\right]\right]\psi(x,t). \end{aligned} \tag{2.11}$$

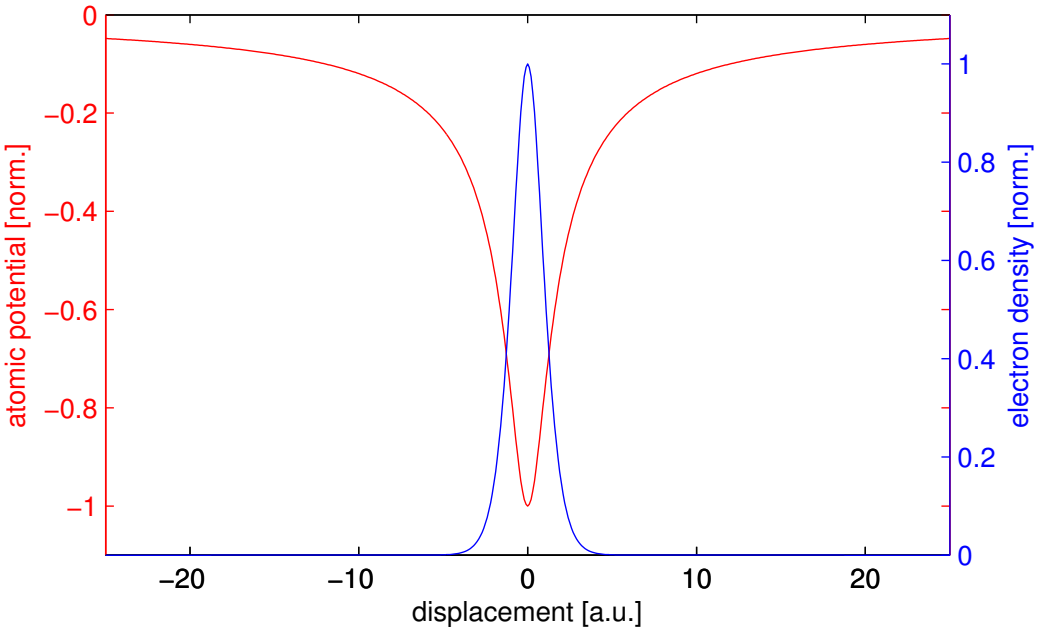

Figure 2.2: The normalised soft Coulomb potential (red curve) and ground state electron density (blue curve). In this example the parameter α has been adjusted so the energy of the ground state coincides with tabulated data for argon.

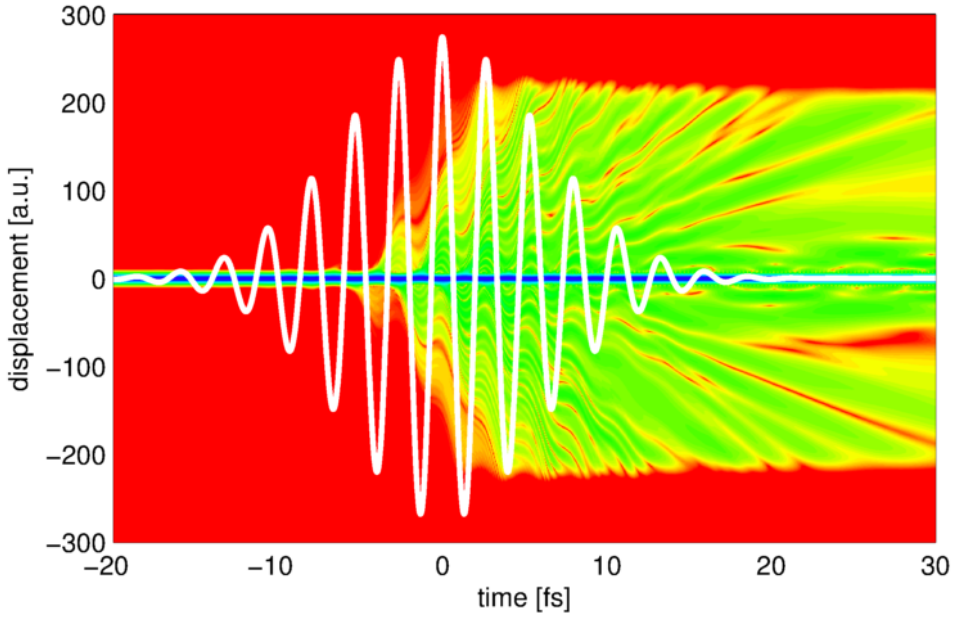

Figure 2.3: The electon density plotted as a function of time for a model argon atom interacting with the superimposed electric field (white curve). The driving pulse has a peak intensity of 1×10^{14} Wcm^{-2}, a 10 fs FWHM duration and a central wavelength of 800 nm.

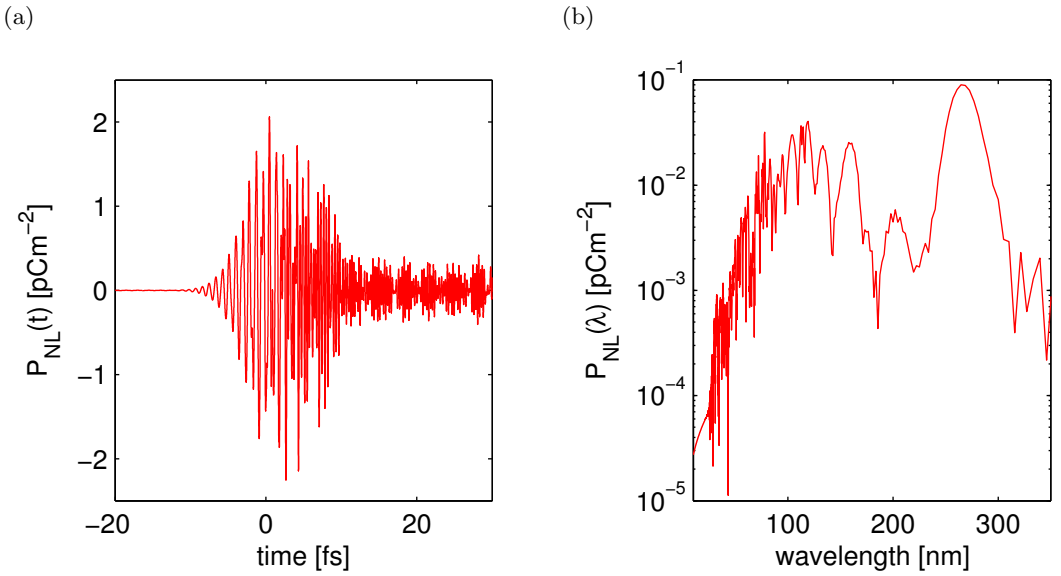

Figure 2.4: (a) The nonlinear polarization and its frequency representation (b) extracted from the SAE TDSE model (same parameters as Fig. 2.3). Both low and high-order harmonics are resolved by this material response model with a moderate efficiency.

Here, the Coulomb potential has been smoothed to reduce the influence of the singularity in 1D and enhance the stability of numerical solutions. The parameter α is close to 1, and can be scaled appropriately to match the energy of the ground state with tabulated data for the atom or ion being modelled. Various approaches can be used to solved Eq. (2.11) numerically including finite difference schemes like the Crank-Nicholson, however due to its elegance, efficiency and accuracy a symmetrised split-step Fourier method (SSFM) is developed here. To derive a discrete time propagator for the wavefunction over a step Δt, the starting point is the formal solution to Eq. (2.11) [32]

$$\psi(x, \Delta t) = e^{-iH\Delta t}\psi(x, 0). \tag{2.12}$$

---

initialisations;
for each time step Δt **do**
  calculate $V(x,t)$;
  $\phi(x) = \text{IFFT}(\text{EXP}(\frac{-iK(k)\Delta t}{2})\text{FFT}(\psi_{in}(x)))$;
  $\phi(x) = \text{EXP}(-iV(x,t)\Delta t)\phi(x)$;
  $\phi(x) = \text{IFFT}(\text{EXP}(\frac{-iK(k)\Delta t}{2})\text{FFT}(\phi(x)))$;
  $\psi_{out}(x) = \phi(x)B(x)$; ▷ apply absorbing boundaries
  $\psi_{in}(x) = \psi_{out}(x)$; ▷ update initial condition, calculate expectation values
end for

Algorithm 2.2: The SSFM implementation used to solve the 1D TDSE under the SAE approximation. This simple algorithm is efficient and can easily be extended to higher dimensions as required.

The aim of this and other operator splitting methods is to separate H such that its constituent parts can be applied in an efficient manner. For the TDSE this involves evaluating the potential part $V = \frac{1}{\sqrt{\alpha+x^2}} + xE(t)$ in real space and the kinetic part $K = \frac{1}{2}\partial_x^2$ in Fourier space, which eliminates the partial derivative from the Hamiltonian entirely. As K and V are noncommutative operators this splitting is not as straightforward as Eq. (2.12) first implies, and the Strang splitting formula is applied to obtain a propagator that is accurate to the second order [32]

$$\psi(x, \Delta t) = e^{\frac{-iK\Delta t}{2}} e^{-iV\Delta t} e^{\frac{-iK\Delta t}{2}} \psi(x, 0). \tag{2.13}$$

This is implemented in Alg. 2.2 where each propagation step is reduced to 4 fast Fourier transforms (FFTs) and 4 elementwise multiplications, including one with a window function $B(x)$ that imposes an absorbing boundary condition to limit any non-physical interferences. These operations are efficient to implement in code, and when compared to finite differences the elimination of the partial derivatives via the SSFM often allows for a sparser discretisation. It was found that simulations were convergent with a spatial window of $600a_0$ (where a_0 is the Bohr radius), 4096 spatial grid points and a time step of ~ 1 as. The final requirement to solve Eq. (2.11) is an initial condition. Here, this is chosen to be the ground state wavefunction, and can be calculated conveniently with Alg. 2.2 by setting $E(t) = 0$ and replacing the time step Δt with an imaginary one. Under these conditions an arbitrary 'seed' will relax into the ground state after a few hundred iterations, and the resulting electron density is shown in Fig. 2.2. Here, the process has been repeated for different α until the expectation value of the Hamiltonian matched the ground state energy of an argon atom. As a test, and to gain a quantum mechanical understanding of HHG, the interaction between an individual argon atom and a laser pulse with a 10 fs full width half maximum (FWHM) Gaussian envelope, a central wavelength of 800 nm and a peak intensity of 1×10^{14} Wcm^{-2} is simulated here. The resulting temporal evolution of the electron density $\psi\psi^*$ with the electric field driving the interaction superimposed is presented in Fig. 2.3. Examination of the leading edge of the pulse shows that as the optical field gains amplitude parts of the electron wave function tunnel through the distorted atomic potential and extend radially over many tens of atomic radii. As the optical field reverses the non-localized sections of the wavefunction collide with the bound section, leading to interferences and rapid oscillations in the electron density function. It is these oscillations that are the underlying source of HHG in the quantum picture of an atom interacting with a strong optical field. Various time dependent expectation values can be extracted from these simulations, and it is a topic of debate which is most appropriate for HHG studies. The dipole moment

$$d(t) = \int \psi(x,t) x \psi(x,t)^* dx \tag{2.14}$$

is the simplest of these, and factoring out the linear response and multiplying by $ea_0\rho_0(0)$, where a_0 is the Bohr radius yields the nonlinear polarization $P_{NL}(t)$ in SI units, as required by Maxwell's equations [17]. This and its Fourier transform $P_{NL}(\omega)$ are plotted in Fig. 2.4 (a) and (b) to demonstrate the inclusion of HHG in this advanced material response model. As the wavefunction describes the system completely, additional metrics describing the materials response to the field, such as $\rho_0(t)$ and $W_0(t)$ are simple to obtain as and when required.

2.2 Nonlinear pulse propagation

An intense optical field propagating through a non-magnetic dielectric is governed by Maxwell's curl equations

$$\nabla \times \mathbf{E}(\mathbf{r},t) = -\mu_0 \partial_t \mathbf{H}(\mathbf{r},t) \tag{2.15}$$

$$\nabla \times \mathbf{H}(\mathbf{r},t) = \epsilon_0 \partial_t [\epsilon(x,y,\tau) * \mathbf{E}(\mathbf{r},t)] + \partial_t \mathbf{P}_{\mathrm{NL}}(\mathbf{r},t) + \mathbf{J}(\mathbf{r},t) \tag{2.16}$$

and their corresponding divergence laws. Here, $\mathbf{H}$ is the magnetic field intensity, ϵ is the time domain representation of the frequency-dependent permittivity, and μ_0 is the permeability of free space. Vectorial quantities are highlighted with a bold typeface and the z coordinate points in the direction of propagation. In this section Eq. (2.15) and (2.16) are reduced to a z-propagated first-order nonlinear PDE system. These equations are then specialised to the gas-filled fibre geometry of interest and numerical methods are discussed.

2.2.1 General coupled-mode equation

The starting point for this derivation is to expand the optical field into a set of transverse spatial modes. The electric field for example becomes

$$\mathbf{E}(\mathbf{x},t) = \sum_{m,\omega} \left[A_m(z,\omega) \boldsymbol{\mathcal{E}}_m(x,y,\omega) e^{i\beta_m(\omega)z - i\omega t} \right], \tag{2.17}$$

where A_m is a complex spectral amplitude, $\boldsymbol{\mathcal{E}}_m$ is a transverse spatial mode function and β_m is a propagation constant - all of the m^{th} mode respectively. The summation extends over all M modes and Ω angular frequencies, and a similar expansion exists for $\mathbf{H}$. Following M. Kolesik and J. V. Moloney [51], Eq. (2.15) and (2.16) are multiplied

by the conjugate modal fields to produce

$$\begin{aligned}\boldsymbol{\mathcal{H}}_m(x,y,\omega)e^{-i\beta_m(\omega)z+i\omega t}\nabla\times\mathbf{E}(\mathbf{r},t) &= -\mu_0\boldsymbol{\mathcal{H}}_m(x,y,\omega)e^{-i\beta_m(\omega)z+i\omega t}\\ &\quad .\partial_t\mathbf{H}(\mathbf{r},t) \qquad (2.18)\\ \boldsymbol{\mathcal{E}}_m(x,y,\omega)e^{-i\beta_m(\omega)z+i\omega t}\nabla\times\mathbf{H}(\mathbf{r},t) &= \epsilon_0\boldsymbol{\mathcal{E}}_m(x,y,\omega)e^{-i\beta_m(\omega)z+i\omega t}\\ &\quad .\partial_t[\epsilon(x,y,\tau)*\mathbf{E}(\mathbf{r},t)]\\ &\quad +\boldsymbol{\mathcal{E}}_m(x,y,\omega)e^{-i\beta_m(\omega)z+i\omega t}\\ &\quad .[\partial_t\mathbf{P}_{\mathrm{NL}}(\mathbf{r},t)+\mathbf{J}(\mathbf{r},t)]. \qquad (2.19)\end{aligned}$$

To simplify notation the arguments will now be omitted and conjugate modal fields $\boldsymbol{\mathcal{E}}_m(x,y,\omega)e^{-i\beta_m(\omega)z+i\omega t}$ and $\boldsymbol{\mathcal{H}}_m(x,y,\omega)e^{-i\beta_m(\omega)z+i\omega t}$ will be re-written as $\boldsymbol{\mathcal{E}}_m^*$ and $\boldsymbol{\mathcal{H}}_m^*$. Again, following [51] Eq. (2.18) and (2.19) are first subtracted

$$\nabla[\mathbf{H}\times\boldsymbol{\mathcal{E}}_m^*]-\partial_t[\mu_0\boldsymbol{\mathcal{H}}_m^*\mathbf{H}]-\nabla[\mathbf{E}\times\boldsymbol{\mathcal{H}}_m^*]=\partial_t[\epsilon_0\boldsymbol{\mathcal{E}}_m^*\epsilon*\mathbf{E}]+\boldsymbol{\mathcal{E}}_m^*[\partial_t\mathbf{P}_{\mathrm{NL}}+\mathbf{J}], \quad (2.20)$$

and then integrated over then entire xyt domain to give

$$\partial_z\int\hat{\mathbf{z}}[\mathbf{H}\times\boldsymbol{\mathcal{E}}_m^*]dxdydt-\partial_z\int\hat{\mathbf{z}}[\mathbf{E}\times\boldsymbol{\mathcal{H}}_m^*]dxdydt=\int\boldsymbol{\mathcal{E}}_m^*[\partial_t\mathbf{P}_{\mathrm{NL}}+\mathbf{J}]dxdydt, \quad (2.21)$$

where $\hat{\mathbf{z}}$ is a unit vector. The above integration step is valid provided the fields vanish far from the optical axis, and at large past and future times [51]. Now, following [25] the modal expansion (Eq. (2.17)) is substituted into Eq. (2.21) and applying the orthogonality relation

$$\int\hat{\mathbf{z}}[\boldsymbol{\mathcal{H}}_m\times\boldsymbol{\mathcal{E}}_n^*-\boldsymbol{\mathcal{E}}_m\times\boldsymbol{\mathcal{H}}_n^*]dxdy=2\delta_{mn}N_m, \quad (2.22)$$

where N_m is a frequency dependent normalisation and δ_{mn} is the Kronecker delta, yields the general coupled mode equation

$$\begin{aligned}\partial_z A_m(z,\omega) &= -\frac{1}{2N_m(\omega)}\int\boldsymbol{\mathcal{E}}_m^*(x,y,\omega)e^{-i\beta_m(\omega)z+i\omega t}\\ &\quad\times[\partial_t\mathbf{P}_{\mathrm{NL}}(\mathbf{r},t)+\mathbf{J}(\mathbf{r},t)]dxdydt. \qquad (2.23)\end{aligned}$$

This equation is a powerful tool for developing nonlinear pulse propagation models encompassing optical filamentation in a bulk material [73], multimode nonlinear fibre optics [72] and nanophotonics [53]. In the next section Eq. (2.23) is specialised to the gas-filled fibre geometry of interest.

2.2.2 Pulse propagation equations for a gas-filled fibre geometry

Simplifying Eq. (2.23) requires the introduction of a set of analytic expressions approximating the mode functions supported by the waveguide. For the dielectric capillary-type

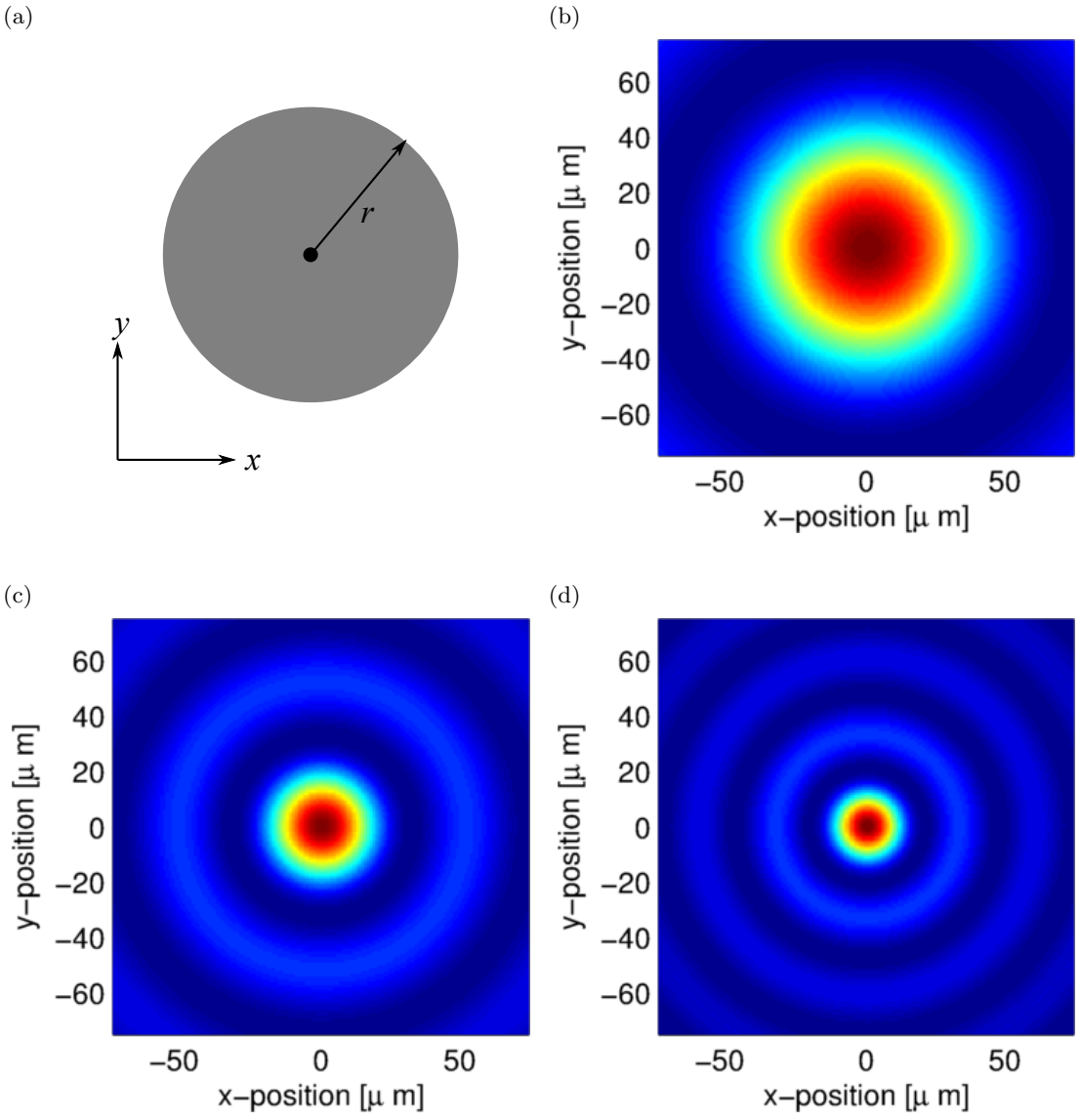

Figure 2.5: (a) The simple hollow capillary fibre. (b), (c) and (d) show the intensity profiles of the 3 lowest order EH_{1m} modes supported by the fibre. Due to the launch parameters selected these are the only modes that will be considered.

fibre shown in Fig. 2.5 (a) Marcatili and Schmeltzer [61] have constructed an orthogonal set of transverse electric, transverse magnetic and hybrid EH_{nm} modes. Of these only the EH_{1m} modes are linearly polarized, and it can be shown that a linearly polarized Gaussian beam is preferentially coupled into these modes under centred launch conditions. Additionally, if the waist of the waist of this Gaussian beam is manipulated to be $0.64a$ then optimal coupling is achieved and 98.1% of the power is transferred into the EH_{11} mode [65]. When the polarization axis of the electric field coincides with the

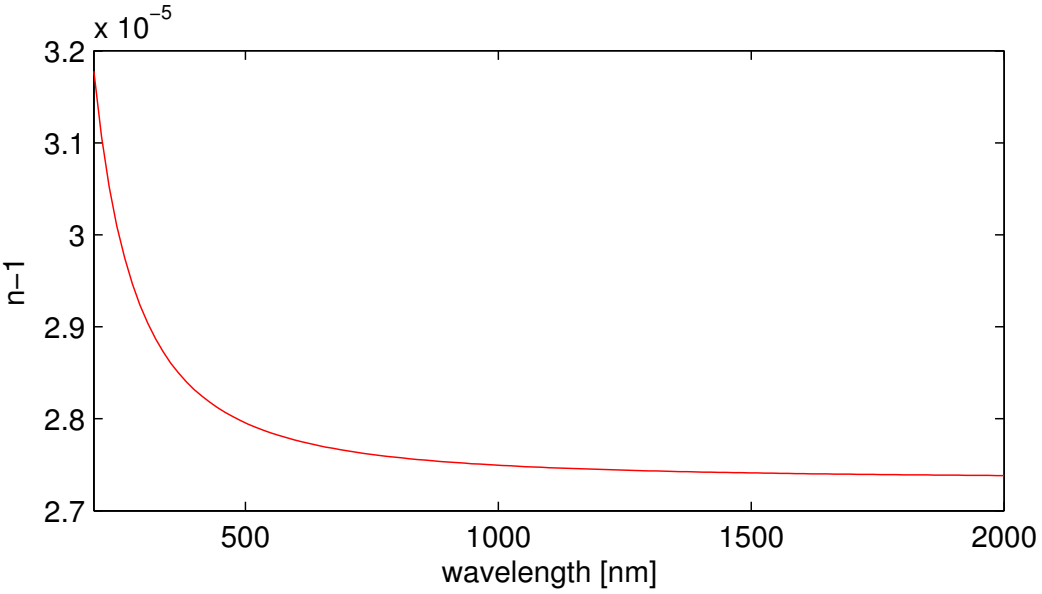

Figure 2.6: The refractive index of 100 mbar of neutral argon.

x-axis the mode functions are given by [61]

$$\mathcal{E}_{m,x} = J_0\left(\frac{u_m}{a}r\right) \tag{2.24}$$

$$\mathcal{H}_{m,y} = -\sqrt{\frac{\epsilon_0}{\mu_0}}\mathcal{E}_x, \tag{2.25}$$

where J_0 is the zero order Bessel function of the first kind, u_m are its roots and a is the radius of the core. The intensity distributions of the three lowest order modes are plotted in Fig. 2.5 (b), (c) and (d). For this geometry the modal propagation constants are [61]

$$\beta_m(\lambda) = \frac{2\pi n_{gas}}{\lambda}\left[1 - \frac{1}{2}\left[\frac{u_m\lambda}{2\pi a}\right]^2\right] + i\left[\frac{u_m}{2\pi}\right]^2\frac{\lambda^2}{a^3}\left[\frac{n_{glass}^2+1}{2\sqrt{n_{glass}^2-1}}\right]. \tag{2.26}$$

The real part describes both waveguide dispersion and the chromatic dispersion of the neutral gas. For wavelengths spanning the UV and MIR the refractive index of the neural gas n_{gas} is calculated with a Sellmeier equation. Using the coefficients given by Bideau-Mehu et al. [13] the refractive index of 100 mbar of argon is plotted as a function of wavelength in Fig. 2.6. Fig. 2.7 (a) shows the real part of the propagation constant as a function of wavelength and m for a 75 μm core radius. The imaginary part of Eq. (2.26) models the lossy nature of the modes. As the guidance mechanism consists of a series of grazing incidence reflections from a dielectric whose refractive index n_{glass} is typically ~ 1.45, light will leak from the core. Fig. 2.7 (b) demonstrates the loss properties of the fibre described above. The rapid increase in loss with m and restricting analysis to the dominant EH_{1m} modes leads to a very efficient implementation in code. In later sections this propagation constant will be modified and extended to XUV and

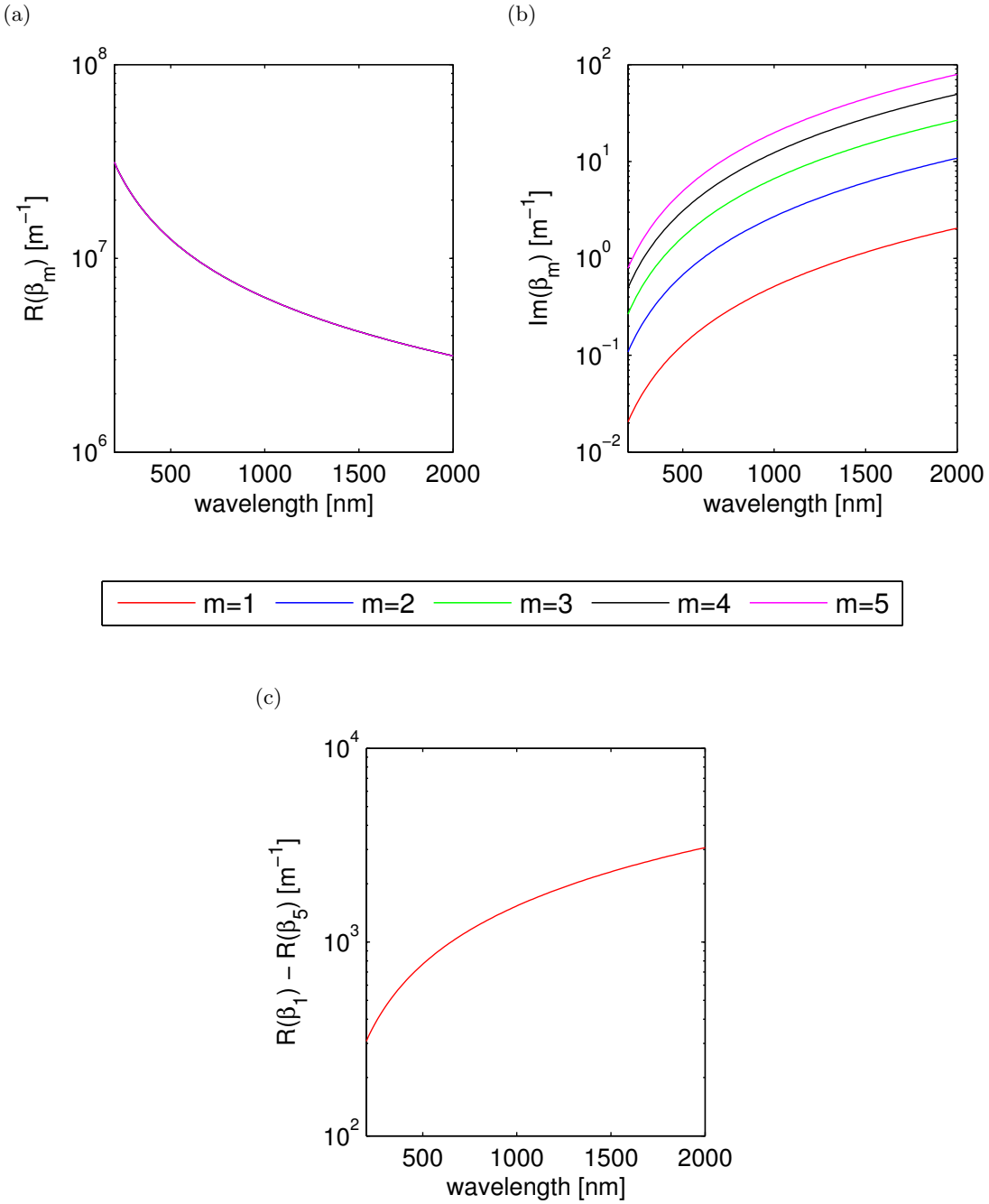

Figure 2.7: (a) The real part of the propagation constant plotted for the first 5 modes. The separation between the curves is difficult to resolve, so it is plotted separately in (c). (b) The imaginary part of the propagation constant which accounts for the lossy nature of the guiding mechanism.

SXR wavelengths. Now the fibre geometry and mode functions have been introduced a unidirectional pulse propagation equation (UPPE) can be derived. First, the mode functions Eq. (2.24 and 2.25) are inserted into the orthogonality relation Eq. (2.22) and transformed to cylindrical polar coordinates to give

$$N_m = 2\pi\sqrt{\frac{\epsilon_0}{\mu_0}}\int_0^a J_0\left(\frac{u_m}{a}r\right)^2 r dr. \tag{2.27}$$

This is a standard integral, and applying the limits yields

$$N_m = \pi\sqrt{\frac{\epsilon_0}{\mu_0}}a^2 J_1(u_m)^2, \tag{2.28}$$

where J_1 is the first order Bessel function of the first kind. Substituting Eq. (2.24) and (2.28) into the radially symmetric form of Eq. (2.23) and normalising the temporal integral with respect to a large window T gives

$$\partial_z A_m(z,\omega) = -\sqrt{\frac{\mu_0}{\epsilon_0}}\frac{e^{-i\beta_m(\omega z)}}{a^2 J_1(u_m)^2 T}\int_{-\frac{T}{2}}^{\frac{T}{2}}\int_0^a [\partial_t P_{NL}(z,r,t) + J(z,r,t)] \times J_0\left(\frac{u_m}{a}r\right)e^{i\omega t} r dr dt. \tag{2.29}$$

Here, the double integral and a portion of the denominator outside is the definition of the discrete spectral transform (Fourier in time and Hankel in space) of $\partial_t P_{NL}(z,r,t) + J(z,r,t)$, leading to one of the main results of this section

$$\partial_z A_m(z,\omega) = \sqrt{\frac{\mu_0}{\epsilon_0}}e^{-i\beta_m(\omega)z}\left[i\omega\tilde{P}_{NL}\left(z,\frac{u_m}{a},\omega\right) - \tilde{J}\left(z,\frac{u_m}{a},\omega\right)\right]. \tag{2.30}$$

The tilde and their arguments highlight that P_{NL} and J have undergone spectral transformation. When combined with the assumption that only the forward propagating field contributes to P_{NL} and J Eq. (2.30) becomes a unidirectional pulse propagation equation (UPPE), This approximation allows for an efficient numerical implementation, and its validity has been demonstrated for nonlinear pulse propagation studies in gases [50]. Introducing additional approximations into Eq. (2.23) allows various envelope equations to be derived, including the nonlinear envelope equation (NEE) confined to a gas filled fibre and the modified multimode generalised nonlinear Schrödinger equation (MM-GNLSE). In the case of the modified MM-GNLSE the material response model is introduced into Eq. (2.23) under the unidirectional approximation, and several frequency dependent arguments are neglected and introduced via empirical correction terms

instead. Using Peter Horak's definitions the modified MM-GNLSE is [21, 47]

$$\begin{aligned}\partial_z A_m(z,t) &= D_m + \frac{in_2\omega_0}{c}\left[1+\frac{i}{\omega_0}\partial_t\right]\sum_{jkl} Q_{mjkl}A_j(z,t)A_k(z,t)A_l(z,t)^* \\ &\quad -\frac{ie^2}{2c\epsilon_0 m_e\omega_0}\left[1-\frac{i}{\omega_0}\partial_t\right]\int \mathcal{E}_m(r)S(z,r,t)\rho(z,r,t)rdr \\ &\quad -\pi\int \mathcal{E}_m(r)S(z,r,t)\frac{\sum_q\left[\rho_q(z,r,t)W_q(z,r,t)U_q\right]}{\mid S(z,r,t)\mid^2}\,rdr. \end{aligned} \tag{2.31}$$

Here, D_m describes conventional dispersion and losses, Q_{mjkl} are mode overlap integrals, S is defined as $\sum[A_m(z,t)\mathcal{E}_m(r)]$, and the mode functions have been normalised so that $\mid S(z,r,t)\mid^2/2\pi$ has units of Watts. In the following chapters the modified MM-GNLSE will be used when carrier resolution is not required, as intuitive numerical solutions can be found more rapidly than for the UPPE.

2.2.3 Numerical methods

Considering the complexity of the system being modelled finding numerical solutions to the UPPE is fairly straightforward. Inspecting Eq. (2.30) shows that it is in fact a large system of ODEs coupled via the nonlinear source terms P_{NL} and J. The propagation over a longitudinal step Δz can therefore be accomplished by a function that evaluates the RHS and a call to an ODE solver. An additional modification is included in the practical implementation to allow for a moving frame of reference. The pseudocode for this is given in Alg. 2.3 and 2.4. The evaluation of the RHS of the ODE system for a small longitudinal step δz is accomplished by Alg. 2.3. The discrete Hankel transform is used to switch between the modal decomposition and the real space electric field,

```
1: function RHS(A(ω), δz, other)
2:     for each mode m do
3:         A_m(ω) = A_m(ω)EXP(i [β_m(ω) − ω/c] δz);
4:     end for
5:     E(r,t) = IFFT(IHT(A(ω)));
6:     P_NL(ω) = HT(FFT(POLARIZATION_MODEL(E(r,t), other)));
7:     J(ω) = HT(FFT(CURRENT_MODEL(E(r,t), other)));
8:     for each mode m do
9:         T_m(ω) = [iωP_NL,m(ω) − J_m(ω)]EXP(−i [β_m(ω) − ω/c] δz);
10:    end for
11:    return √(μ0/ε0) T;
12: end function
```

Algorithm 2.3: The algorithm developed to evaluate the RHS of the UPPE. Here, the functions HT and IHT perform the discrete Hankel transform and its inverse.

and the fast Fourier transform is used to alternate between the frequency and time domain. These transformations are required by the material response models. Alg. 2.4 is the main propagation loop and each iteration describes the propagation of the initial condition $A^{in}(\omega)$ over a distance Δz. The sophisticated numerical ODE solver used here has adaptive step-size control, allowing an error tolerance and large Δz to be specified. The procedure developed by Peter Horak to solve the modified MM-GNLSE is an operator splitting technique, and a pair of routines that share many similarities with Alg. 2.3 and 2.4. The modifications arise due to the nonlinear propagation step being performed in the time domain and the need to eliminate two time derivatives on the RHS of Eq. (2.31). The details of the software implementation, optimisation and performance will be discussed in section (2.4).

2.3 HH field propagation

If the fully quantum mechanical material response models developed in section 2.1.2 are used to calculate the source terms in the UPPE the generation of the HH field is included directly in the propagation model. The only modification required in this case is the extension of the propagation constants to XUV or SXR wavelengths. This approach is not used here because when the UPPE is solved the nonlinear source terms must be evaluated sequentially in the z-direction, and the lack of parallelism in this dimension leads to unworkable computation times when propagating over distances of 1-100 mm, even on the world's largest supercomputers. Additionally, the huge bandwidth and low divergence of the HH field increases the number of active frequency samples and 'modes' dramatically leading to an inefficient propagation. To get around these inefficiencies, frequencies generated that are higher than the TH are assumed to be weak and not drive the nonlinear source terms. This assumption allows the propagation to be performed as follows: The strong driving field is propagated via the UPPE using the standard material response model (2.1.1) over a number of z-steps to give $E(r, z, t)$; the quantum mechanical material response $P_{NL}(r, z, t)$ is calculated from this and used

1: initialisations;
2: **for** each longitudinal step Δz **do**
3: $A^{out}(\omega) =$ ODE_SOLVER(RHS, Δz, $A^{in}(\omega)$, options);
4: **for** each mode m **do**
5: $A_m^{out}(\omega) = A_m^{out}(\omega)\mathrm{EXP}\left(i\left[\beta_m(\omega) - \frac{\omega}{c}\right]\Delta z\right)$;
6: **end for**
7: $A^{in}(\omega) = A^{out}(\omega)$; ▷ update initial condition
8: **end for**

Algorithm 2.4: The algorithm used to propagate the field along the length of the fibre in steps of Δz.

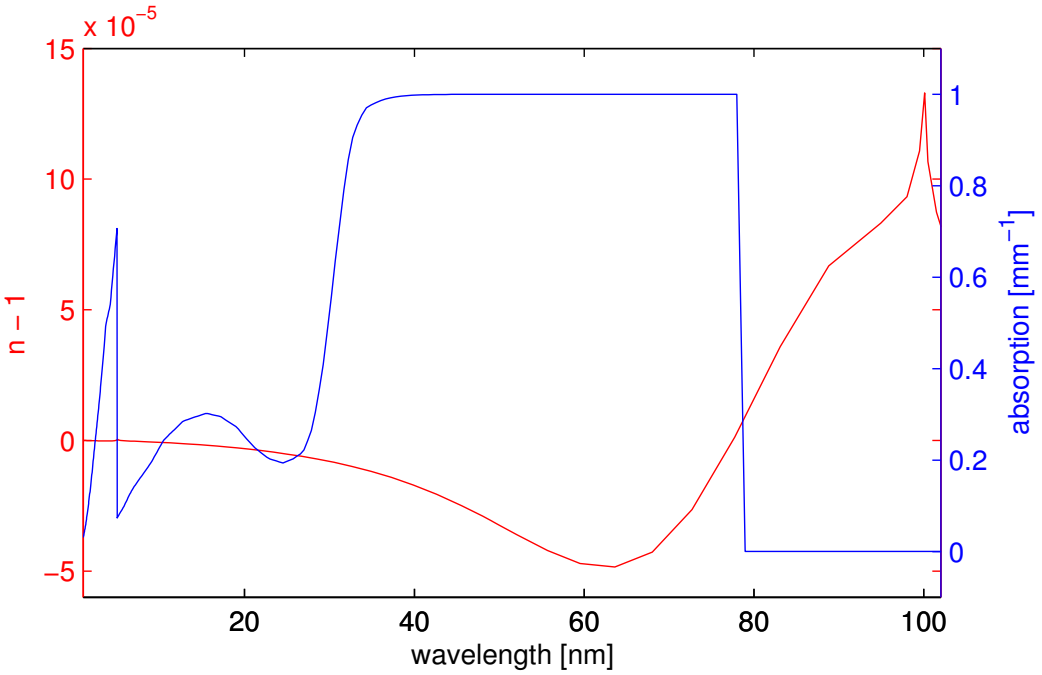

Figure 2.8: An illustration of the refractive index and absorption of 100 mbar of argon in the SXR and XUV. The refrctive index is < 1 for wavelengths < 70 nm and the absorption is very strong throughout much of the region.

in a second propagation equation restricted to a conservative XUV/SXR bandwidth. The final requirement in the model is knowledge of the frequency dependent complex propagation constant at XUV and SXR wavelengths. Unlike in the VIS and MIR, at short wavelengths the chromatic dispersion and linear absorption of the neutral gas dominate dispersion or loss caused by waveguiding. This is included via the complex refractive index [43, 30]

$$n_{gas}(\lambda) = 1 - \left[\frac{\rho_0(0) r_0 \lambda^2}{2\pi}\left[f_1(\lambda) + i f_2(\lambda)\right]\right], \tag{2.32}$$

where r_0 is the classical electron radius, and f_1 and f_2 are the real and complex parts of the atomic scattering factors [43]. These factors are a wavelength dependent quantity extracted from photoabsorption measurements. The refractive index and absorption coefficient of 100 mbar of argon is plotted in Fig. 2.8 for the entire XUV and SXR region.

2.4 Computational implementation and model validation

Now the final form of the model has been described, its computational implementation can be discussed. Performance was a key consideration in the design process and the software was developed with conventional cluster hardware in mind. However, optimisation did not supersede the development of a highly modular code leading to the adoption of

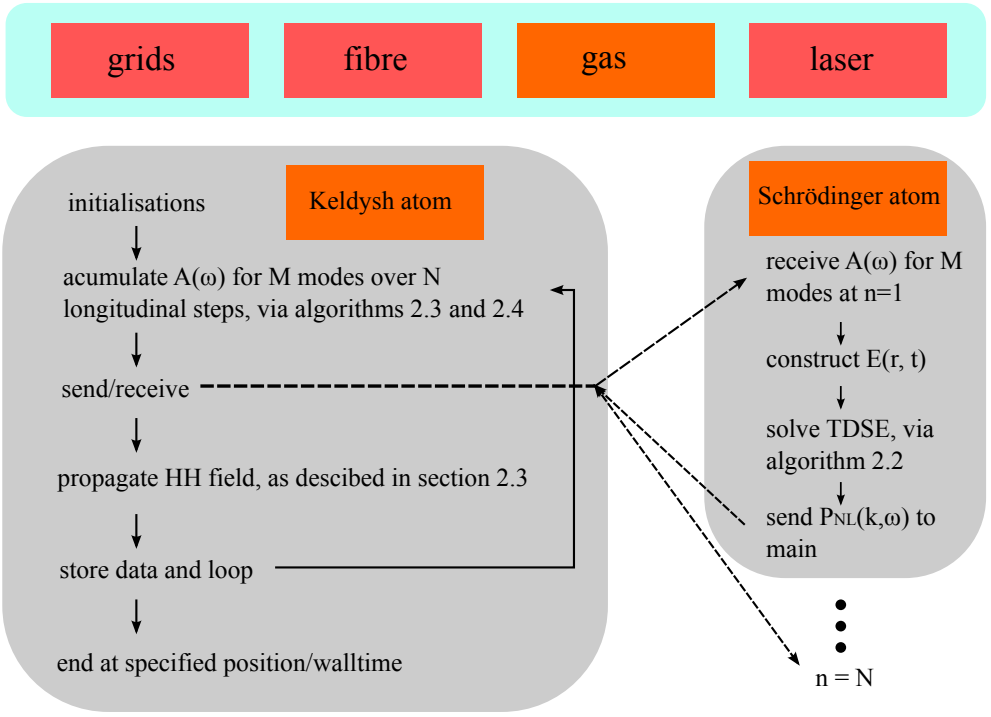

Figure 2.9: The structure of the program developed to solve the UPPE-TDSE model. Sophisticated object orientated and parallel programming were used to create a flexible, high-performance tool.

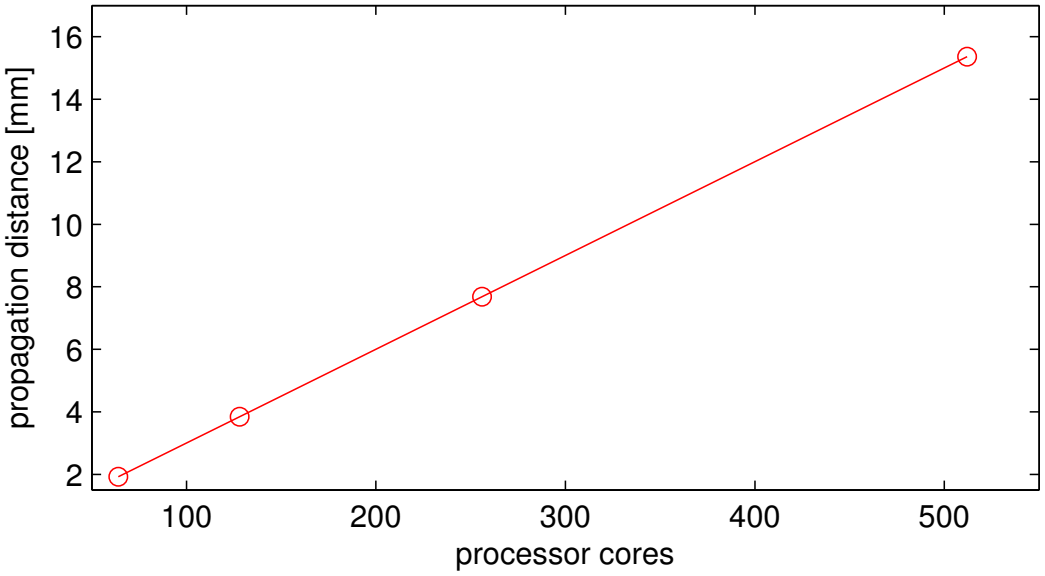

Figure 2.10: The propagation distance achieved in 10 hours as a function of the number of processor cores. The parameters used here are in-line with those used in the following chapters.

the object-orientated programming paradigm. When modelling physical systems object-orientation allows the properties and physics associated with various components to be encapsulated within 'objects'. Fig. 2.9 shows the key objects required in the HHG model, and these are interacted in the 'main' part of the program as described in the previous sections and the specified data is produced. The advantage of using objects becomes apparent when the system being modelled is modified. An example of this is the convenience at which the gas or fibre can be exchanged for another, requiring only 1 line of code to be changed. This functionality will be used extensively in chapters 3, 4 and 5. The C++ programming language was chosen for the final implementation because of its speed, object-oriented support and the ease at which standard C libraries (MKL, FFTW, GSL, etc.) can be called upon for numerics and parallelisation when required. The eigen template library was used heavily for linear algebra and vectorised mathematical operations. It was commented on in section 2.3 how parallelisation is implemented in the model and Fig. 2.9 shows this diagrammatically. The spectral amplitudes are stored at a series of z-positions and distributed to a group of 'workers' using the message passing interface. These workers perform the intensive quantum mechanical calculations and return the results to the main process for propagation. Further parallelisation strategies have been explored but a limit of ~ 500 processors per run leads to difficulties. The performance of the program is shown in Fig. 2.10. The propagation distance achieved with a 10 hour walltime is plotted as a function of processors. The parameters used here are consistent with HHG experiments, and to my knowledge the many mm of propagation achieved make this the most sophisticated tool developed to study HHG in gas-filled fibres to date. Extracts from the code have been made available on GitHub (GitHub, inc.) [2].

The modular nature of the program (shown in Fig. 2.9) is also helpful for locating and fixing any errors introduced during the during the development stage. The various elements of the program were tested individually against published or experimental data before they are 'connected' together to form the UPPE-TDSE model. Two key examples of this are the Schrödinger atom module being verified against the results of S. Rae and co-workers [78], and as will be seen in chapter 4 the validation of the UPPE model with respect to experimental measurements.

2.5 Conclusions and outlook

In this chapter a sophisticated model was developed that is capable of predicting the output of a fibre based HH source. This model combines a state-of-the-art UPPE with the TDSE and propagation over several mm is achieved by de-coupling the driving and harmonic fields to increase the number of computations that can be performed in parallel. This model (and its various constituent parts) are used throughout this thesis with much success.

The future development of this model is focused on adding a feedback step between the TDSE calculations and the simplified medium response model used by the UPPE. This will enable almost *ab initio* calculations to be carried out.

Chapter 3

Develoment and analysis of laboratory HHG sources

This chapter describes the apparatus and experimental methods used to generate and characterise high harmonics in the laboratory. In the first section the gas-filled fibre geometry is discussed and the harmonic field emerging from a 7 cm length of fibre analysed. The measured XUV spectra are then compared to their theoretical counterpart and the complex spatio-temporal structure is found to be imprinted onto the harmonic beam as a consequence the spatial and temporal structure of the driving pulse. The second section focuses on the development of a 13.5 nm source at Artemis (an open access laser facility at the Rutherford Appleton Laboratory). Here, an extended neon gas cell is used and 13.5 nm XUV is successfully monochromated and brought to a focus for applications in CXDI.

3.1 Short gas-filled fibres

This section describes the ongoing development of the gas-filled fibre beamline at the University of Southampton. The fibre preparation, installation and launch will be described in detail before discussing the XUV diagnostics and analysing the results of a source characterisation experiment.

3.1.1 Ti:sapphire oscillator-regenerative amplifier system

A schematic of the University of Southampton laser system used throughout this thesis is given in Fig. 3.1. At its heart is a compact Ti:Sapphire regenerative amplifier (Spectra Physics, Spitfire Pro) utilising a CPA scheme to deliver 3 mJ pulses with 40 fs durations at a repetition rate of 1 kHz. The seed for this amplifier is a modelocked Ti:Sapphire

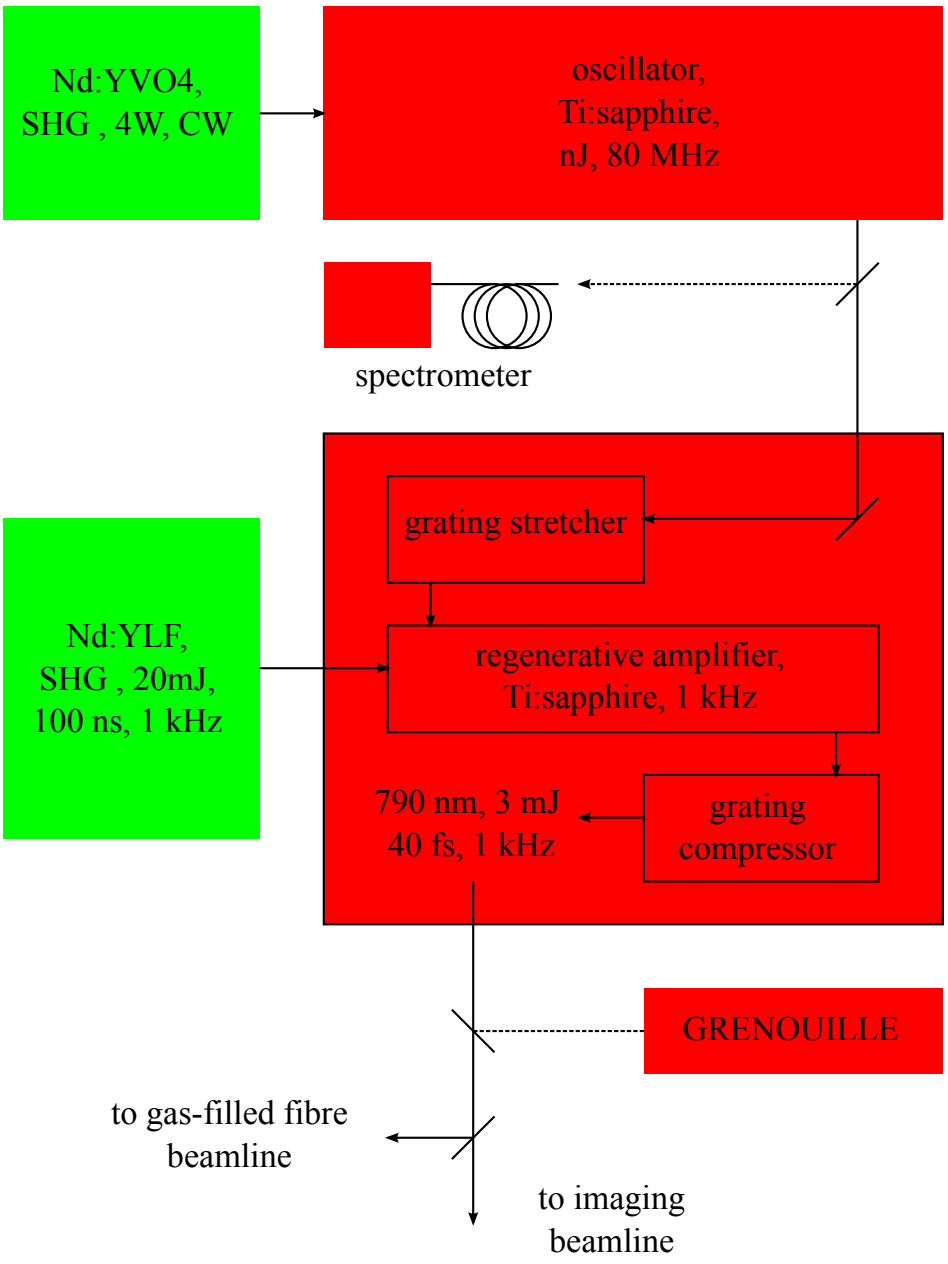

Figure 3.1: The laser system at the University of Southampton. The oscillator seeds a regenerative amplifier that is reliant on the CPA technique. Within the amplifier the repetition rate is reduced to 1 kHz and the 40 fs pulses are amplified to 3 mJ. After emerging from the amplifier the pulses are characterised by a GRENOUILLE device and distributed to the various beamlines.

laser oscillator (Spectra Physics, Tsunami) whose nJ pulses are delivered at a repetition rate of 80 MHz. These pulses enter the amplifier and are initially stretched by a grating-based stretcher. This lowers the peak intensity of the pulses considerably, thus relaxing the requirements on the damage threshold of the optical components within the amplification stage. The Ti:sapphire crystal is positioned at the center of the amplifier's cavity and is pumped from both ends by an external 20 W frequency doubled diode pumped solid state laser at 532 nm (Positive Light, Evolution 30). When operating the crystal is maintained at a sub-zero temperature by a Peltier to reduce the likelihood of thermally induced damage and stabilise the amplified mode. Once the gain medium has accumulated sufficient energy from the pump a single stretched pulse is allowed to enter the amplification stage via an electro-optic switch (in this case a Pockels cell). As the pulse undergoes round trips it is amplified to a high energy and a second intra-cavity Pockels cell and a thin-film polariser extract the amplified pulse directing it into a grating-based compressor. The dispersion added by the stretcher and accumulated during amplification is compensated for resulting in high energy ultrashort pulses leaving the amplifier. To aid the day to day compressor optimisation a commercial GRating-Eliminated No-nonsense Observation of Ultrafast Incident Laser Light E-fields (GRENOUILLE) device [67] (Swamp Optics) is sent a small portion of the amplifier output. This is a compact and greatly simplified frequency resolved optical gating (FROG) device [89], employing iterative phase retrieval to measure the full E-field of the amplifier output and also providing a near-field diagnostic to study the mode. The pulses are then distributed to the various beamlines by a combination of beamsplitters.

3.1.2 Fibre processing, installation and launch

When supplied the fused silica capillary-type fibres are 300 mm long with a 0.8 mm outer radius and 75 μm inner radius (Silica Fibre Fabrication Group, Optoelectronics Research Centre, University of Southampton). Incorporating these fibres into a HHG set-up proved to be a lengthy process but several optimised procedures are outlined here.

3.1.2.1 Cleaving and polishing

The first important step is to cleave the fibre to the required length. The optimised cleaving process is illustrated in Fig. 3.2 (a). The fibre is scored with a ceramic knife and a droplet of water is deposited to assist the propagation of the fracture through the cladding. Applying gentle longitudinal force along the length of the fibre and inducing a slight bend such that score 'closes' was found to produce the best cleaves when the end face was examined with an optical microscope.

Unfortunately, it was found that some unwanted material will always be left behind when cleaving a capillary-type fibre in this manner. To achieve an optical quality end

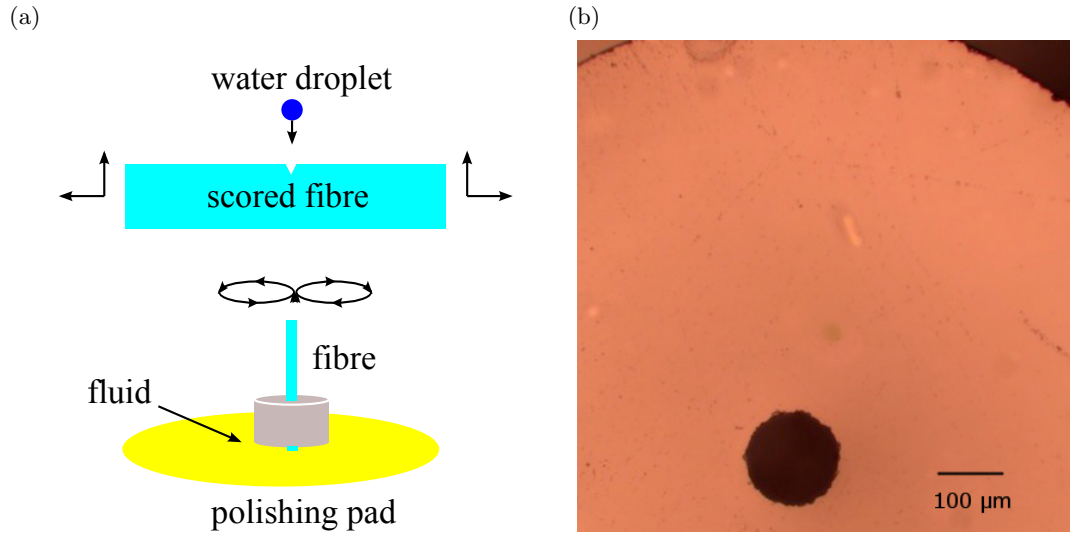

Figure 3.2: (a) The procedure used to cleave the fibre (top). The fibre is scored with a ceramic knife and a droplet of water deposited. The fibre is pulled gently from both ends and a slight bend applied to achieve a quality cleave. The fibre is then placed in a mount and polished (bottom) (b) The end face of the cleaved and polished fibre viewed under an optical microscope.

face lapping and polishing must be performed. This procedure is also illustrated in Fig. 3.2 (a) where the cleaved fibre is placed in a mount that does not restrict its vertical movement. Polishing fluid is then applied to the pad and the mounted fibre is translated in a smooth figure of eight motion. The polishing pad is replaced for one of a lower grade and the process is repeated (the smallest particle size used here is 300 nm). Once complete the fibre is placed in a solvent-filled sonic bath to remove any residue from the core and end faces.

The cleaved and polished fibre is shown in Fig. 3.2 (b). Note the macroscopic smoothness and lack of any cracks or scattering features that may limit the coupling efficiency. Work is ongoing to replace this procedure and make use of a laser cleaver available at the University of Southampton. This would speed up the process considerably and give high quality results.

3.1.2.2 Machining gas inlets

The next step in the fibre processing is to machine gas inlets through the cladding and into the core at several points along the length of the fibre. Femtosecond laser machining was selected for this task, as material will only be removed from the focal volume enabling a high degree of control. The apparatus is shown in Fig. 3.3 (a). The fibre is held in a V-groove on a 3-axis stage and high energy pulses from the laser system described in section 3.1.1 are focused into the cladding at the required inlet position.

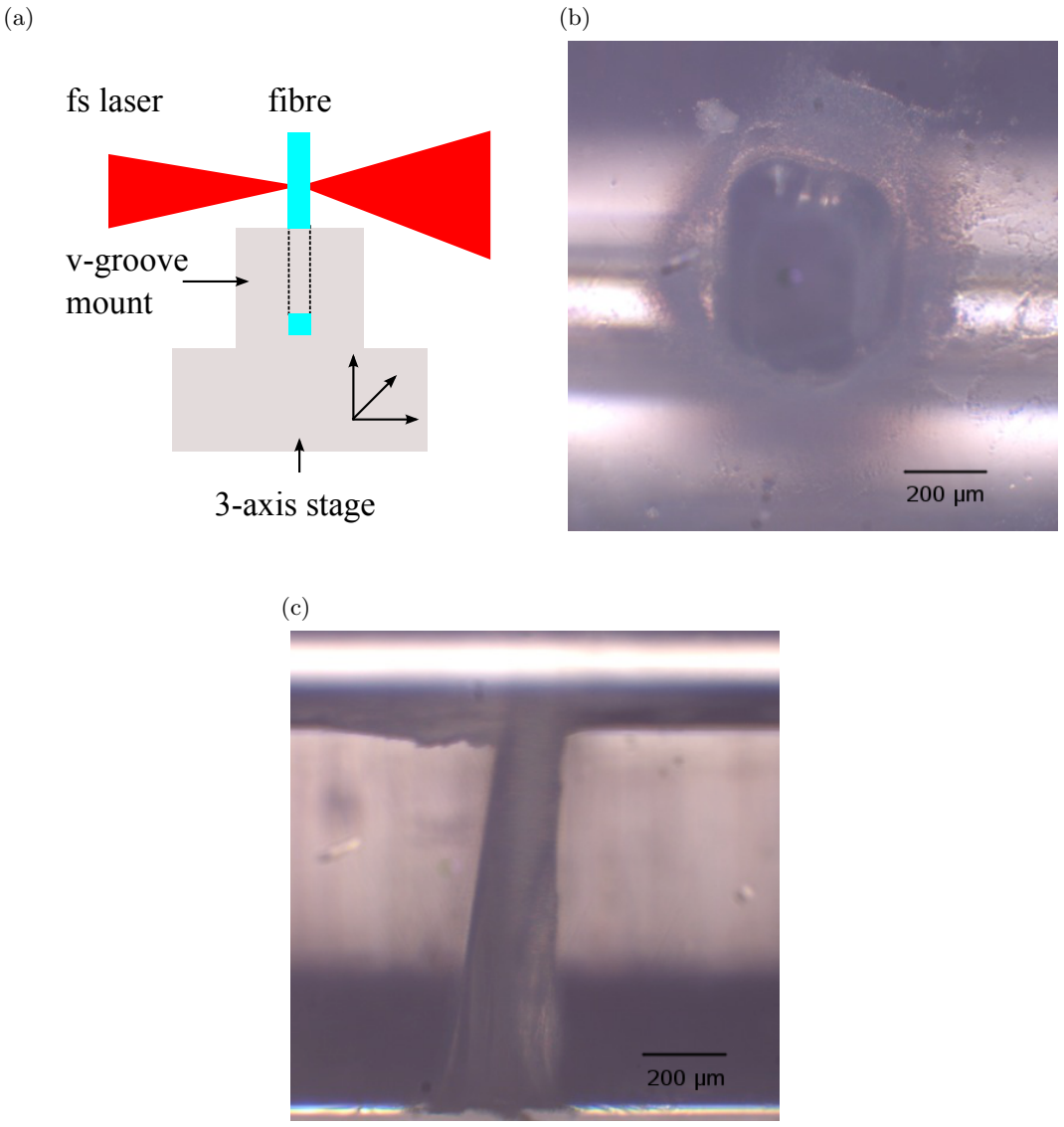

Figure 3.3: (a) The apparatus used to machine gas inlets in the cladding wall. The fibre is mounted in a V-groove on a 3-axis stage and multi-mJ laser pulses are brought to a focus at the required position. The stage is then translated to several positions in order to remove sufficient material. (b) The machined inlet viewed from above. Here, the fibre core is the bright stripe through the centre of the image. (c) The same inlet viewed from the side. This time the core is the bright stripe at the top of the image.

The time taken to remove 0.8 mm of material and penetrate the core was calibrated and the stage was scanned to enlarge the hole. The results are shown in Fig. 3.3 (b). Here, the inlet is imaged from above and the bright horizontal stripe through the centre is the hollow core. The same inlet is imaged from the side in Fig. 3.3 (c) and this time the bright stripe at the top is the core. These images show very little collateral damage highlighting the key advantage of femtosecond laser machining. Once the two inlets are complete the fibre is returned to the solvent-filled sonic bath and cleaned thoroughly prior to mounting.

3.1.2.3 Fibre mount

Once fibre processing is complete the bare fibre must be mounted in a manner that allows several hundred mbar of gas to be passed to the inlets while maintaining a high vacuum at the entrance and (especially) exit of the fibre to minimise nonlinear effects and XUV re-absorption. To achieve this the fibre is placed inside a glass T-piece and seals are created between the ends of the fibre and the two gas inlets. In Fig. 3.4 (a) the T-piece is fabricated such that these seals can be made by the injection of a UV curing adhesive. This approach is not suitable for all fibre designs as the inlet may become blocked if a seal is required to be in close proximity. If this is the case rubber X-rings can be used to make the seal. This technique is used for the fibre assembly in Fig. 3.4 (b) and has been found to perform well and enables T-pieces to be reused should the fibre become damaged.

The fibre assembly is incorporated into the beamline as shown in Fig. 3.4 (b). It is sealed between a pair of vacuum flanges that are attached to 2-axis stages and flexible bellows. The entire front end of the gas-filled fibre beamline is shown in Fig. 3.4 (c). Here, the third port of the fibre assembly is connected to a computer controlled pressure regulated supply and the pumping strategy is illustrated. This part of the system has proven to be very successful especially as extra support has now been added to stabilise the fibre.

3.1.2.4 Launch optimisation

Launching into a freshly prepared fibre assembly is a lengthy process however once it is in place daily alignment is far more straightforward. For the first step the lens and entire front end assembly are removed, a pair of irises installed along the intended path of the XUV (making sure this coincides with any subsequent components such as filter apertures, etc.) and the laser aligned through these. The pulse energy is reduced, the lens reinstalled and a knife edge measurement taken of the focal spot. The telescope before the grating compressor is adjusted slightly and focal spot measurements are repeated until the spot size coincides with the requirements for optimal coupling

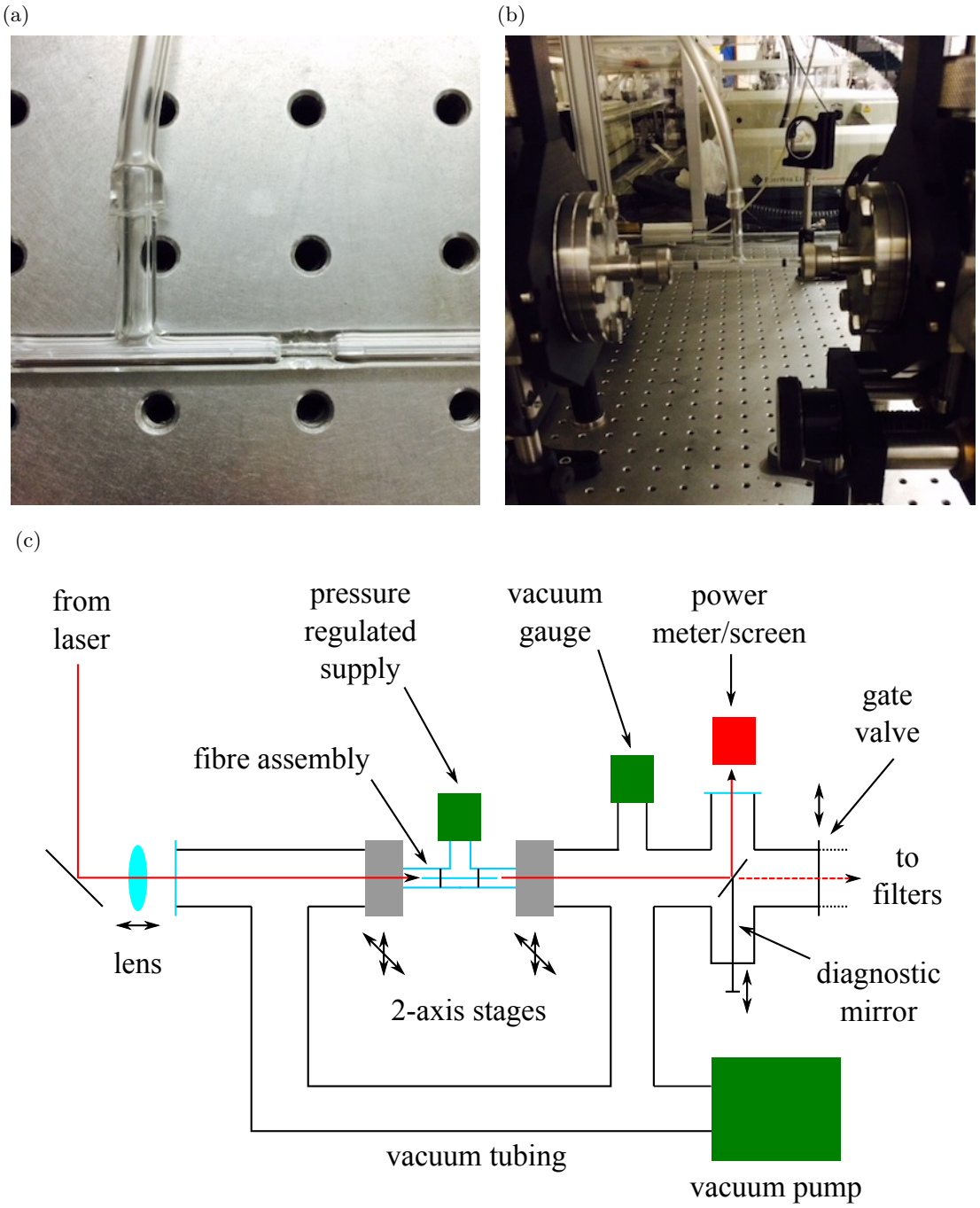

Figure 3.4: (a) The fibre secured within a glass T-piece using UV curing adhesive. (b) The T-piece assembly mounted within the gas-filled fibre beamline. This time the fibre has been secured in place by a pair of X-ring seals. (c) The front end of the gas-filled fibre beamline and all associated vacuum systems.

(a) (b)

Figure 3.5: Cartoon of the desired far-field mode pattern when aligning the fibre at low and then high pulse energies. (a) Initially the alignment of the fibre is performed with very low energy pulses. Under these conditions the 2-axis stages are translated and the fundamental mode optimised in the far-field. (b) Once the energy has been increased and gas injected the quality of the far-field ring pattern is used to further optimise the launch.

into the fundamental fibre mode (48 μm for a fibre with a 75 μm core radius). The position of this focus is then marked on the optical bench and the vacuum apparatus is reconstructed so that the fibre entrance coincides with this point.

The vacuum pump is switched on, the diagnostic mirror inserted and low-energy pulses allowed into the beamline. Using the 2-axis stages the position of the fibre is adjusted while examining the mode in the far-field. Adjustments should be made until it closely resembles Fig. 3.5 (a). The pulse energy is slowly increased while making constant adjustments to optimise the mode and minimise supercontinuum generation. The typical throughput achieved when following this procedure is $60 - 70\%$. Once a good launch has been made gas is injected into the fibre and laser power is transferred via the gases optical nonlinearities into the high order modes (the mechanisms responsible for this are the topic of the next chapter). The launch is then further optimised by enhancing the radial symmetry of this pattern to resemble Fig. 3.5 (b). This procedure has proved to be successful and lifetimes of fibres used in the beamline have exceeded a year.

3.1.3 Thin-film filters

Before XUV generated within the fibre is allowed to pass into the chamber containing the delicate diagnostic instruments the residual driving laser power must be removed. This is achieved by free-standing aluminium filters with thicknesses of several hundred

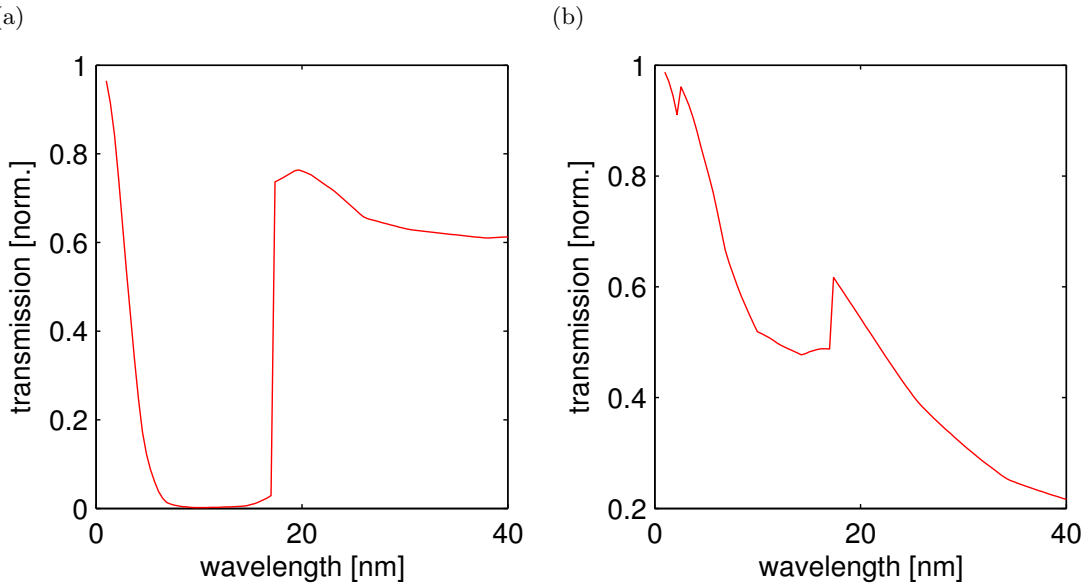

Figure 3.6: (a) The calculated transmission of a 200 nm film of aluminium for the wavelength range of interest [30]. (b) The calculated transmission of a 20 nm layer of aluminium oxide over the same range [30].

nm. These are excellent at rejecting the driving laser and low-order harmonics, and have proven to be resilient to long exposures and ageing. The transmission of 200 nm of aluminium at SXR and XUV wavelengths is shown in Fig. 3.6 (a). This is calculated from atomic scattering data in a similar fashion to the gas absorption calculation described in chapter 2. Unfortunately, the relatively high transmission between 20 and 40 nm is degraded by the formation of oxide layers on each side of the film. To illustrate how severe this can be the transmission of a 20 nm layer of aluminium oxide is shown in Fig. 3.6 (b). In section 3.1.5 the transmission of these filters will be measured experimentally and predictions about the oxide thickness extracted.

Fig. 3.7 (a) shows a selection of the filters used on the gas-filled fibre beamline. The two styles shown here are fabricated using different methods. The circular variety (Lebow Company) consist of two 100 nm thick aluminium films held onto a 5 mm aperture by van der Waals forces, and the square filters (Silson) are manufactured by depositing 200 nm of aluminium onto a silicon nitride membrane and etching part of this substrate away. Both perform well when a pair of filters is used, but if an individual filter is a requirement of the experiment the circular design is preferred. The filters are mounted and installed into the housing shown in Fig. 3.7 (b). Typically two filters are installed at two of the positions and a pair of beamblocks placed in the third. This is inserted into the precision machined vacuum T-piece shown in Fig. 3.7 (c) and the 3 positions can be selected via the mechanical vacuum feedthrough. This assembly includes a pair of baffles to aid the removal of the driving laser and a long 'siding' is incorporated into the design so the delicate filters can be moved out of the path of least resistance when evacuating the chambers.

(a)

(b)

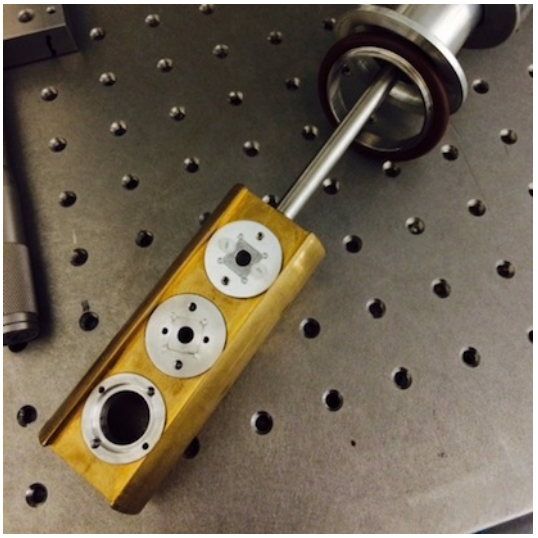

(c)

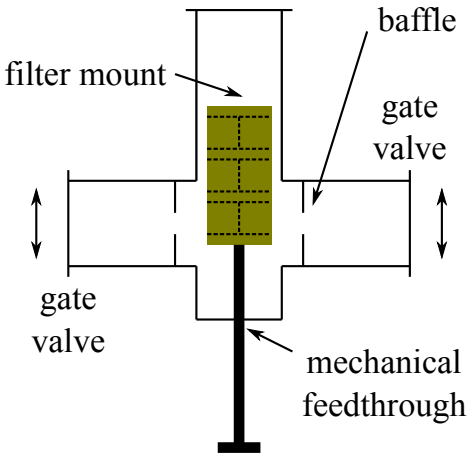

Figure 3.7: (a) A selection of free standing aluminium filters used on the gas-filled fibre beamline. The thickness here is 200 nm and the apertures are 5 mm. (b) The filter housing. Typically a pair of 200 nm thick aluminium filters are inserted into 2 of the available slots and beamblocks placed in the third. (c) The filter housing inside its precision machined vacuum fitting. The baffles are in place to further reduce laser scatter, and when evacuating the chamber the filters are pushed into the siding for added protection.

3.1.4 SXR/XUV diagnostics

The final element in the gas-filled fibre beamline is a suite of diagnostics for characterising the high harmonic beam. This and the required vacuum systems are shown in Fig. 3.8 (a). The x-ray CCD camera (Andor Technology) is used to record near-field images of the XUV beam. Photon numbers can be extracted from these as the quantum efficiency of the detector and exposure time are known. This camera is positioned on a motorised translation stage and once a series of images have been taken it slides out of the way allowing the XUV beam to propagate into the XUV spectrometer. This spectrometer (Shulz Scientific Instruments) is of a Rowland design and is illustrated in Fig. 3.8 (b). The XUV beam enters through the slit before striking a cylindrical gold grating (1 m radius of curvature) with an equidistant grove spacing of 300 lines/mm. The spectral components illuminating the slit are imaged onto the Rowland circle where a curved micro-channel plate (MCP) detector is positioned. The electron signal is converted to visible light by a phosphor screen and this is imaged from outside the vacuum chamber by a CCD camera (Princeton Instruments). As this detector assembly includes high voltage components an additional turbo pump is used to maintain a high vacuum within this instrument.

3.1.5 Harmonic beam characterisation and analysis

As the various component parts and alignment procedures have been presented the results of a simple source characterization experiment can be described. For this experiment $\sim$ 800 μJ pulses were launched using a 500 mm focal length plano-convex lens into a 70 mm long fibre. Gas inlets were positioned 20 mm from each end and it was secured inside the T-piece using the adhesive method. This was flooded with argon and the near-field profile of the XUV beam was recorded with the x-ray CCD camera. An exposure (100 ms) recorded with 200 mbar of gas in the fibre is shown in Fig. 3.9 (a). The non-uniformities are predominantly caused by a large damage spot and oil droplets contaminating the surface of the detector. From these images the number of XUV photons arriving at the detector each second can be found. It is then possible to back-propagate through the filters and estimate the XUV flux generated within the source. Before performing this back-propagation a simple experiment was carried out to measure the transmission of a well oxidised 200 nm thick aluminium filter. To do this one, two and then three filters were placed in the beam path, and from this data the transmission of a single filter was estimated to be 0.13. This implies an oxide layer of roughly 15 nm on each face of the filter. The photon flux measurements were then back-propagated through a pair of filters and the XUV flux generated within the source is plotted as a function of argon pressure in Fig. 3.9 (b). Error analysis was also performed, and taking into account uncertainties in the quantum efficiency data provided

(a)

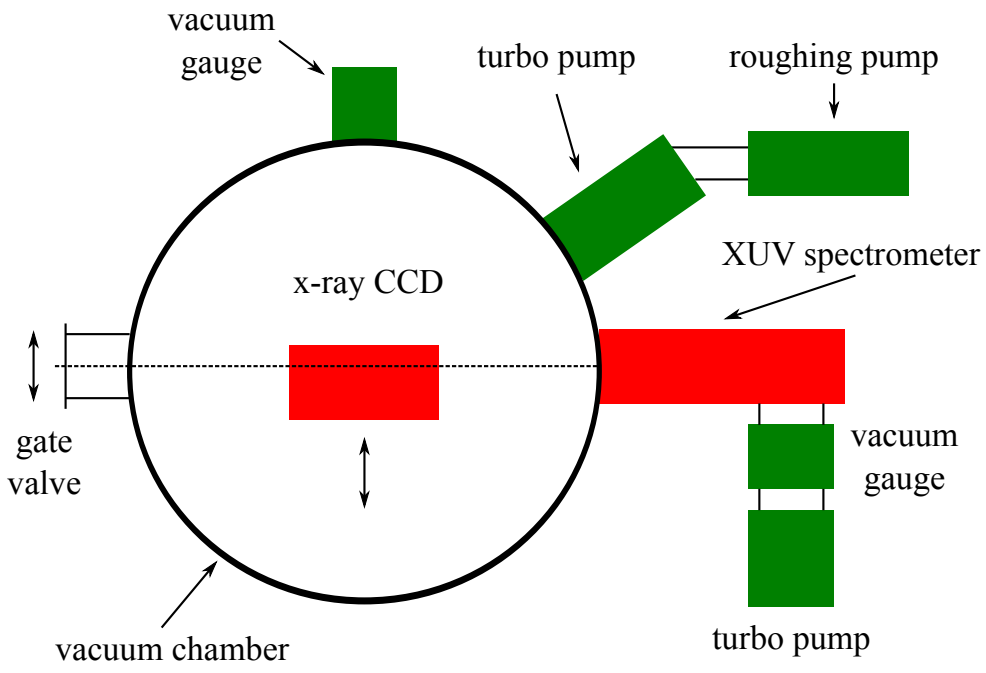

(b)

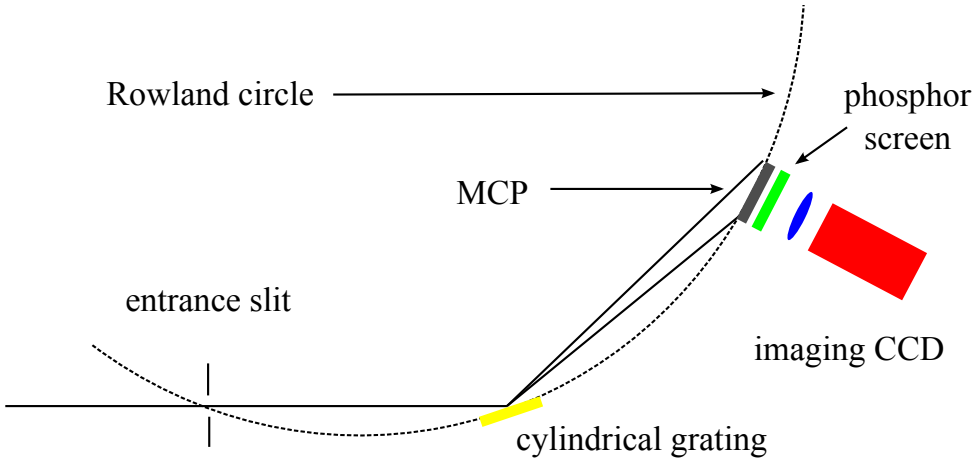

Figure 3.8: (a) The chamber housing the XUV diagnostics and their associated vacuum systems. The x-ray CCD is mounted on a motorised translation stage so near-field and absolute XUV flux measurements can be made before allowing the beam to propagate into the XUV spectrometer. (b) The layout of the spectrometer used to characterise the XUV output of the gas-filled fibre. This instrument is of the Rowland type and is configured to record spatially resolved spectra between 20 and 60 nm.

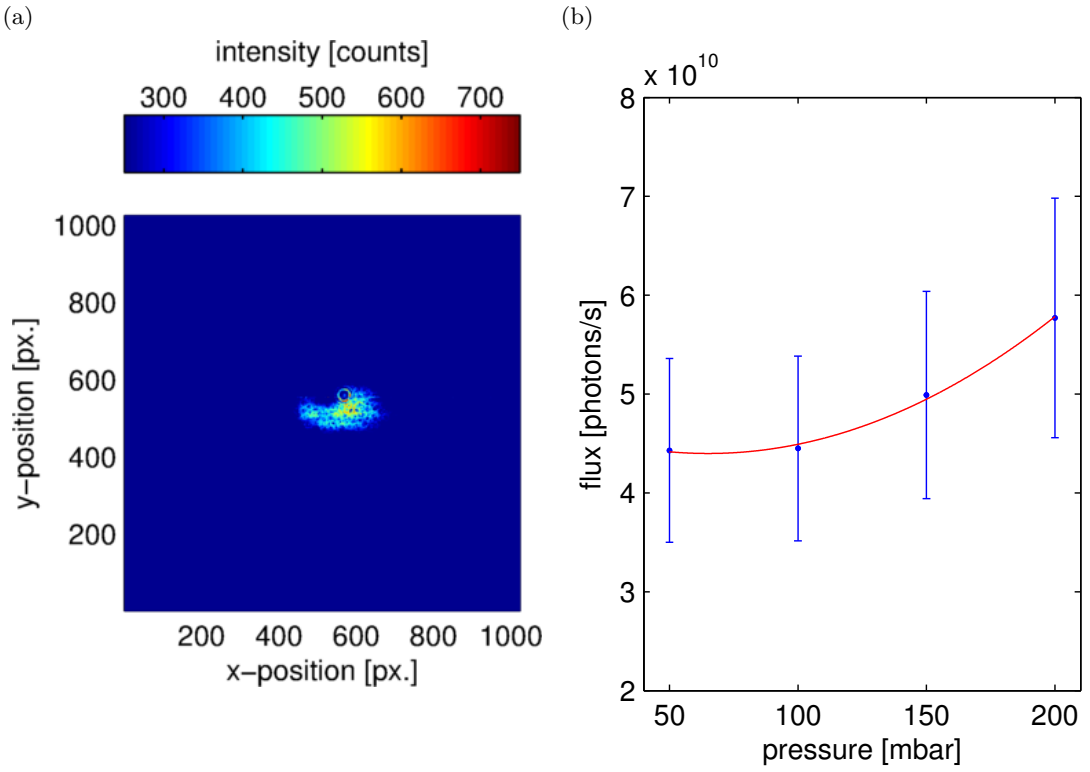

Figure 3.9: (a) An image of the XUV beam captured by the CCD camera. The feature towards the top of the beam is the result of damaged detector pixels, and the speckle pattern is caused by oil droplets on the detector surface. (b) The number of XUV photons arriving at the detector each second is calculated and plotted as a function of gas pressure. No dramatic enhancement in phase-matching is observed with this fibre.

with the detector and varying oxide thickness between filters a conservative error estimate of 20% was used. The low flux (when compared with published results in a similar geometry [79]) and the lack of any dramatic variation as the pressure is tuned imply that this is a poorly phase-matched source.

What is perhaps more interesting are the XUV spectra generated within this fibre. This particular dataset was taken by Tom Butcher under similar experimental conditions and results are shown for 50, 100 and 150 mbar in Fig. 3.10 (It should be noted that there is an uncertainty of several nm in the spectral calibration as only 1 calibration point was available and the central wavelength of the laser is dynamically changing). These measurements deviate considerably from high harmonic spectra recorded at lower gas pressures, and to understand the origin of the complex spatial and spectral structure the model developed in chapter 2 was used. The experimental parameters were replicated in the UPPE-TDSE model and when completed the XUV field was propagated through a pair of filters and into the far-field. The numerical results (Fig. 3.11) capture many of the features observed in the experiment. The off-axis structure is found to be imprinted directly onto the harmonic beam by the mode functions that confine the driving laser.

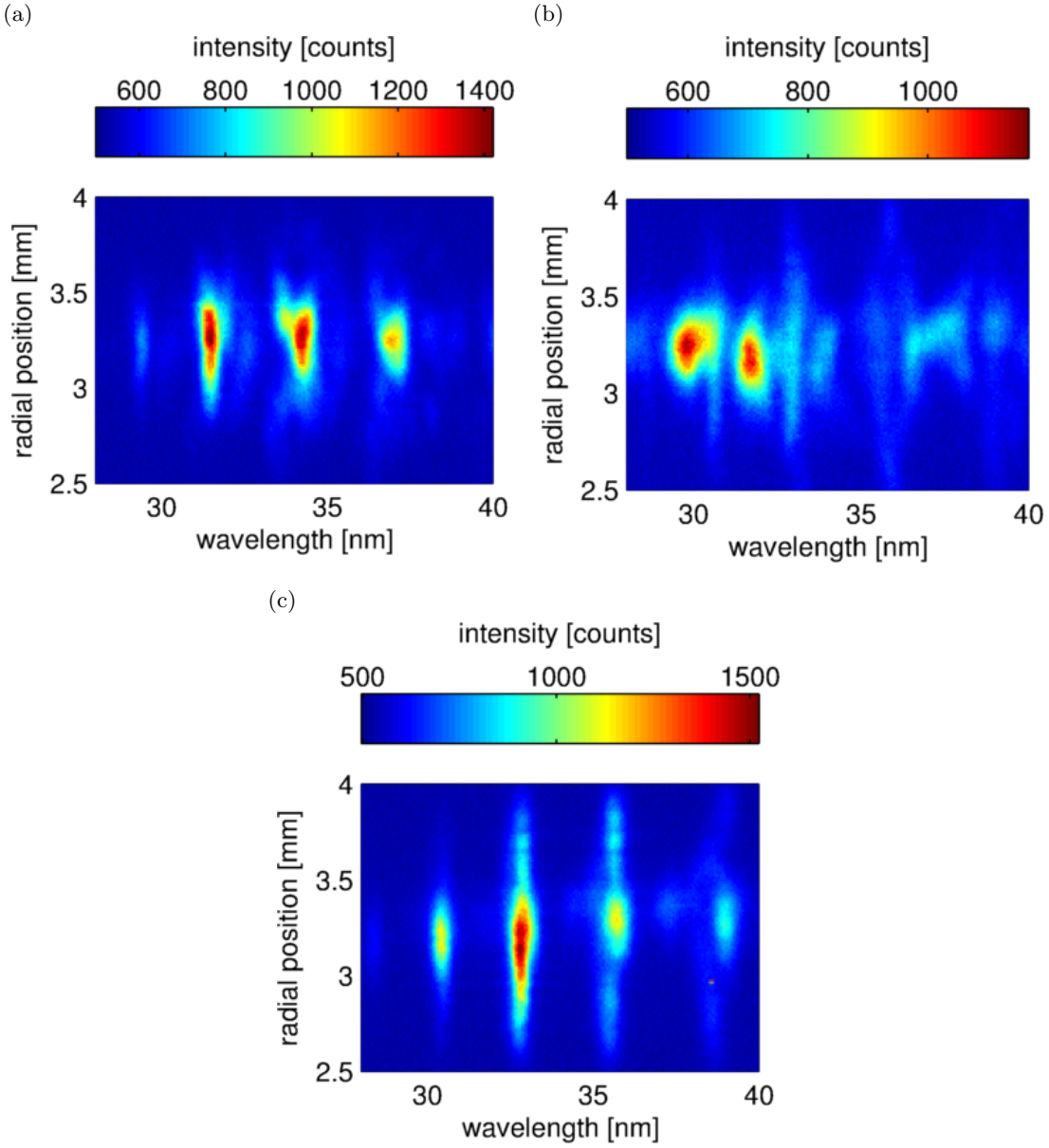

Figure 3.10: XUV spectra recorded when 50 (a), 100 (b) and 150 mbar (c) of argon is injected into the fibre. These spectra are far more complex than those observed at lower gas pressures, and to understand the origins of this reshaping the sophisticated model developed in chapter 2 was used. Note that due to only a single calibration point being availible and a dynamic central wavlength there is an uncertainty of several nm in the wavelength axis.

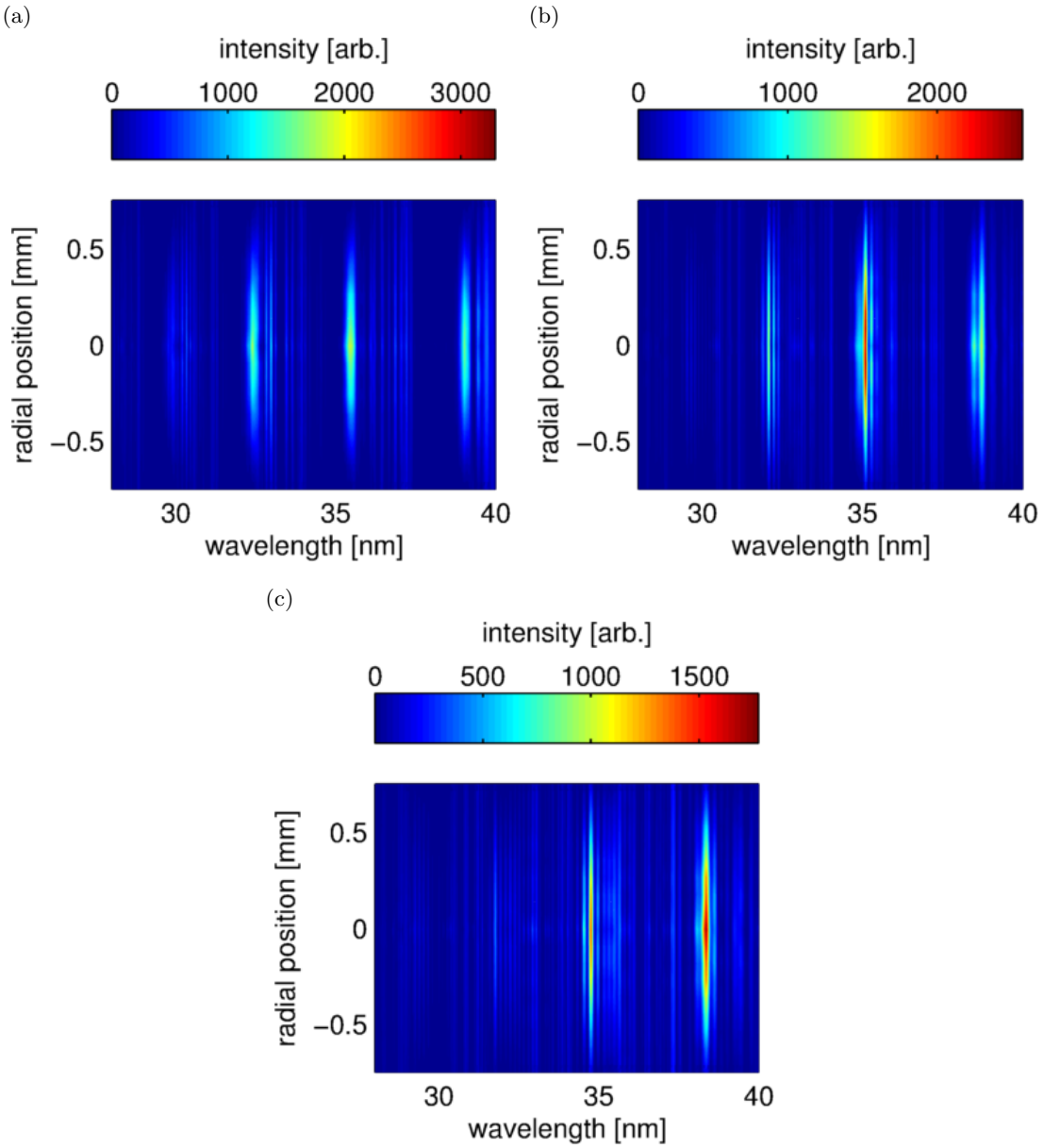

Figure 3.11: The experimental conditions used in Fig. 3.10 were replicated in the full UPPE-TDSE model and the results propagated into the far-field. Much of the complex radial and spectral structure observed in the experiment is replicated here. This can be correlated to the mode functions supported by the fibre and the highly nonlinear propagation of the driving laser. These represent some of the most sophisticated simulations of HHG performed to date.

It can also be confirmed that the complex spectral structure is the result of the driving laser undergoing increasingly nonlinear propagation as the gas pressure is increased (the mechanisms responsible for this will be developed in the next chapter). This leads to HHG being driven by multiple time delayed pulses, which in turn produces strong modulations in the XUV spectrum. This is an interesting effect and the contrast of the driving pulse can be enhanced by minimising these modulations in the XUV spectrum. This is analogous to a common technique used to diagnose and correct multi-pulsing in mode-locked lasers.

3.2 Extended gas cells

This section describes a 4 week experiment performed at the Artemis facility. The proposal stated that optimised conditions would be found for extending the high harmonic spectrum to shorter wavelengths. The XUV beam would then be monochromated at 13.5 nm and brought to a focus where CXDI would be carried out. The source development was very successful and several groups have begun to use the apparatus constructed for CXDI of test objects and biological samples. This work was performed with Bill Brocklesby, Richard Chapman and Peter Baksh.

3.2.1 Modifications to the AMO beamline at Artemis

The Artemis facility is based around a laser oscillator-multipass amplifier system (KM Labs) capable of delivering 12 mJ NIR (800 nm) pulses with 30 fs durations at a repetition rate of 1 kHz. Additionally, this can be used to pump an OPA (Light Conversion) to provide novel wavelengths or sent into a nonlinear pulse compressor to access few-cycle pulses. Implementing a fibre-based HHG source into the allocated beamline was not possible in the short time period so an extended gas cell was selected instead. For these experiments focusing, pulse energy, gas species and driving wavelength were free parameters in the optimisation procedure.

Fig. 3.12 shows the modifications made to the existing beamline. The light blue dielectric mirrors deliver high energy NIR pulses to the gaseous target and the grey unprotected metallic mirrors are used to deliver the output of the OPA. Note that the focusing optics have also been exchanged (1 m focal length dielectric and 0.5 m focal length metallic) to maintain a more consistent intensity. The metallic mirrors are also used to deliver NIR pulses to a 100 μm thick BBO crystal within the vacuum chamber allowing HHG to be performed with visible light. The aperture of this crystal is relatively small so a reflective telescope is included in the beam path prior to the chamber.

The 5 mm long gas cell is attached to a pulsed valve (attotech) and suspended from a 3-axis vacuum feed-through. This arrangement was later found to be a source of

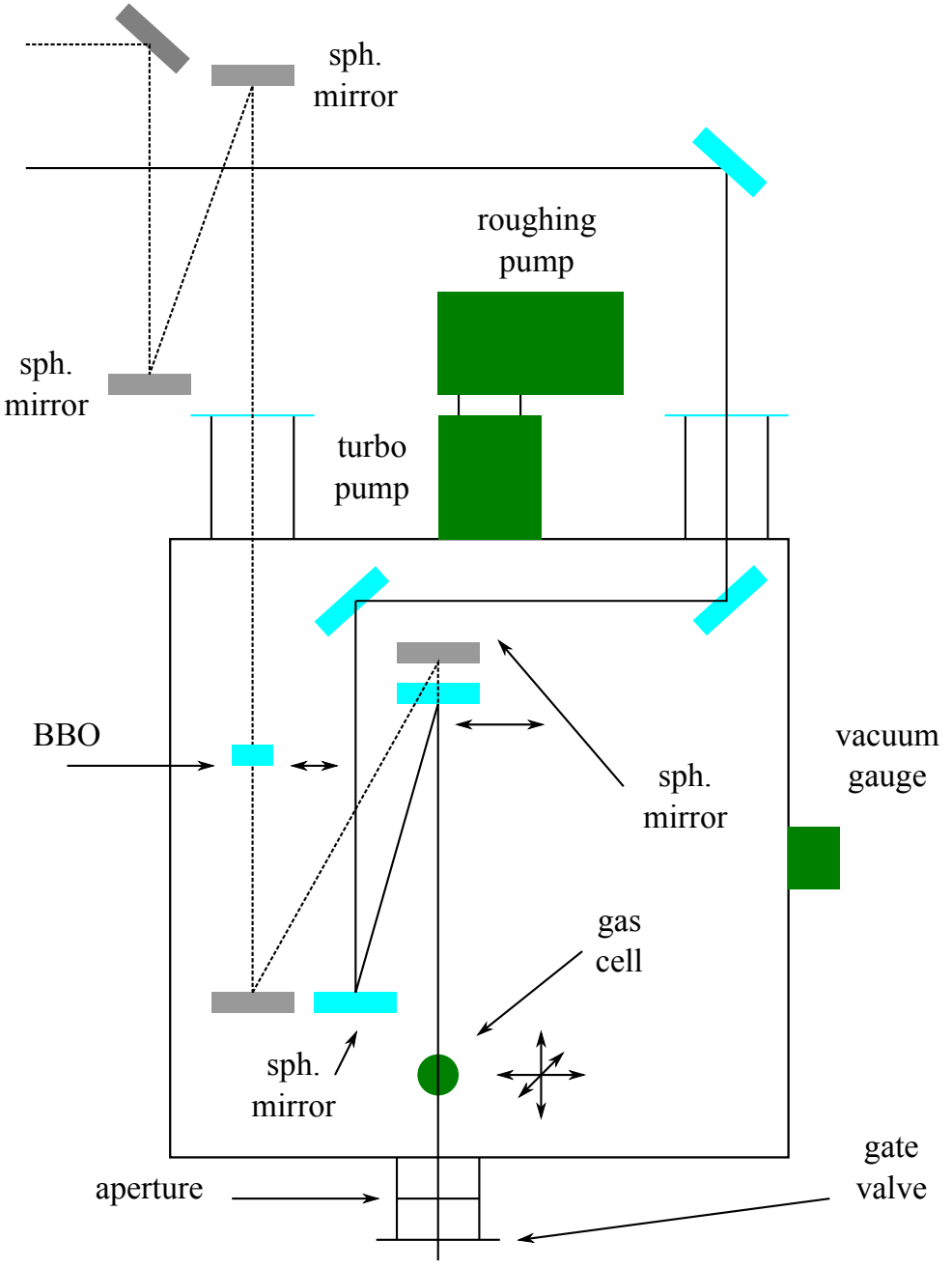

Figure 3.12: The new layout of the XUV generation chamber at Artemis. The light blue dielectric mirrors deliver energetic NIR pulses to the gas cell and the grey metallic mirrors deliver the output of the OPA. The metallic mirrors are also used when driving a BBO crystal with NIR pulses and generating high harmonics with visible light.

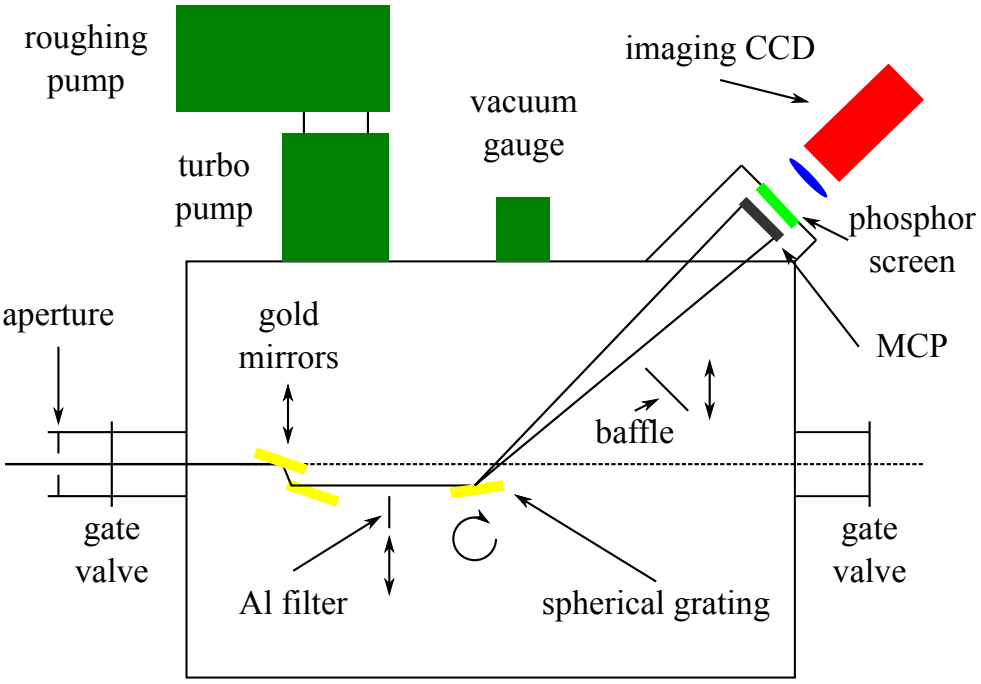

Figure 3.13: The XUV spectrometer positioned directly after the generation chamber at Artemis. The beam is diverted onto the grating by translating a pair of gold grazing-incidence mirrors into its path. After striking the aberration corrected grating the spectrum is focused across the flat detector assembly. The instrument also includes a baffle to block the zero-order beam and an aluminium filter can be positioned in the beam to assist calibration.

instability in the XUV beam, and the gas cell has since been remounted on a stable 3-axis motorised stage attached firmly to the optical bench.

3.2.1.1 Flat-field XUV spectrometer

For this experiment the Artemis flat-field spectrometer was positioned directly after the large vacuum chamber shown in Fig. 3.12. This instrument is pictured in Fig. 3.13. The XUV beam passes through a differential pumping aperture and is deflected onto the grating by a pair of gold grazing-incidence mirrors that can be translated in and out of the beam. The advanced aberration corrected grating (Hitachi) enables the foci to be manipulated into a 'flat-field'. The vacuum flange holding the detector assembly was re-designed so that it overlapped with this region for the entire wavelength range of interest (35 - 10 nm). The instrument also included a baffle to prevent the bright zero-order beam from saturating the detector and an aluminium filter could be translated into the XUV beam to provide a good calibration point at 17 nm. In future experiments it would be advantageous to move the spectrometer further away from the gas cell. This

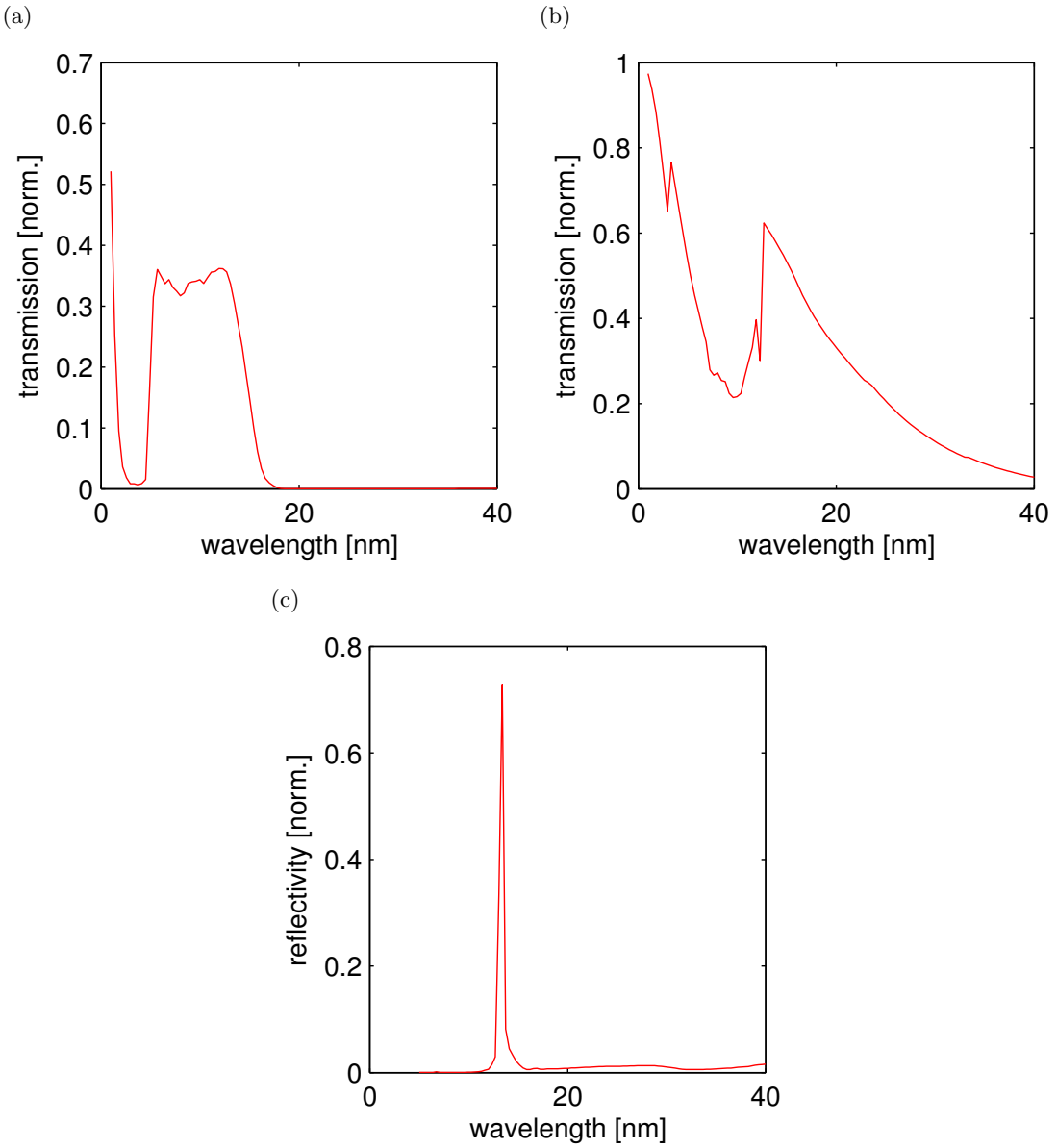

Figure 3.14: (a) The transmission of a 200 nm film of molybdenum for the wavelengths of interest [30]. (b) The transmission of the 50 nm thick silicon nitride substrate [30]. (c) The simulated reflectivity of a mirror consisting of 100 thin layers of silicon and molybdenum for a 5° incidence [30]. The narrow peak is centred at 13.7 nm.

will reduce the likelihood of optical damage to the mirrors and grating and enhance the vacuum, enabling higher gas densities or lighter species to be used.

3.2.1.2 Isolating the 59th harmonic

The aluminium filters described in the previous section do not transmit between 6-17 nm so this well tested technology had to be replaced with something else. Several metallic

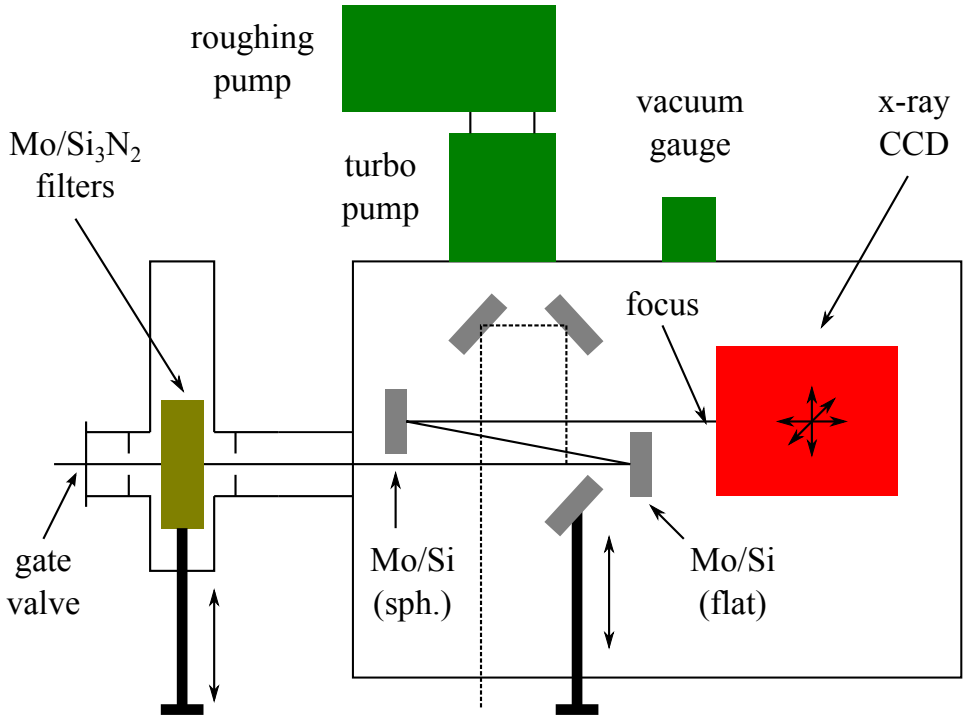

Figure 3.15: The chamber constructed to remove the residual driving laser, pick out the 59th harmonic and bring it to a tight focus ready for CXDI. The three mirrors that are not labelled are conventional metallic mirrors and are used to confirm that the filters are attenuating the driving laser sufficiently.

films including zirconium have been used previously for this task but molybdenum (Mo) is explored here because of its widespread use as an optical coating technology. Fig. 3.14 (a) shows the transmission of a 200 nm thick layer of molybdenum. The transmission band overlaps nicely with the desired harmonic positioned at 13.5 nm. In addition to the novel coating the filters were also prepared on 50 nm thick silicon nitride (Si_3N_4) substrates. The transmission of these is shown in Fig. 3.14 (b), and thankfully the harmonic of interest lies just to the right of the sharp absorption edge. The addition of this substrate simplifies the fabrication process and greatly enhances the robustness of the filters to pressure differentials. Due to the broad bandwidth of the filters they cannot be used to extract an individual harmonic, and this is instead achieved via molybdenum/silicon (Mo/Si) multilayer mirrors. The simulated reflectivity [49] of a stack of 100 thin (10 nm) layers of molybdenum and silicon is shown in Fig. 3.14 (c) for a 5° incidence. The reflectivity peak is sufficiently narrow to isolate an individual harmonic at 13.5 nm.

The filters were fabricated (Silson), mounted and inserted into a housing and vacuum T-piece identical to the one described in the previous section. Next, the multilayer mirrors (Fraunhofer) were positioned as shown in Fig. 3.15. Here, a flat multilayer reflects the harmonic back onto a spherical multilayer with a focal length of ~ 300 mm. The focal

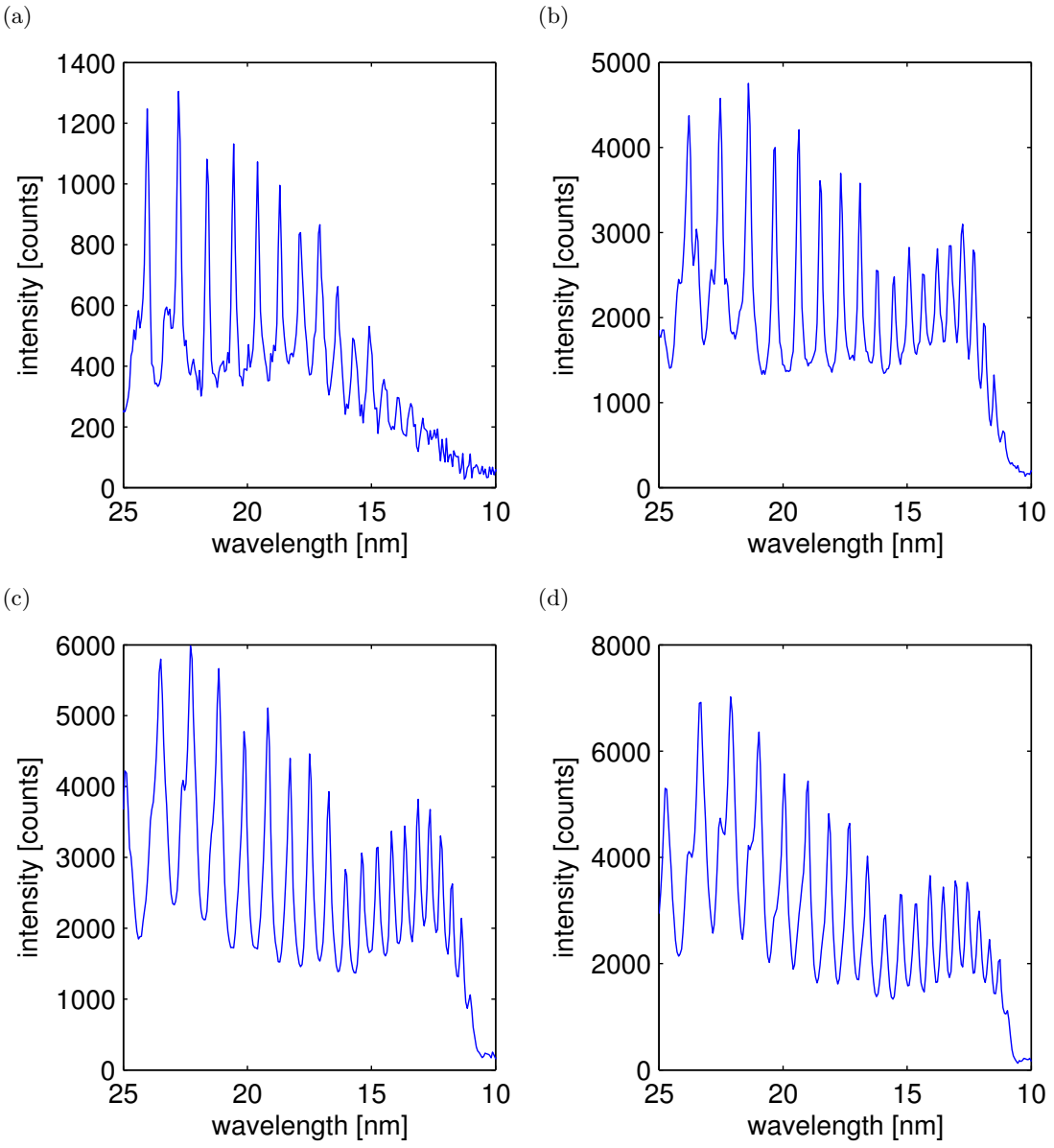

Figure 3.16: The high harmonic spectrum recorded by the flat-field spectrometer when the neon-filled gas cell is driven by 1 (a), 2 (b), 3 (c) and 4 mJ (d) NIR pulses.

volume of the 13.5 nm beam can then examined by the x-ray CCD (Andor Technology) positioned on a 3-axis motorised stage. The final three mirrors inside the chamber are conventional metallic mirrors and are used to diagnose the extinction ratio of the driving laser striking the filters. Monitoring this is important because any filter damage could lead to the driving laser being focused onto the CCD chip.

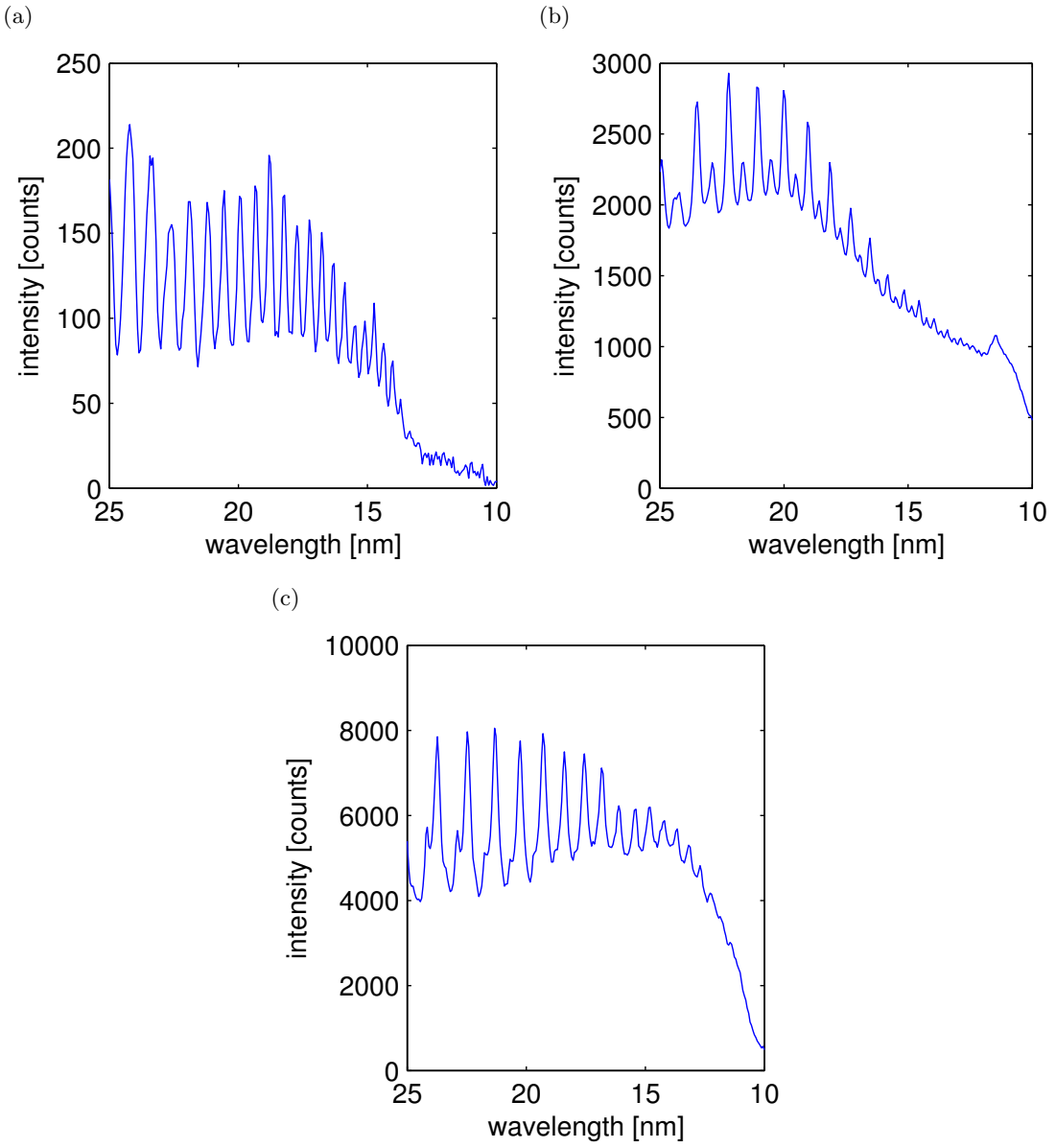

Figure 3.17: (a) The spectrum recorded by the flat-field spectrometer when driving HHG in argon with 1400 nm pulses. (b) This time the interaction is driven with frequency double NIR pulses. The residual NIR leads to both odd and even harmonics being generated. (c) Bright harmonics generated when 5 mJ NIR pulses are sent into helium.

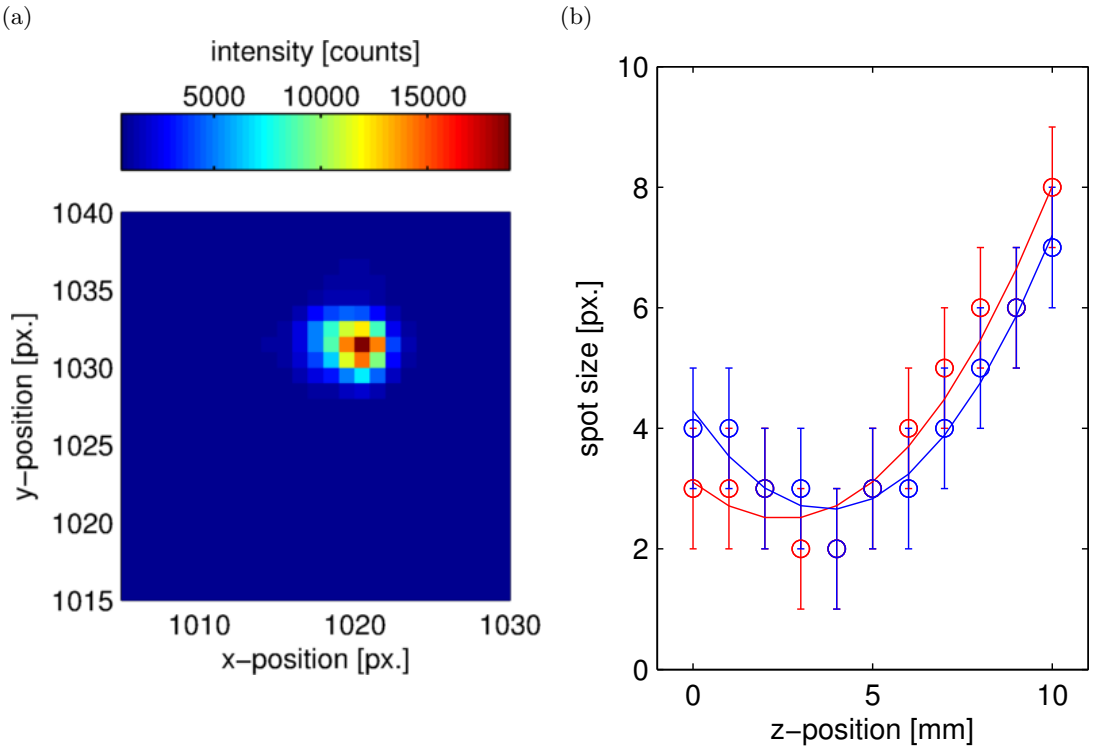

Figure 3.18: (a) An image of the 13.5 nm XUV beam taken away from the focus using the x-ray CCD camera. (b) The spot size measured in the x and y-direction though the focus. The separation between the foci is caused by the spherical focusing mirror being positioned off-axis.

3.2.2 XUV wavelength and flux optimisation

Now the development work has been presented the source optimisation and characterisation experiments can be discussed. The first of these experiments was fairly straightforward, and involved increasing the NIR pulse energy and monitoring the XUV spectrum using the flat-field spectrometer. The gas selected for this experiment was neon, due to its high ionization energy and the ease at which it is handled. Fig. 3.16 (a) shows the high harmonic spectrum produced with 1 mJ driving pulses. This spectrum shows that the pulse energy is insufficient as the 13.5 nm harmonic is positioned in the cut-off region of the spectrum. The pulse energy was increased to 2 mJ and the cut-off shifted to shorter wavelengths as expected. This is shown in Fig. 3.16 (b). The pulse energy was increased further to 3 (Fig. 3.16 (c)) and 4 mJ (Fig. 3.16 (d)) but the flux of the harmonic of interest quickly saturated. The gas cell was then translated along the focal volume searching for the optimal focussing conditions for phase-matching. These were found to be in the proximity of the starting position so there was no need to repeat the measurements. Increasing the time that the gas cell was supplied with neon was also tried, but this quickly led to the pressure within the chamber exceeding the safe limit.

For the next set of experiments the gas cell was driven with 1 mJ MIR (1400 nm) and then 400 μJ VIS (400 nm) pulses. These pulse energies were lower than expected and thus the gas had to be exchanged for argon in order to observe HHG. The idea here was to test the simple scaling laws introduced in chapter 1 and see if either could enable access to bright 13.5 nm radiation. As the driving wavelength is increased it is expected that the cut-off will shift to shorter wavelengths. This is verified in Fig. 3.17 (a) but with this decrease in wavelength comes a considerable reduction in flux. Going the other way and driving the interaction with 400 nm pulses in the presence of the residual NIR field (as in fig. 3.17 (b)) has the opposite effect. Generation becomes more efficient but the 13.5 nm harmonic is engulfed by the cut-off. For the final measurement the gas was exchanged for helium to take advantage of its very high ionization potential and 5 mJ NIR pulses were launched into the gas cell. The flux at 13.5 nm (Fig. 3.17 (c)) was slightly higher than that recorded in neon but removing the helium from the chamber was too much of an engineering challenge for the short experimental run. Because of this and the desire to work at lower pulse energies to protect the filters 2 mJ NIR pulses and neon were the chosen generation configuration.

Once the generation parameters had been optimised the next step was to test the filters, focusing geometry and measure the flux to see if these are appropriate for CXDI. For the first part of this the metallic mirror directly before the flat Mo/Si multilayer was translated into the beam and a photo-detector placed in the deflected beam path. An individual Mo/Si_3N_4 filter was used to block the residual driving laser and a transmission at 800 nm of 7×10^{-5} was measured. Before removing the mirror blocking the XUV beam path, the longevity of the filters was confirmed by performing several long exposures. Once satisfied the mirror was removed and the CCD camera was started. It was found that when positioned close to the focus at least 3 filters were required to achieve an acceptably low background. An image of the 13.5 nm beam recorded away from the focus is shown in Fig. 3.18 (a). From this and the quantum efficiency data provided with the camera the number of photons delivered to the focus was calculated. This value was found to be 5×10^5 photons/s which is sufficient for performing CXDI provided long exposure times are acceptable. Back-propagating this through the mirrors and filters gives a flux of $\sim 1 \times 10^8$ photons/s. This is considerably lower than the flux measured from the gas-filled fibre, but for CXDI the shorter wavelength may make up this because of lower material absorption. To complete the characterisation the CCD camera was translated along the optical axis through the focus. The spot size in the x and y-direction is shown in Fig. 3.18 (b). This gives a conservative estimate of the focal spot size to be 20 μm. The source of the slight separation between the two foci is due to the use of an off-axis spherical focusing mirror, and the large uncertainty is due to the pixel size of the detector approaching the spot size. Such a focus has not proved to be a major hindrance when performing CXDI.

3.3 Conclusions

The topic of the first part of this chapter was the gas-filled fibre beamline at the University of Southampton. The procedures developed to process, mount and launch into a fibre were described in detail before discussing the results of a source characterisation experiment. The XUV spectrometer measurements were found to be particularly interesting and these were compared to results predicted by the UPPE-TDSE model. This sophisticated model enabled the spatial reshaping of the XUV beam to be linked to the mode functions supported by the fibre, and the spectral reshaping was attributed to the highly nonlinear propagation of the driving pulses.

The second geometry discussed was a source of 13.5 nm XUV constructed at the Artemis facility. The first part of this experiment involved finding the optimum conditions for efficient generation. Many parameters were explored including MIR and VIS driving wavelengths but the most efficient combination was found when focusing 2 mJ NIR pulses into a neon gas cell. Next, the thin film technology was developed to remove the residual driving laser, isolate and focus an individual harmonic at 13.5 nm. Finally the focal spot was characterised and found to be well suited to CXDI. Visiting scientists have begun to use this apparatus to image test objects and biological samples.

The next step in this work is to use fibre based sources on a day-to-day basis for CXDI. To achieve this the long term stability needs to be improved, possibly via an entirely new mounting, launching and alignment strategy.

Chapter 4

Self-compression in short gas-filled fibres

This chapter is largely based on [7] and has been extended to include a selection of experimental measurements at NIR wavelengths.

The CPA technique is evolving rapidly and is expected to deliver intensities above 10^{23} Wcm^{-2} this decade [35]. At more modest intensities where HHG is performed, laser system development is focussed on increased repetition rates and providing access to novel wavelengths from the mid-infrared through to the visible and ultraviolet (UV). To achieve this an additional stage of temporal compression is desirable after CPA (or after the subsequent wavelength conversion module) as it provides an elegant pathway to increased peak powers. Also, several high-field techniques are enhanced when driven with few-cycle pulses, as will be the discussed in the next chapter.

One compression technique that has gained particular popularity involves passing pulses through a long (often a metre or more) capillary-type fibre filled with a high pressure (typically several bar) atomic gas [64]. Here, the Kerr nonlinearity of the neutral gas leads to spectral broadening. After the fibre a combination of chirped mirrors and thin glass wedges can be used to carefully tune the spectral phase, enabling the compression of multi-mJ many-cycle pulses into the few-cycle regime [14]. An alternative to this is the 'self-compression' phenomena observed when laser pulses undergo filamentation [55]. Typically, these experiments involve loosely focusing high energy laser pulses in air or an extended gas cell such that the peak power exceeds the critical power for self-focusing. Under these conditions the linear and nonlinear response of the ionizing gas can reshape the pulse dramatically in both space and time, again enabling the compression of conventional multi-mJ pulses to few-cycle durations [84]. Despite being useful techniques, both schemes come with their own disadvantages and limitations. Hollow fibre compressors require specialised optics, complex optomechanics and considerable space. As pulse energies are increased the gas will begin to ionize requiring compressor designs to be

modified. It has been suggested that it may be advantageous to replace the hollow fibre altogether and use a planar waveguide instead [66, 1]. When compressing pulses via filamentation the temporal structure often becomes very complex, limiting the efficiency of the technique. Additionally, at high pulse energies the onset of multi-filamentation [11] leads to expansive and intricate spatial structure. This reduces both the usable energy and stability of the few-cycle pulses, and shifts numerical study beyond the reach of most groups. To overcome some of these issues modified self-compression schemes are being explored where the interaction region is confined to a short (several cm) gas-filled fibre. One of the first experiments of this type was performed by N. Wagner *et al.* where 2 mJ pulses were compressed from 30 fs to 13 fs after propagating through a 25 mm fibre filled with 5 mbar of argon [90]. The low gas pressures and short propagation lengths allow HHG to be performed efficiently within the compressor device itself [9, 18]. This property will become only more valuable as the high field community continues its shift towards the MIR [88, 83, 75, 8] and VIS/UV [36, 12] where ultrabroadband components are not as well developed.

The key to extending this new technique to deliver few-cycle pulses and guarantee compatibility with novel laser sources is to gain a deep understanding of the physical mechanisms involved. To date, several groups have performed theoretical studies that predict self-compression of energetic laser pulses as they propagate through fibres filled with low pressure atomic gases. Courtois *et al.* [28] build on the coupled mode equation developed by Tempea and Brabec [87] and predict the self-compression of 7 mJ 129 fs pulses to 51 fs after just 1 mm of propagation through a fibre filled with 10 mbar of helium. In the work by Wagner *et al.* [90] numerical solutions to Christov's [22] three-dimensional scalar wave equation are included in the study. The authors go on to compare these with experimental data achieving a varying degree of success.

In this chapter the state-of-the-art nonlinear pulse propagation models developed in chapter 2 are successfully used to isolate a mechanism that can provide access to few-cycle pulses in this new compression geometry. These results are then shown to be consistent with experimental spectra and SHG FROG measurements recorded in the far-field. Further simulations show that the mechanism is also applicable at VIS and MIR wavelengths, and work is ongoing to incorporate microstructured fibres into the system with the aim of compressing 100 μJ few-100 fs pulses delivered by high-repetition rate fibre CPA systems.

4.1 Preliminary simulations and analysis

Oscillator-amplifier systems using a bulk Ti:sapphire gain medium (like the two described in chapter 3) are a relatively mature technology and are widely available commercially. Short pulse variants have pulse durations of 25 - 45 fs, central wavelengths

close to 800 nm and depending on repetition rate pulse energies between 100 μJ and 10 mJ. In this section the modified MM-GNLSE will be used to study the spatio-temporal evolution of such pulses through short capillary-type fibres filled with low pressure atomic gases.

4.1.1 Proposed spatio-temporal reshaping mechanism

For an initial simulation an 800 μJ pulse with a Gaussian temporal envelope, 40 fs FWHM and 800 nm central wavelength is launched into a fibre with a 75 μm core radius such that optimal coupling is achieved into the fundamental mode. The fibre is filled uniformly with 100 mbar of argon and the pulse is allowed to propagate for 32 mm. The initial conditions and results of the simulation are shown in Fig. 4.1. At the launch ((a) and (c)) 98.1 % of the power is contained in the fundamental mode. It should be noted that the modes included in this figure are restricted to the 5 lowest order $EH_{1,m}$ modes for clarity and 20 modes were used in the simulation. As the pulse propagates ((b) and (d)) it is found that higher order modes are rapidly excited via the plasma defocussing term in Eq. (2.31). To understand the physics and how it leads to interesting temporal behaviour it is helpful to examine the simple optical system in Fig. 4.2 (a). Here a negative lens (the free electron distribution, refractive index < 1) is placed between a pair of long parallel reflectors (the fibres core wall). The collimated beam (fundamental mode) is defocused by the lens and a tight focus is formed after striking the reflectors. Now, in the time dependent case the strong nonlinear field dependence of the photoionization process causes the 'negative lens' to form close to the peak of the pulse (Fig. 4.2 (b)). The deflected/confined light (higher order modes) will therefore acquire a shortened temporal envelope, which is clear to see in Fig. 4.1 (b) m = 3. Analysis based on modal envelopes is essential for understanding the underlying mechanisms but can be misleading as the relative phases and extreme spatial confinement of high order modes may be forgotten. Instead, it is more appropriate to study full spatio-temporal/spectral fields (Fig. 4.3). The dominant feature in Fig. 4.3 (a) arises when several of the compressed high order modes overlap such that they are in phase with each other. In this particular example at $t \simeq 20$ fs the on-axis temporal FWHM (see the inset) is reduced to 4 fs, giving an order of magnitude of temporal compression after just 32 mm of propagation. This compressed feature contains $\sim 20\%$ of the launched energy and it displays a good contrast with respect to the features at 0 and 50 fs. As HHG doesn't have any strict contrast requirements a contrast of 2 or more will be considered good in this work.

The mechanism described here is very different to that developed to describe self-compression within filaments. Neutral gas nonlinearities are found not to contribute at all, however similar compression ratios and efficiencies are achieved at low gas pressures where HHG is routinely performed.

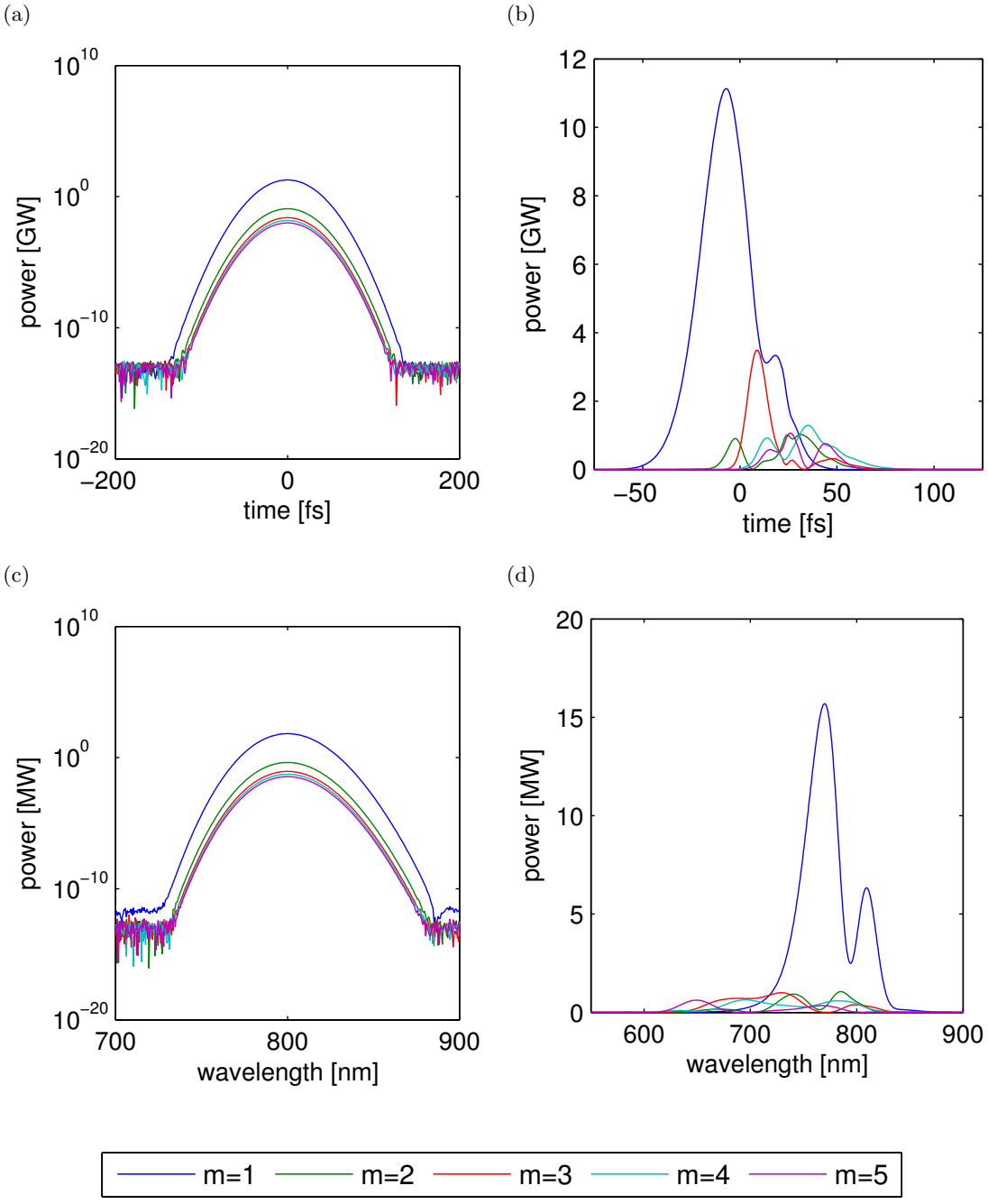

Figure 4.1: (a) and (c) The 800 μJ, 40 fs NIR pulse is coupled predominantly into the fibre $EH_{1,1}$ mode. (b) and (d) The envelopes of the $EH_{1,m}$ modes after 32 mm of propagation through a fibre with a 75 μm core radius filled with 100 mbar of argon.

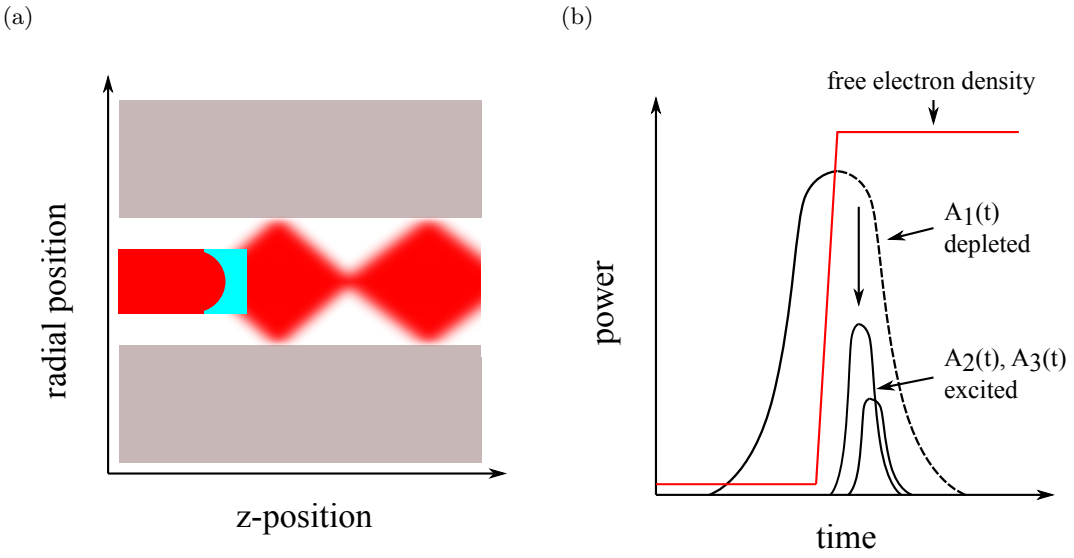

Figure 4.2: (a) The mechanism responsible for spatial compression within the fibre is analogous to a defocusing optic (the free electrons) surrounded by a long reflector (the core wall). (b) The free electron density is highly nonlinear in the presence of a strong laser field. Therefore, the 'defocussing optic' will only be seen by the trailing edge of the pulse and the deflected portion of the field (high order modes) will acquire a shortened envelope.

4.1.2 Propagation effects

Returning to the initial simulation the spatio-temporal reshaping achieved within the fibre is highly dynamical. Fig. 4.4 demonstrates the spatial HWHM (a), on-axis FWHM duration (b) and on-axis peak intensity (c) as a function of z-position. When constructing these plots and throughout the rest of this thesis the convention is used to analyse the most intense feature within the pulse at each z-position. Although this leads to discontinuities it is the most appropriate way to present the data with HHG in mind. Much of the dynamic behaviour shown here is in fact driven by linear propagation effects. Intermodal dispersion causes the relative phases of the modes to slip, modulating the spatio-temporal field calculated from the coherent sum involving all mode envelopes and mode functions, Eq. (2.17). Also, as a considerable amount of power is coupled into high order modes, their large loss influences the distance over which a short pulse can be maintained with a high intensity.

4.1.3 Alternative parameter regimes

The effectiveness of the compression mechanism across the pressure and input pulse energy parameter space will now be explored. This will allow predictions to be made and limitations identified. Fig. 4.5 (a) and 4.5 (b) show the spatial HWHM and on-axis FWHM duration as a function of the z-position and argon pressure. These simulations

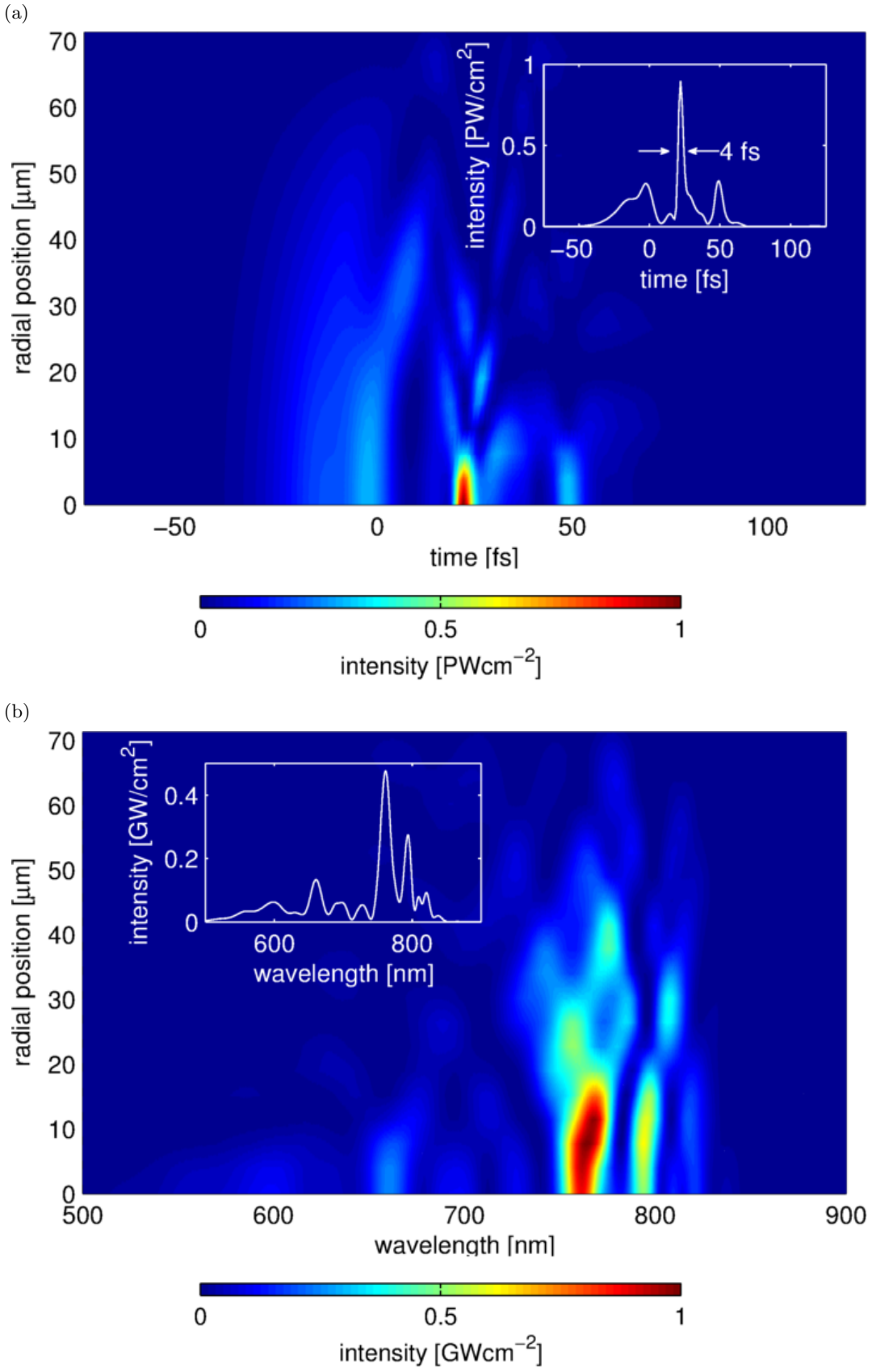

Figure 4.3: (a) and (b) The full spatio-temporal and spatio-spectral fields at the output of the fibre for the same conditions as Fig. 4.1. Here, the 4 fs self-compressed pulse at $\sim$ 20 fs contains 20% of the launched energy. The insets display the values of the on-axis field.

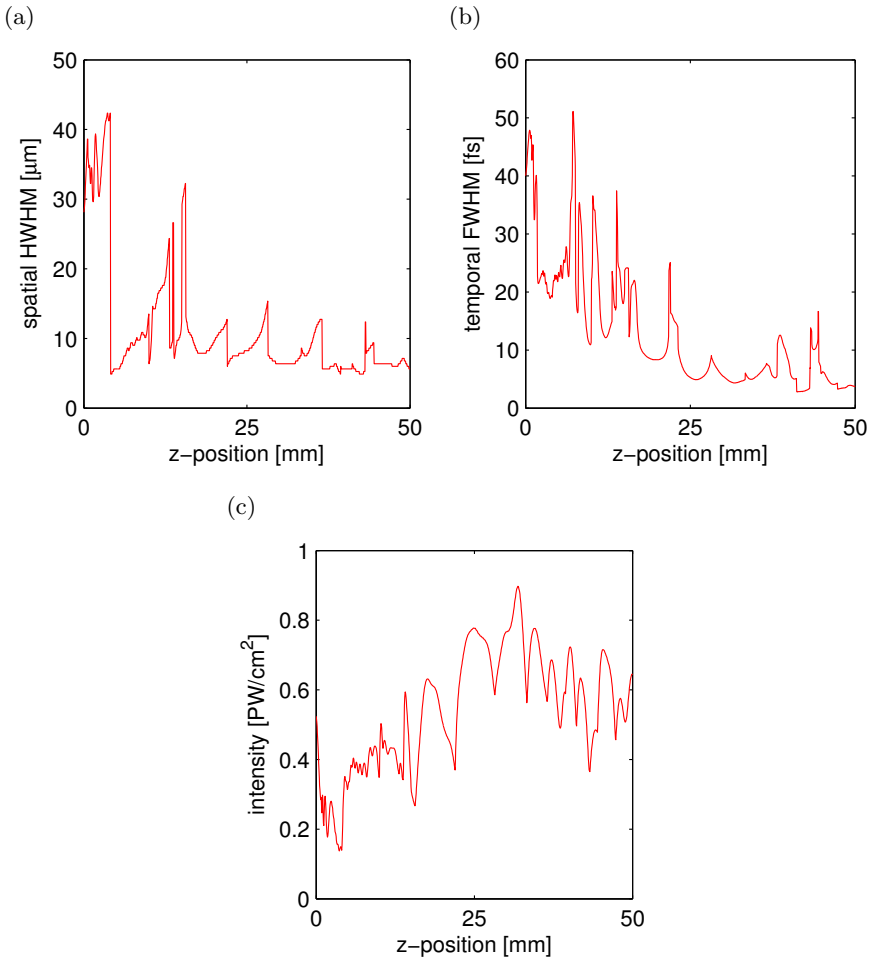

Figure 4.4: (a) Spatial HWHM, (b) on-axis FWHM duration and (c) on-axis intensity as a function of z-position. The discontinuities arise during data analysis as the most intense feature within the complex pulse is extracted. The input pulse, fibre and gas parameters are the same as those used to produce Fig. 4.1.

demonstrate the importance of generating a high free-electron density when mode coupling is the desired outcome. Fig. 4.6 (a) and (b) show the same quantities as a function of z-position and input pulse energy. Again, the plots demonstrate the importance of a high free-electron density but also highlight the nonlinearity of the photoionization process itself, producing a distinct boundary within which spatio-temporal compression is achieved. These datasets highlight the close relationship between spatial and temporal compression, and suggest that whenever bright, nonlinearly excited high order modes are observed in the far-field of an experiment then temporally compressed pulses are likely to exist within the fibre, at least in the limit of pressures where material dispersion has a negligible effect. The remaining plots, Fig. 4.5 (c) and Fig. 4.6 (c) show the on-axis intensity (normalised with respect to the launched intensity) as a function of z-position, argon pressure and input pulse energy, respectively. These plots show parameter regimes where intensities increase by 1.6-fold, and it is within these regions that the highest pulse contrast is observed. The positioning of these regions is largely governed by intermodal

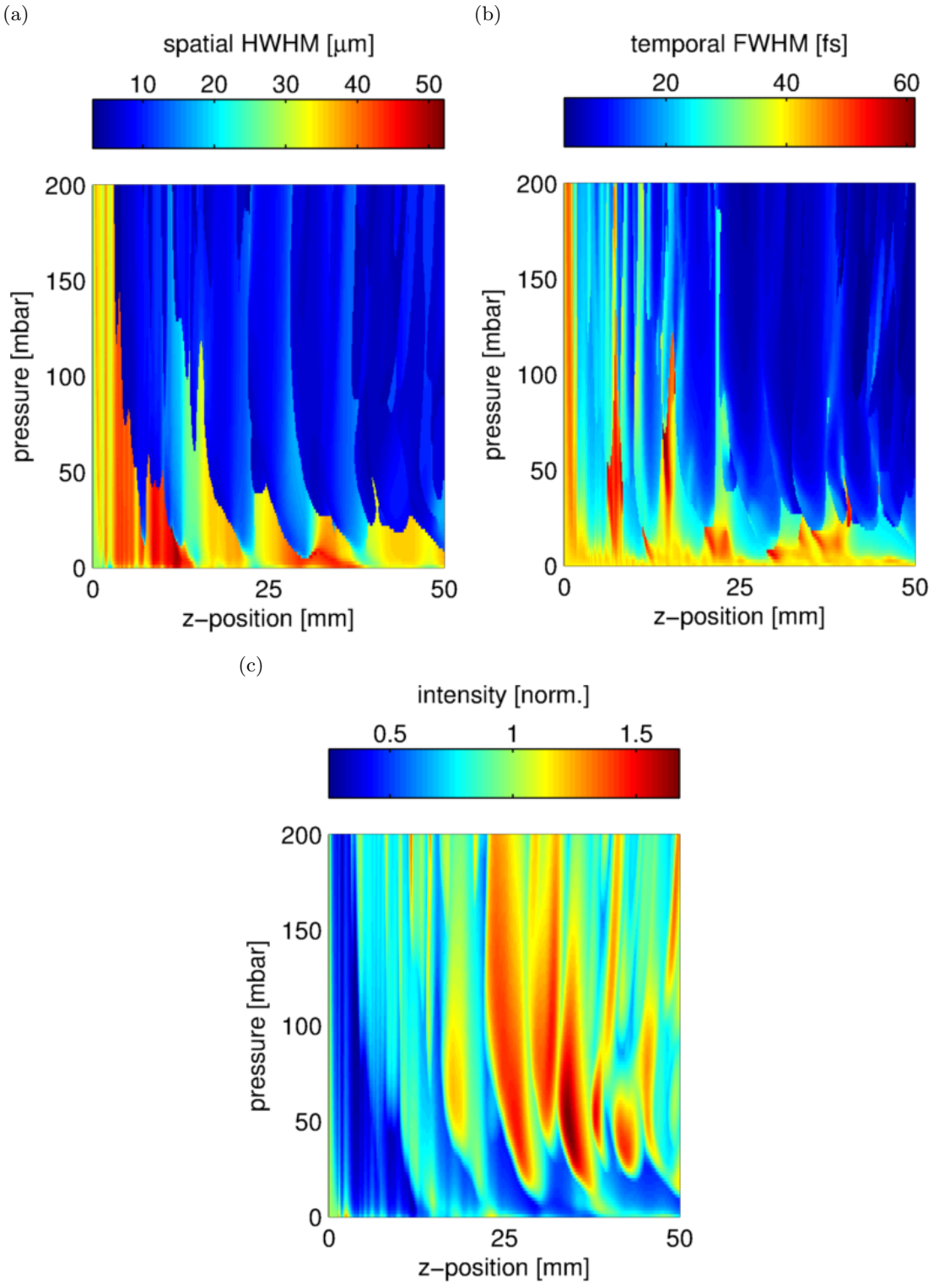

Figure 4.5: (a) Spatial HWHM, (b) on-axis FWHM duration and (c) on-axis intensity as a function of z-position and argon pressure. Here, the intensity has been normalised with respect to the launched intensity. All other parameters are identical to those used in 4.1.

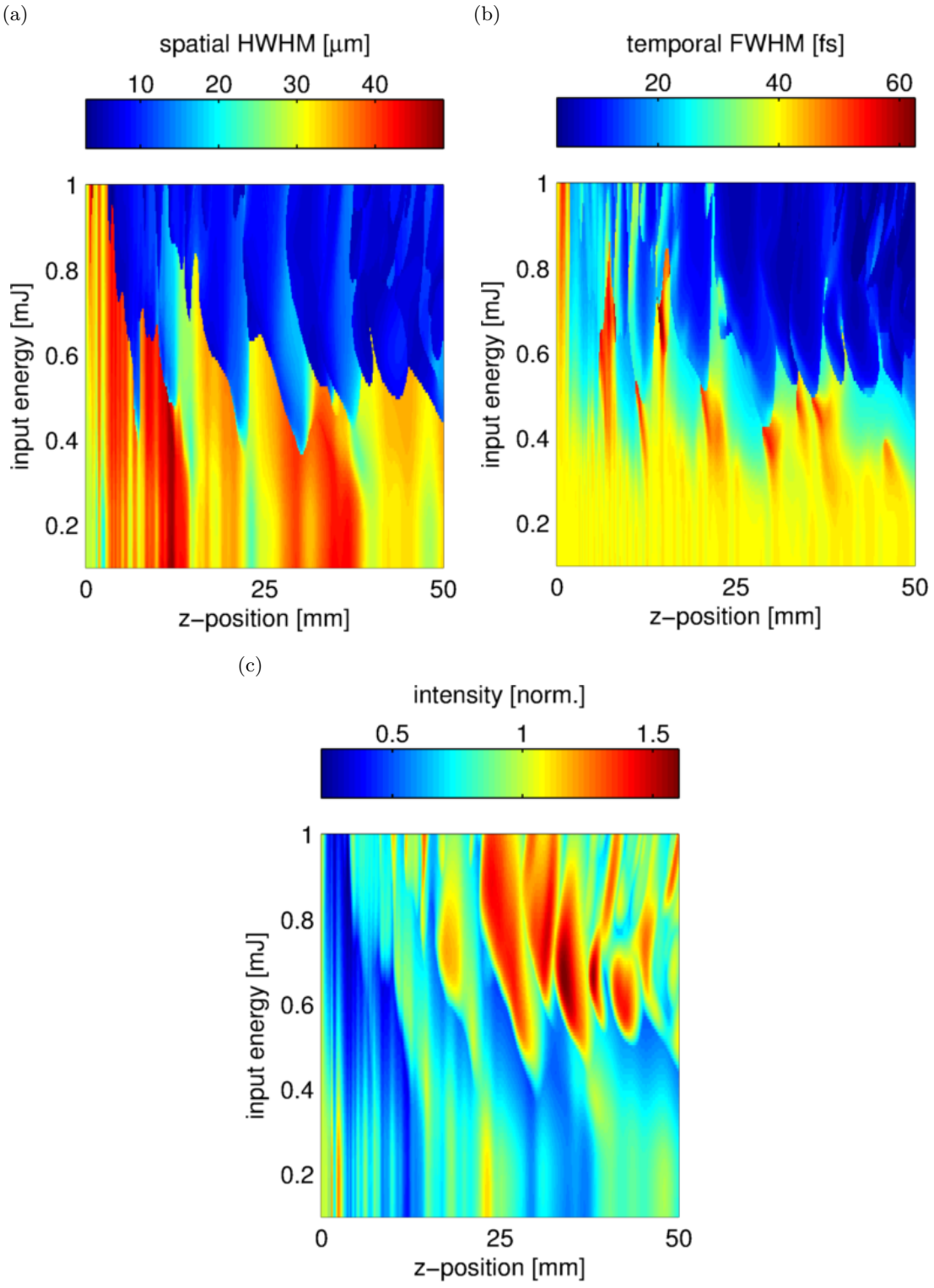

Figure 4.6: (a) Spatial HWHM, (b) on-axis FWHM duration and (c) on-axis intensity as a function of z-position and input pulse energy. This plot can be considered as a replica of Fig. 4.5 with input pulse energy being the free parameter and the argon pressure fixed at 100 mbar.

dispersion, however excessive mode coupling at high gas pressures and pulse energies is shown to spoil the pulse contrast.

4.2 Experimental study

Devices for measuring complex few-cycle pulses in both space and time are still in their infancy [33, 15, 91]. Additionally, if a pulse like the one shown in Fig. 4.3 (a) is to be measured it must first be extracted from the vacuum apparatus and delivered to the diagnostic instrument in a manner that takes account of its extreme divergence. Instead of tackling these problems head-on it was decided to take a different approach, comparing measurements taken in the far-field with appropriately propagated simulations. This simple study has led to improvements being made to the models and the observation of the key aspects of the mechanism developed in section 4.1.1.

4.2.1 Spatio-spectral field

The first measurement compared with theoretical data is the spatio-spectral field shown in Fig. 4.7 (b). This particular data set was taken by Richard Chapman and Thomas Butcher [21] using the apparatus shown in fig. 4.7 (a). Here, a 765 μJ, 41 fs pulse with a central wavelength of 790 nm is sent to the gas-filled fibre beamline described in chapter 3. The fibre used here is once again 70 mm long with a 75 μm core radius and gas inlets positioned 20 mm from each end. The fibre was filled with a peak argon pressure of 200 mbar. After leaving the fibre the broadened pulses were allowed to propagate out of the vacuum via a steering mirror, through a variable attenuator and into a fibre coupled spectrometer (Ocean Optics) that was translated across the beam. The total distance from the exit of the fibre to the spectrometer was 0.8 m. The theoretical data was propagated over this distance using a spectral method (chapter 2) and the result is shown in Fig. 4.7 (c). In terms of total spectral broadening and the radial structure and size the two compare fairly well, however the spectral structure is poorly replicated in the theoretical plot. In order to correct this it was found to be necessary to characterise the driving laser thoroughly so that realistic initial conditions could be passed to the model.

4.2.1.1 Spatial measurements of the driving laser

Measuring the spatial intensity profile of a laser is fairly simple, and typically involves passing the beam through a telescope and onto a CCD camera. Measuring the spatial profile of the phase however requires far more specialised equipment, and this property is not routinely measured outside of large scale laser facilities running adaptive optics.

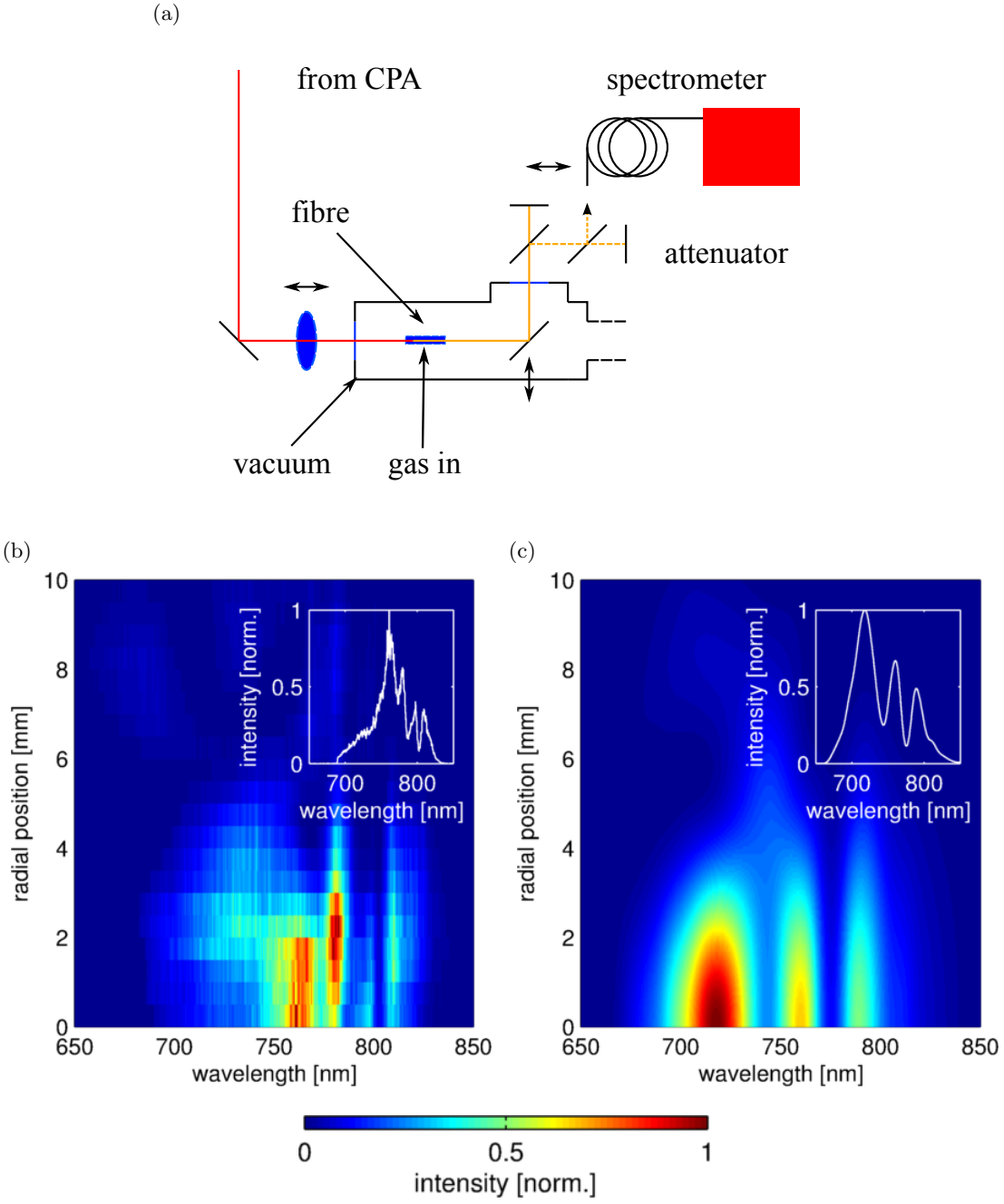

Figure 4.7: (a) The apparatus used to measure the spatio-spectral profile of pulses in the far-field. The broadened pulses pass through a variable attenuator and into a fibre-coupled spectrometer that is scanned across the beam. (b) and (c) The experimental and theoretical spatio-spectral field of a 765 μJ, 41 fs pulse with a central wavelength of 790 nm having passed through the fibre and 0.8 m of free-space. The fibre used here is the same as the one described in chapter 3 and the peak gas pressure is 200 mbar.

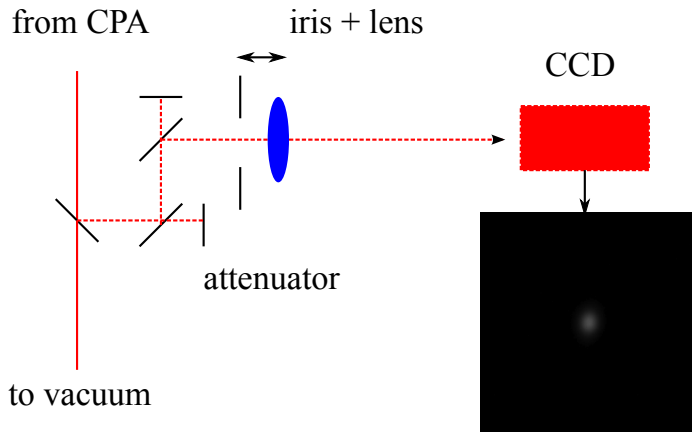

Figure 4.8: The simple wavefront sensor device constructed from an iris (near-field/pupil/etc.), thin lens and CCD camera with a high dynamic range. The far-field image is recorded and the near-field amplitudes and phases are reconstructed via iterative phase retrieval.

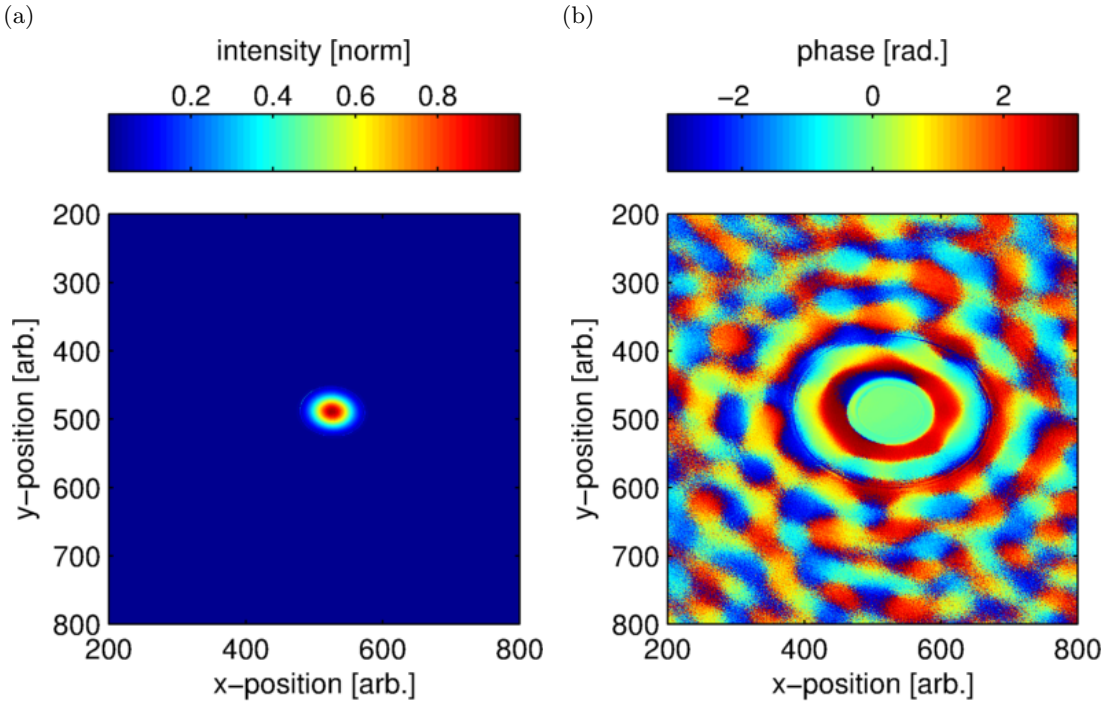

Figure 4.9: (a) The reconstructed spatial amplitudes and phases (b) at the iris. The smooth intensity profile and flat phase show that it is a reasonable assumption to launch a Gaussian beam into fibre in the model.

Unfortunately it was not possible to purchase a commercial device such as a Shack-Hartmann sensor [70] or lateral shearing interferometer [77], and instead iterative phase retrieval was used to recover the amplitude and phase of the beam from a single image recorded at the focus of a thin lens. This novel technique for analysing wavefronts has not found regular use in laser laboratories (except when posed as a microscopy problem! See chapter 1) but it is a common technique in astronomy [31].

The device constructed is shown in Fig. 4.8. Part of the CPA beam is picked-off and attenuated close to the gas-filled fibre beamline. The beam then passes though an iris positioned just before a 1.5 m focal length lens and a high dynamic range CCD camera (Princeton Instruments) records the far-field intensity distribution. Here, the thin lens is performing a Fourier transform and the iris is providing a strong near-field constraint so the phase-retrieval algorithms described by J. R. Fienup [38] can be applied directly to reconstruct the amplitude and phase at the iris. The hybrid input-output (HIO) algorithm with shrinkwrap [62] was selected to perform the reconstruction because of its desirable convergence properties. This algorithm is shown in Alg. 4.1. Initially the near-field n is populated with random amplitudes and phases and multiplied by a simple circular mask. This is then propagated into the far-field via a 2D FFT and the amplitudes are replaced by those measured with the CCD camera. The inverse 2D FFT is then taken and an error metric is evaluated. The next step is unique to the HIO algorithm as the near-field constraint is not applied rigorously, but instead some 'memory' of the previous iteration is maintained through the parameter β (which is typically set to 0.9) helping steer the solution away from local minima. Finally, the mask is updated every 20 iterations via shrinkwrap (blurring the current solution with a Gaussian kernel and thresholding) to help increase the rate of convergence.

After several hundred iterations the algorithm converges to the solution shown in Fig. 4.9. The smooth intensity and flat phase profiles measured here enable the continued use

---

1: initialisations;
2: **for** each iteration **do**
3: $f = \mathrm{FFT2}(n)$;
4: $f' = \sqrt{F}\ \mathrm{EXP}(i\ \mathrm{ARG}(f))$; ▷ Fourier constraint
5: $n' = \mathrm{IFFT2}(f')$;
6:
7: $\epsilon = \mathrm{SUM}(\mathrm{INVERT}(mask)\ n')\ /\ \mathrm{SUM}(mask\ n')$; ▷ error metric
8:
9: $n = ((\mathrm{INVERT}(mask)\ n)\ -\ (\beta\ \ \mathrm{INVERT}(mask)\ \ n'))\ +\ (mask\ n')$;
10: $mask = \mathrm{SHRINKWRAP}(n')$;
11: **end for**

Algorithm 4.1: The HIO algorithm used to reconstruct the near-field intensity and phase n from the far-field intensity data F. For simplicity shrinkwrap is applied at every iteration in this example.

of a simple Gaussian beam launch in the model. Despite not solving the discrepancies in Fig. 4.7 the diagnostic device constructed here is a very elegant one. Not only does it measure the amplitude and phase of a laser beam, but it is easy to calibrate as the iris aperture is known (enabling beam waist measurement), it also serves as a focal spot diagnostic and if necessary an M^2 parameter can be extracted by propagating the field numerically through a focus.

4.2.1.2 Temporal measurement of driving pulses

Once spatial distortions were ruled out the next measurement to take was the electric field at the entrance to the fibre. As discussed in chapter 3 the pulses emerging from the amplifier are monitored by a suit of diagnostics including a GRENOUILLE. However, on their way to the fibre the pulses pass through two beam splitters, a lens and a window. Even with an unfocussed beam nonlinearities and dispersion will be active modifying the pulses from the ideal Gaussian assumed in the model. To test this, the experiment shown in Fig. 4.10 (a) was performed with the assistance of Thomas Butcher. The CPA beam was diverted from the gas-filled fibre beamline and sent through a 3 mm thick block of fused silica (thickness matched to the lens and vacuum window), through an attenuator and into the GRENOUILLE. The pulse energy was then slowly increased and FROG traces were recorded at typical operating values. Fig. 4.10 (b) and 4.10 (c) show the reconstructed temporal and spectral amplitudes of the driving pulse used throughout this section. The measured and reconstructed GRENOUILLE traces are provided in appendix A for comparison. The FROG retrieval error of 0.00995 is acceptable for a pulse of this type.

The pulse launched into the fibre differs considerably from the Gaussian profile assumed before. When this experimentally measured field is used as the initial condition in the model the spatio-spectral profile is greatly improved (Fig. 4.11). The overall broadening and spatial profile remain an excellent match, and the spectral structure is now perfectly resolved. The apparent off-axis shift in the peak intensity seen in the experimental data is likely to be caused by a poorly calibrated attenuator or some saturation in the data and not a physical effect. Much of this structure could be removed by using a focussing mirror instead of a lens.

4.2.2 FROG measurements of fibre output

Once the pulses emerge from the vacuum apparatus the inner part of the ring pattern is dominated by power that was propagating in the fundamental mode. Measuring the temporal profile of this will allow several aspects of the mechanism described in section 4.1 to be tested. Unfortunately the commercial GRENOUILLE device used throughout this thesis would be operating beyond its specification [68] if it were to be

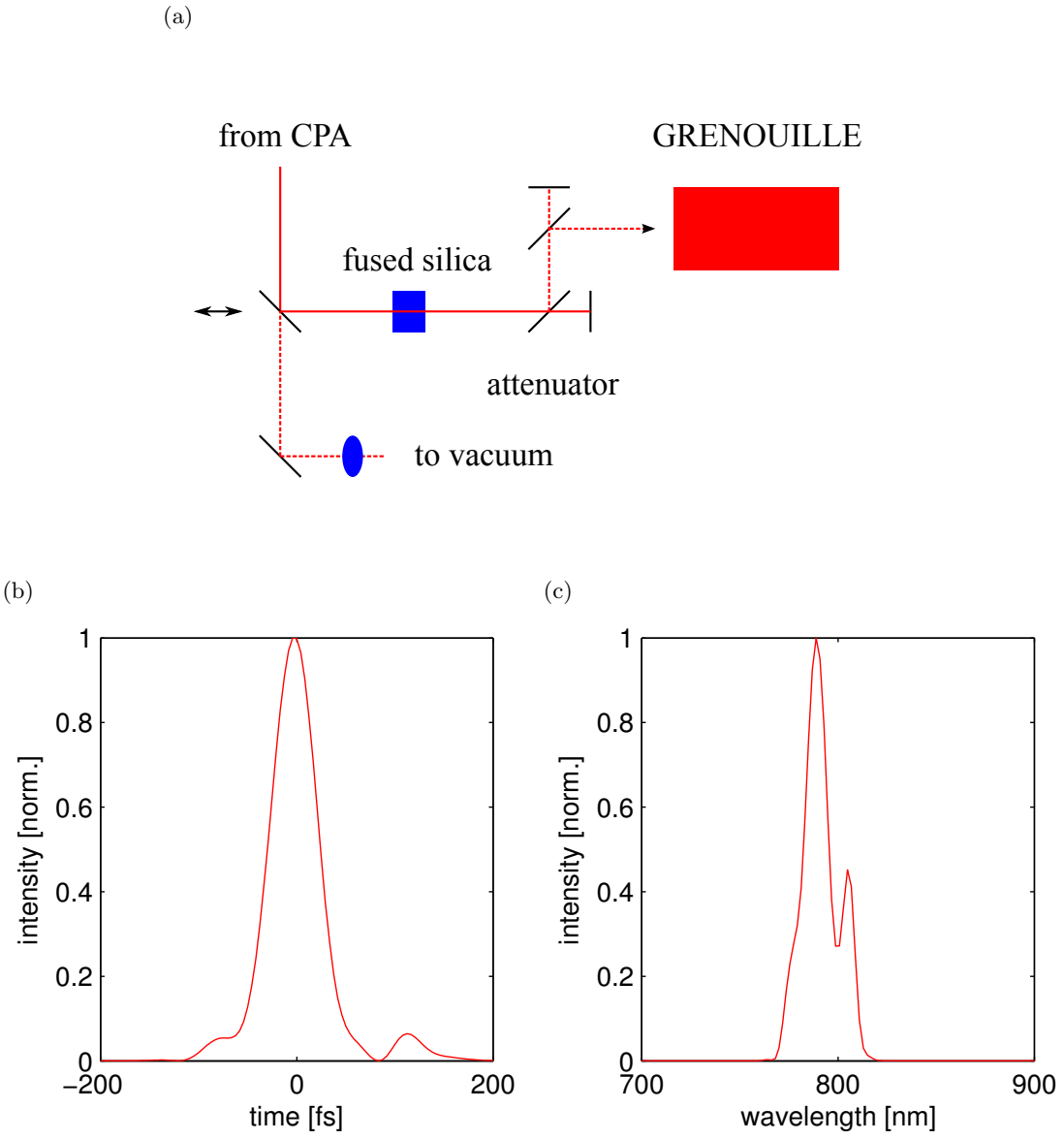

Figure 4.10: (a) The geometry used to estimate the temporal field at the input to the gas-filled fibre. The CPA beam is diverted through a block of fused silica whose thickness is matched to the glass in the gas-filled fibre beamline. The beam then passes through an attenuator and into a GRENOUILLE device. (b) and (c) The experimentally measured temporal and spectral intensity after the pulse of interest has propagated though 3 mm of fused silica. The measured and reconstructed GRENOUILLE traces are provided in appendix A for reference.

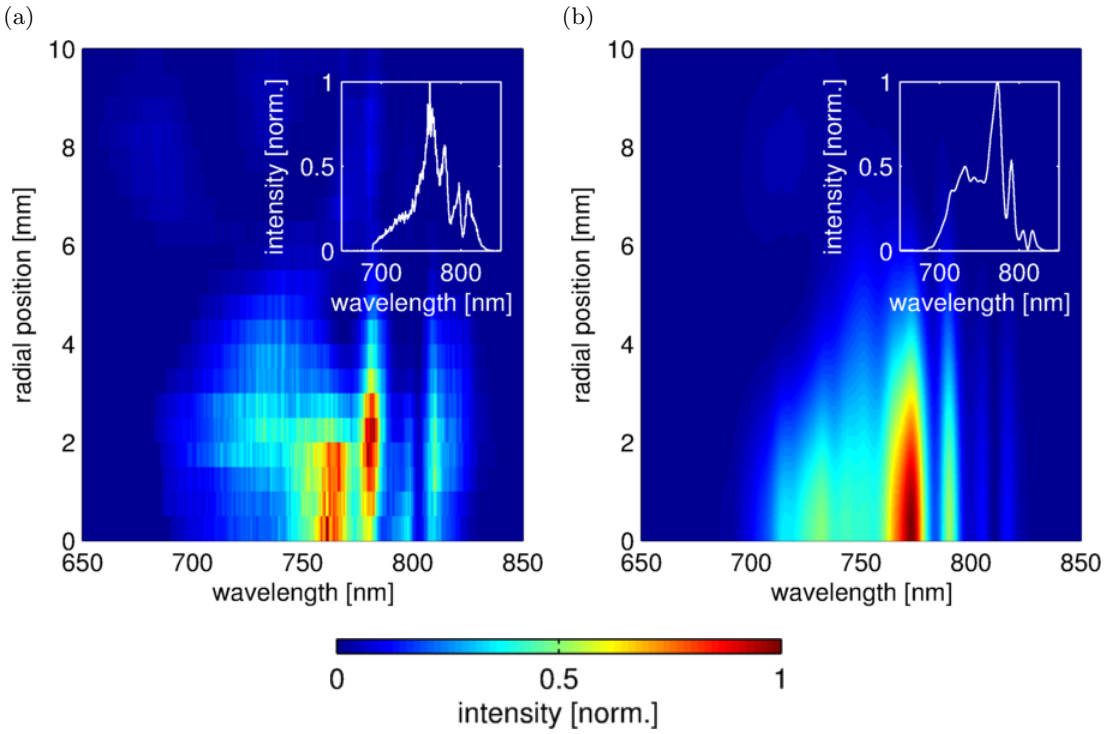

Figure 4.11: (a) The experimental spatio-spectral data replicated from Fig. 4.7 (b) The corresponding theoretical plot having used the GRENOUILLE data in the initial conditions. All of the features observed experimentally now appear in the theory.

used to measure these pulses. Instead the single-shot SHG FROG shown in Fig. 4.12 was borrowed from the Artemis facility at the Rutherford Appleton Laboratory. This device works as follows: the pulses enter through the aperture A1 and are divided by the beamsplitter BS1, where half of the power is sent into the delay line DL. Pulses from the two arms are then directed onto the cylindrical mirror CM such that the foci cross at an angle within the 10 μm thick BBO crystal. This is an important aspect of the geometry as it maps delay onto the spatial coordinate enabling single-shot measurements to be made. The second harmonic exits the crystal and is collimated by the lens L1 before being steered into the imaging spectrometer SP. The device also includes a fused silica window on a flip mount (FS) to test for time ambiguities and an additional beamsplitter BS2 to balance dispersion in the two arms.

The device was positioned in place of the fibre-coupled spectrometer in Fig. 4.7 (a) and A1 was closed to remove any spatial structure that may be misinterpreted as delay. The two arms were carefully aligned, crossed in the crystal and the delay was adjusted to maximise SHG. The second harmonic was then aligned onto the slit of the imaging spectrometer and the CCD camera was used to record a series of SHG FROG traces at various input pulse energies (see appendix A). Ambiguities were checked, temporal and spectral calibrations were taken and the SHG FROG traces were reconstructed using commercial software (see appendix A). Finally, the spectral phase was modified to take

into account the vacuum window, air and beamsplitters. The results are compared with theory in Fig. 4.13 where the launched pulse energy is 100 μJ in (a) and (b), 500 μJ in (c) and (d) and 1 mJ in (e) and (f). The fibre shares its design with the one used for spatio-spectral measurements and is filled with a peak argon pressure of 100 mbar. The comparison between experiment and theory is once again striking and these temporal measurements demonstrate several of the effects outlined in section 4.1. An example of this is the steepening of the trailing-edge of the pulse where power has been rapidly coupled into high order modes. The FWHM durations of the pulses in Fig. 4.13 are listed in Tab. 4.1. The discrepancy between the measured and simulated pulse duration for a 500 μJ input may be attributed to a poor FROG reconstruction. The FROG retrieval errors of 0.01004, 0.01973 and 0.0258 are acceptable when measuring complex pulses like these, however the reconstruction at 500 μJ (see appendix A) captures less of the detailed structure when compared with the 1 mJ result.

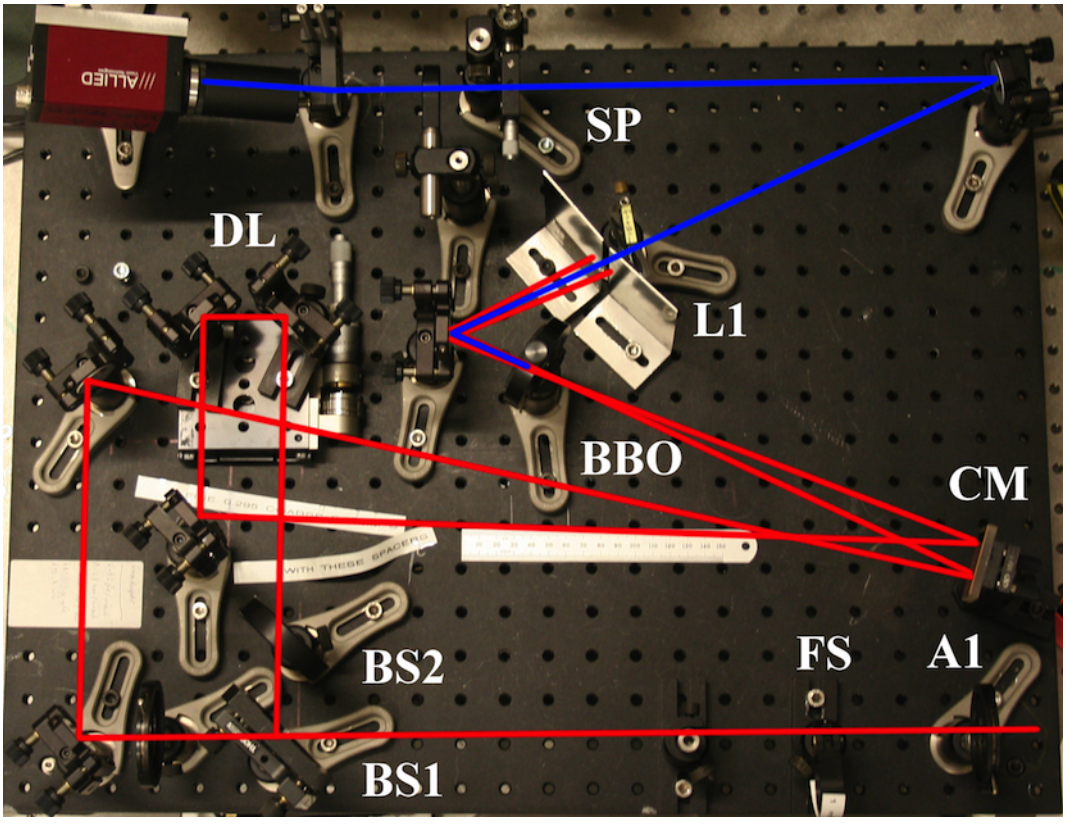

Figure 4.12: The FROG device used to characterise the pulses emerging from the gas-filled fibre. The pulse enters through the aperture A1 and then gets divided by the beamsplitter BS1. One replica then travels through the delay line DL, and both are directed onto the cylindrical mirror CM such that they cross within the 10 μm thick BBO crystal. The second harmonic is then collimated by the lens L1 and directed into the imaging spectrometer SP. The other two components labelled are a fused silica window FS on a flip mirror to examine the time ambiguity and a second beamsplitter BS2 to balance the dispersion.

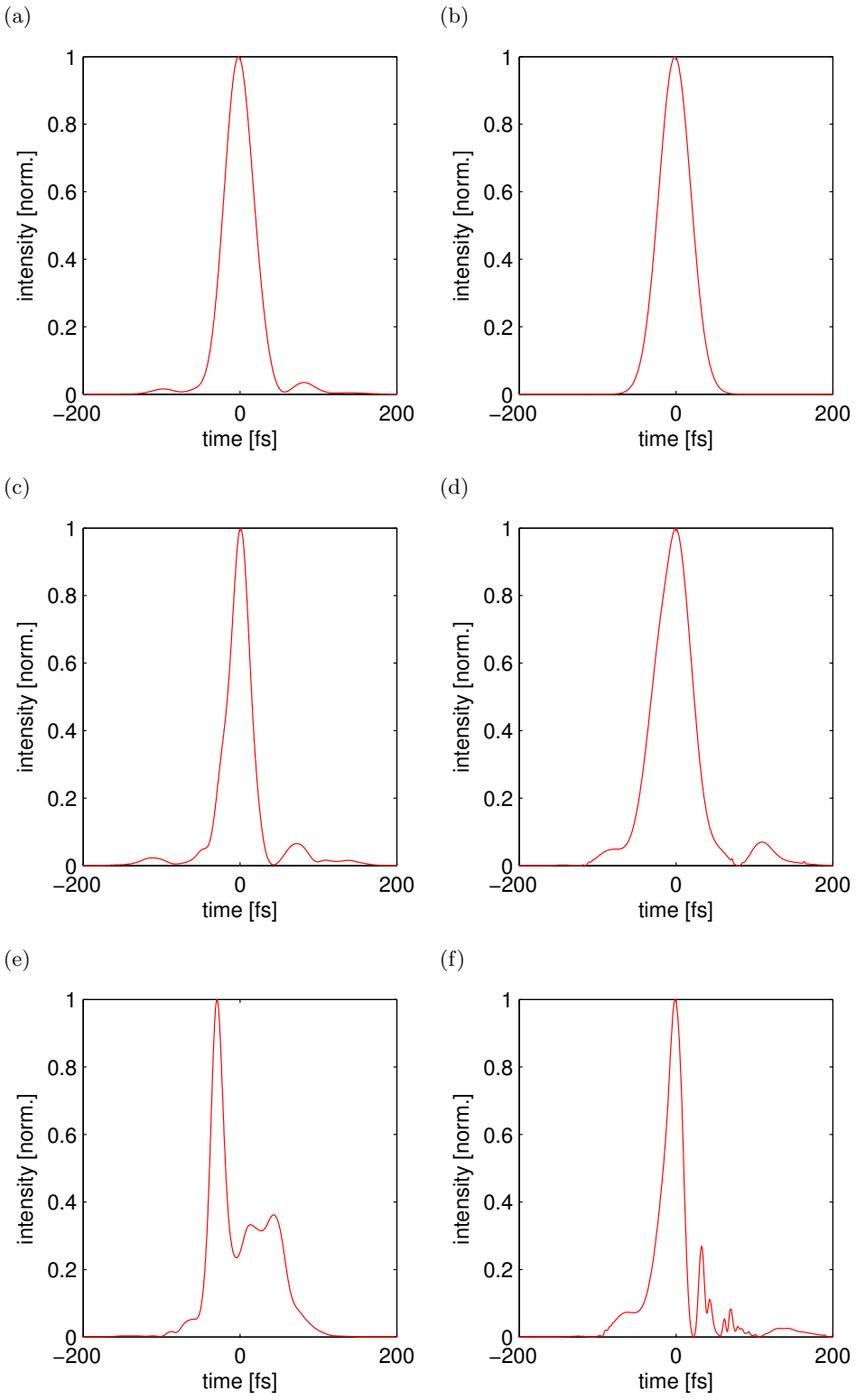

Figure 4.13: (a), (c) and (e) The experimentally measured far-field pulse shape for 100 μJ, 500 μJ and 1 mJ input pulses. (b), (d) and (f) The corresponding theoretical results. The fibre shares its design with the one used in the spatio-spectral study and in this instance it was filled with a peak argon pressure of 100 mbar.

Input pulse energy [μJ]	Experimental FWHM duration [fs]	Theoretical FWHM duration [fs]
100	47.1	47.0
500	29.3	50.7
1000	21.4	24.0

Table 4.1: The FWHM durations of the experimental and simulated pulses shown in Fig. 4.13.

4.3 Simulations from the VIS to MIR

For the penultimate set of simulations the influence of the driving wavelength on the spatio-temporal compression mechanism is studied. This is of interest because of current shifts in the high field community away from the NIR and towards VIS and MIR wavelengths. High energy pulses throughout this region are being made available by efficient wavelength conversion modules (harmonic generation and optical parametric amplifiers) and laser systems utilising the optical parametric chirped pulse amplification (OPCPA) technique or novel gain media (Tm).

For this set of simulations the fibre is once again 50 mm long with a 75 μm core radius and is uniformly filled with 100 mbar of argon. The input pulse energy is 1.5 mJ, the FWHM duration is 100 fs and the wavelength is varied between 500 nm and 2000 nm. The results are shown in Fig. 4.14. The format here is similar to previous plots of this type, (a) shows the spatial HWHM, (b) the on-axis FWHM duration and (c) the on-axis intensity as a function of z-coordinate and central wavelength. Again a clear correlation between the excitation of high order modes and temporal compression is seen. The parameter space where spatio-temporal compression can be achieved is extensive, and high contrast examples are given in Fig. 4.15 (a) at 1500 nm and Fig. 4.15 (b) at 500 nm. Changing the wavelength while keeping the fibre radius constant impacts the intermodal dispersion and linear losses. An order of magnitude change in loss across the simulations begins to limit spatio-temporal compression and intensities over long propagation lengths at MIR wavelengths.

4.4 Compression of 100 μJ few-100 fs NIR pulses

An interesting and timely application for this technique is the compression of 100 μJ few-hundred fs pulses delivered by compact ytterbium-doped fibre CPA systems. The high repetition rates achievable from such architectures are of interest to the high field community because of the enhancements in signal yield they could bring and new opportunities they could open up, such as performing metrology with XUV frequency combs [12]. Simulations in this parameter regime may also be applicable to pulses delivered by

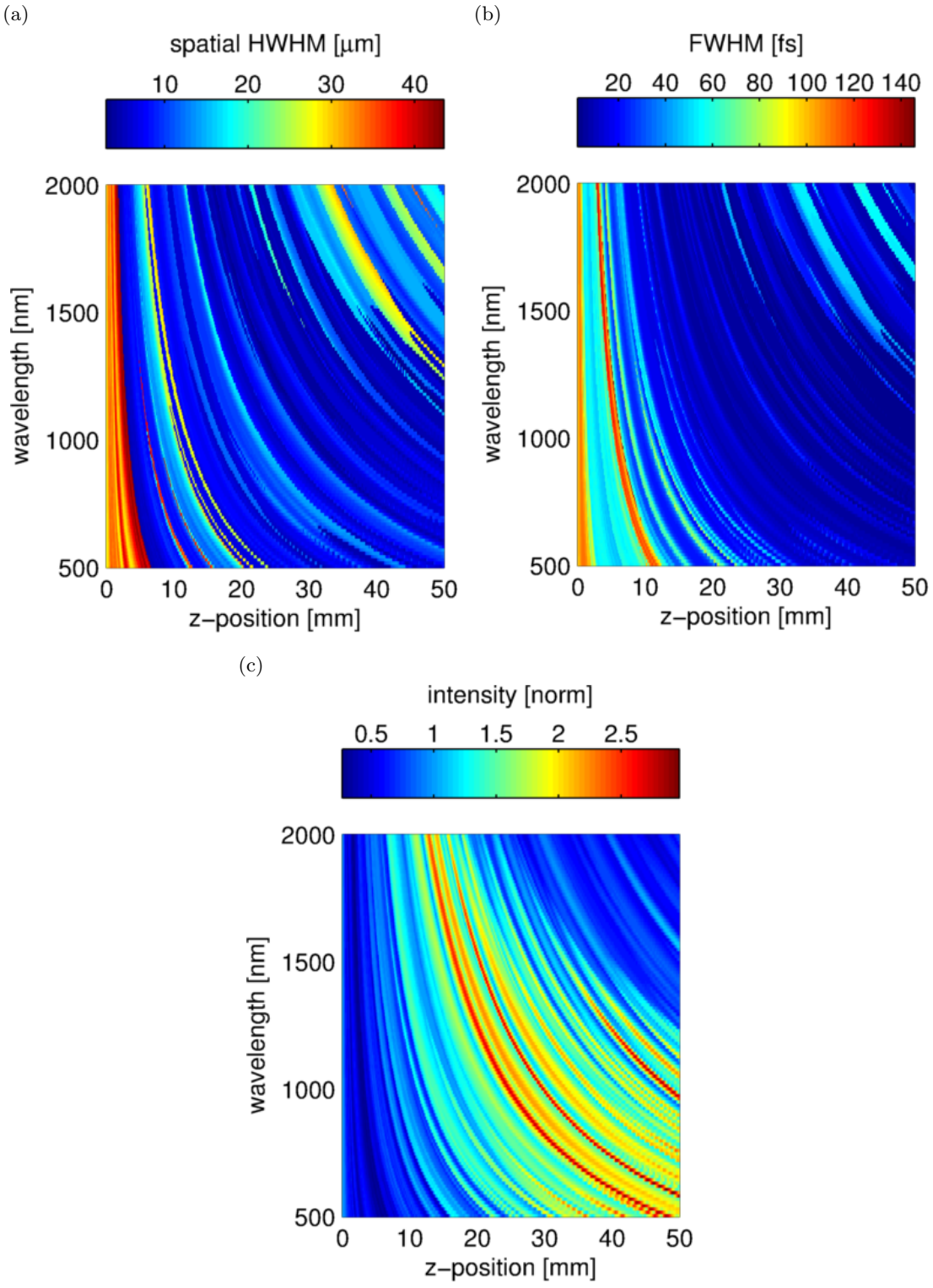

Figure 4.14: (a) Spatial HWHM, (b) on-axis FWHM duration and (c) on-axis intensity as a function of z-position and central wavelength. The input pulse energy is 1.5 mJ, the FWHM duration is fixed at 100 fs and the fibre has a 75 μm core radius and is filled uniformly with 100 mbar of argon.

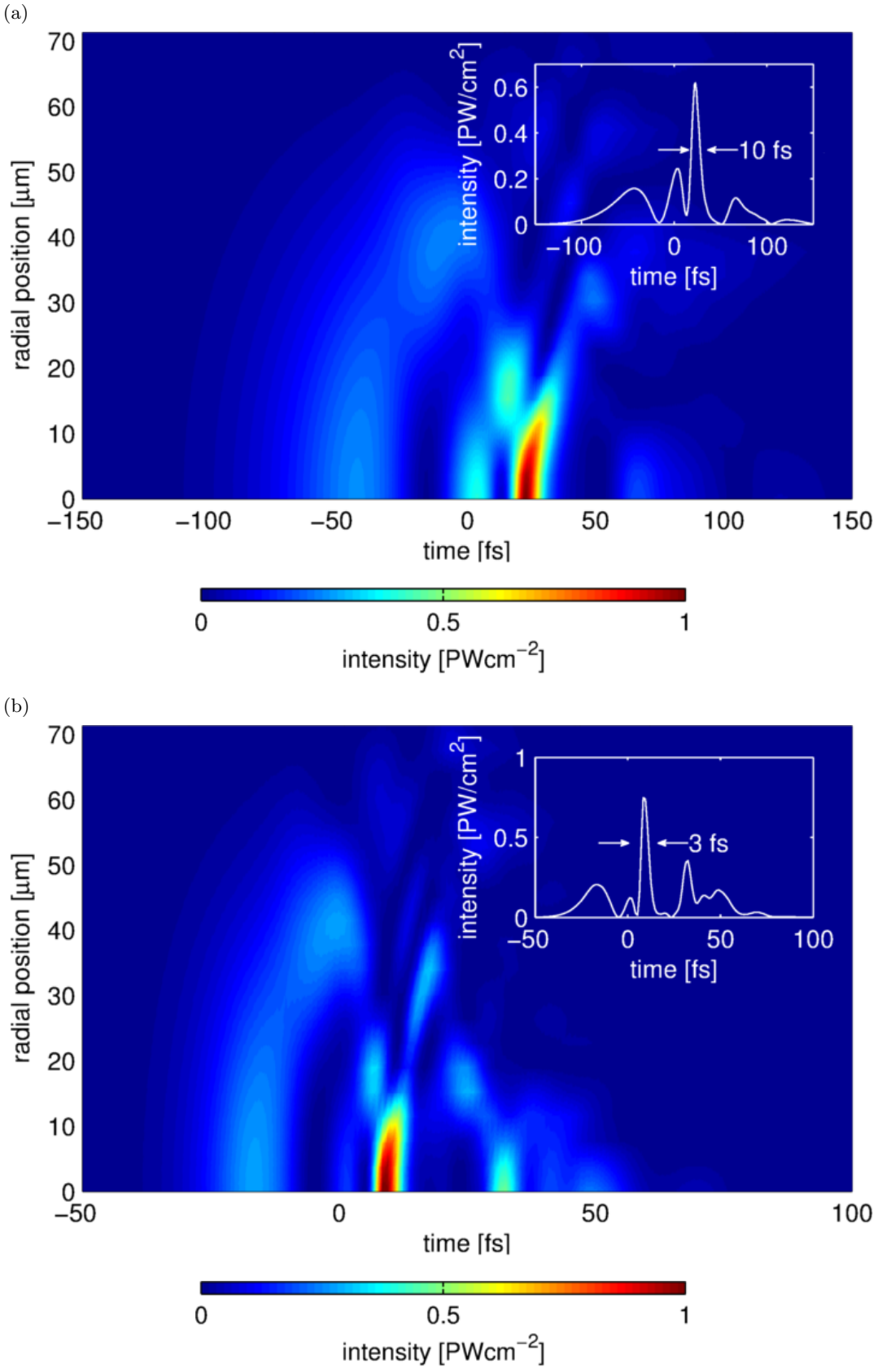

Figure 4.15: (a) High contrast example of the spatio-temporal compression of a 1500 nm pulse. (b) Another high contrast spatio-temporally compressed pulse. This time the central wavelength is positioned 500 nm.

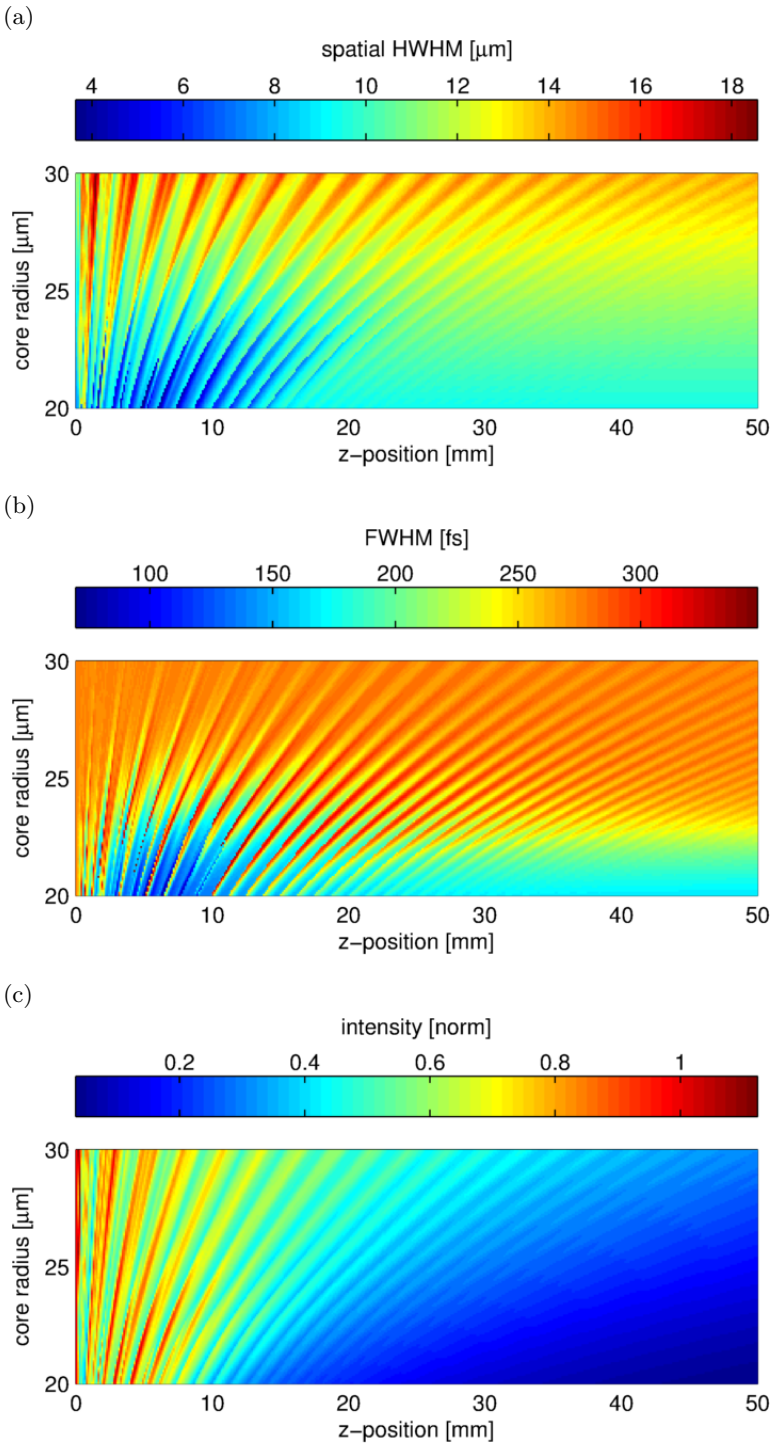

Figure 4.16: (a) Spatial HWHM, (b) on-axis FWHM duration and (c) on-axis intensity as a function of z-position and core radius. The input pulse energy is 100 μJ, the FWHM duration is fixed at 275 fs and the central wavelength is 1050 nm. The core is filled in a uniform fashion with 200 mbar of xenon.

high repetition rate regenerative amplifiers, thin-disk lasers, slab amplifiers and certain coherent combination arrangements.

Activating the compression mechanism developed in section 4.1.1 for initial conditions of this type is not straightforward because of the greatly reduced peak powers delivered by such driving lasers. Several alterations are needed in order to produce a large step in refractive index via ionization. First, the gas must be exchanged for one with lower ionization potentials. For these simulations xenon has been selected, but more exotic gaseous species may prove to be an interesting alternative if their nonlinear polarizations and ionization rates can be accurately modelled. This change is not enough to produce high free electron densities, so the fibre must also be switched for one with a smaller core to increase the field strength. For these simulations the pulse energy is 100 μJ, the FWHM duration is 275 fs and the central wavelength is 1050 nm. The core radius of the fibre is varied between 20 μm and 30 μm and the xenon pressure is fixed at 200 mbar to maximise the potential for generating a high free electron density. The results of these simulations are given in Fig. 4.16. The spatial HWHM in (a), the on-axis FWHM duration in (b) and the on-axis intensity in (c) are plotted as a function of the z-position and the core radius. In order to observe extensive coupling into high order modes and the temporal compression that this has been shown to herald, core radii must be kept below 22.5 μm for the chosen pulse energy. Within such fibres 275 fs pulses can be compressed to 69 fs after 5 mm of propagation. As the size of the core is reduced the propagation becomes increasingly dynamic early in the fibre. The pulse then undergoes a stabilisation, maintaining a FWHM duration of 165 fs throughout the remainder of the propagation. In order to explain the physical origins of these two regions it is helpful to study the modal propagation constants over a broad range of core diameters (Eq. (2.26)). The increase in separation between real parts at small core radii leads to short characteristic beat lengths and the strong interference patterns seen in 4.16. When the imaginary parts are compared with earlier simulations a difference of 2 orders of magnitude is observed, and such a large increase in linear loss causes the apparent stabilisation of the pulse after $\simeq$ 20 mm of propagation. The lack of significant enhancement of on-axis intensity is due to these large losses, and in this region the pulse is contained predominately within the steepened fundamental mode. In future theoretical and experimental this will be overcome by incorporating low-loss microstructured fibres [29, 27, 41] into compressor designs.

4.5 Conclusions and outlook

In this chapter a new mechanism has been discovered to self-compress energetic many-cycle laser pulses to few cycle durations within short gas filled-fibres. The mechanism produces pulse contrasts similar to those observed from filaments but at significantly lower gas pressures, enabling HHG to be performed within the compressor device itself

(a) (b)

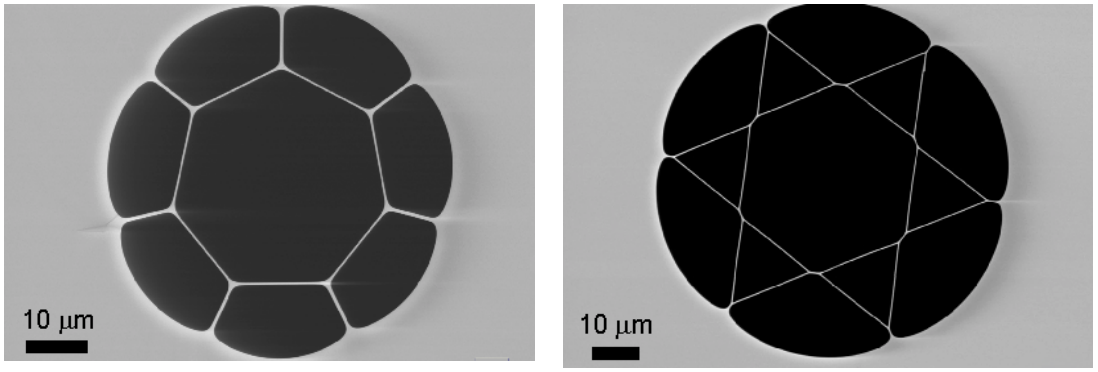

Figure 4.17: 4.16(a) and 4.16(b) Low-loss hollow-core microstructured fibres fabricated at the University of Southampton (reproduced from [71]). These have been incorporated into the nonlinear pulse propagation models developed in chapter 2 and the impact on the spatio-temporal reshaping is being explored.

(as will be discussed in the next chapter). Spectrometer and SHG FROG measurements were then taken in the far-field, and once the true initial conditions had been found and incorporated into the model an excellent match between theory and experiment was achieved. In the final two sections novel wavelengths (VIS to MIR) and pulses delivered by high repetition rate fibre laser systems were explored. The compression mechanism may be extended to both of these regimes, however high fibre losses can become a limiting factor at long wavelengths and small core radii. In future work this will be addressed by replacing the simple capillary-type fibre with a Southampton fabricated microstructured fibre like those shown in fig 4.17 [71], where losses can be three orders of magnitude lower. Fibres of this type have now been included in the pulse propagation models developed in chapter 2 and work is ongoing to understand how the low fibre loss modifies the spatio-temporal reshaping.

Chapter 5

Optimised HHG with self-compressed pulses

This chapter is based on [18], and some preliminary computational results have been added examining the XUV field in the time-domain.

For the final results chapter the spatio-temporal reshaping mechanism developed in chapter 4 will be used to optimise characteristics of high harmonics generated in-situ. In the first section the XUV flux is optimised by taking advantage of the enhanced phase-matching achieved when driving HHG with few-cycle laser pulses. The optimised fibre is then fabricated and integrated into the apparatus developed in chapter 3 and the measured flux at $30 - 40$ nm is shown to be amongst the highest ever reported. The second characteristic of interest is the temporal structure of the XUV leaving the fibre. Sophisticated simulations are performed using the models developed in chapter 2, and a high-contrast few-cycle driving pulse is synthesised. The XUV field is simulated and propagated through a thin titanium filter and a near-isolated XUV pulse with a duration of 250 as is the result.

5.1 Enhanced HHG at high gas pressures

In order to achieve a high XUV flux some degree of phase-matching must be achieved. At low gas pressures the methods outlined in chapter 1 are often successful. These schemes rarely operate close to the absorption limit so considerable increases in flux are on offer simply by working at higher gas pressures, provided the free electron density can be kept sufficiently low. In this section this is achieved by designing, fabricating and implementing a new gas-filled fibre that compresses the driving pulse to a few-cycle duration throughout an absorption limited region close to its exit.

5.1.1 Phase-matching and few-cycle pulses

As has been mentioned previously it is a high free electron density that limits the length over which HHG can be phase-matched. This problem is insuperable at gas pressures between 50-200 mbar if the driving pulse consists of many cycles. This is demonstrated in Fig. 5.1 (a) where a 4×10^{14} W/cm^2 40 fs NIR pulse is interacting with an argon atom. Here, the harmonic of interest (~ 30 nm) will be generated close to the peak of the pulse and this will therefore experience the free electron density already generated by the leading edge. This has a dramatic effect on phase-matching and the results of a simple calculation performed to illustrate the coherence length at a gas pressure of 50 mbar are shown in Fig. 5.1 (b). To overcome this issue it is necessary to replace the driving pulse with a waveform whose leading edge is incredibly steep. The few-cycle pulses produced via self-compression in the previous chapter are a good approximation of this, and an idealised (Gaussian) case is shown in Fig. 5.2. For an identical peak intensity the use of a 4 fs driving pulse enables the coherence length to be extended close to the absorption length of the gas. This simple mechanism will now be used to deliver an unprecedented XUV flux in a simple and compact geometry.

5.1.2 Fibre optimisation procedure

The fibre design used thus far in this thesis (a 70 mm length with gas inlets positioned 20 mm from each end) was chosen long before any advanced theoretical capabilities had been developed. When characterising the XUV output of this fibre in chapter 3 it was concluded that it was poorly phase-matched, and when compared to the results of other groups the flux at $30 - 40$ nm is indeed low [79]. To improve this a new fibre was designed using the advanced numerical models developed in chapter 2. The optimised design exploits the self-compression scheme outlined in chapter 4 to enhance the phase-matching of the harmonics falling between $30 - 40$ nm at high gas pressures.

5.1.2.1 Gas density profile

Wherever simulations were compared to experimental measurements in the previous chapters the gas density profile was also matched to the one supported by the fibre mounted in the vacuum apparatus. This would be very difficult to measure and instead it was calculated by Matthew Praeger using the computational fluid dynamics package ANSYS CFX (ANSYS, inc.). The density profile was found to take a general form, maintaining a constant value between the two gas inlets, followed by a sharp drop to an intermediate pressure and then a linear gradient to either end of the fibre. An example (normalised) is shown in Fig. 5.3. Note that the discontinuities at the inlets have been softened, as this is a requirement of the numerical models. This profile is in good

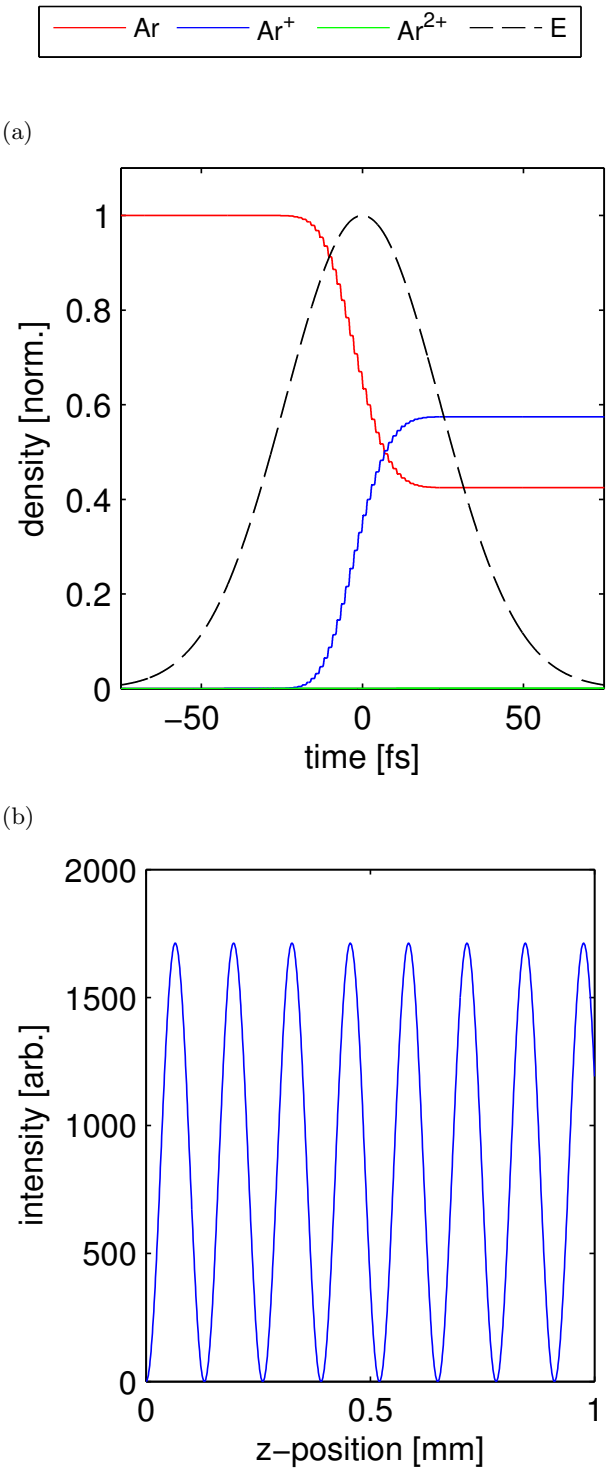

Figure 5.1: (a) The density of argon and its ions when interacting with a 4×10^{14} W/cm^2 40 fs NIR pulse. (b) The results of a simple phase-matching calculation for the same laser parameters and a 50 mbar argon pressure. The coherence length of 30 nm XUV is demonstrated to be $< 100\mu$m.

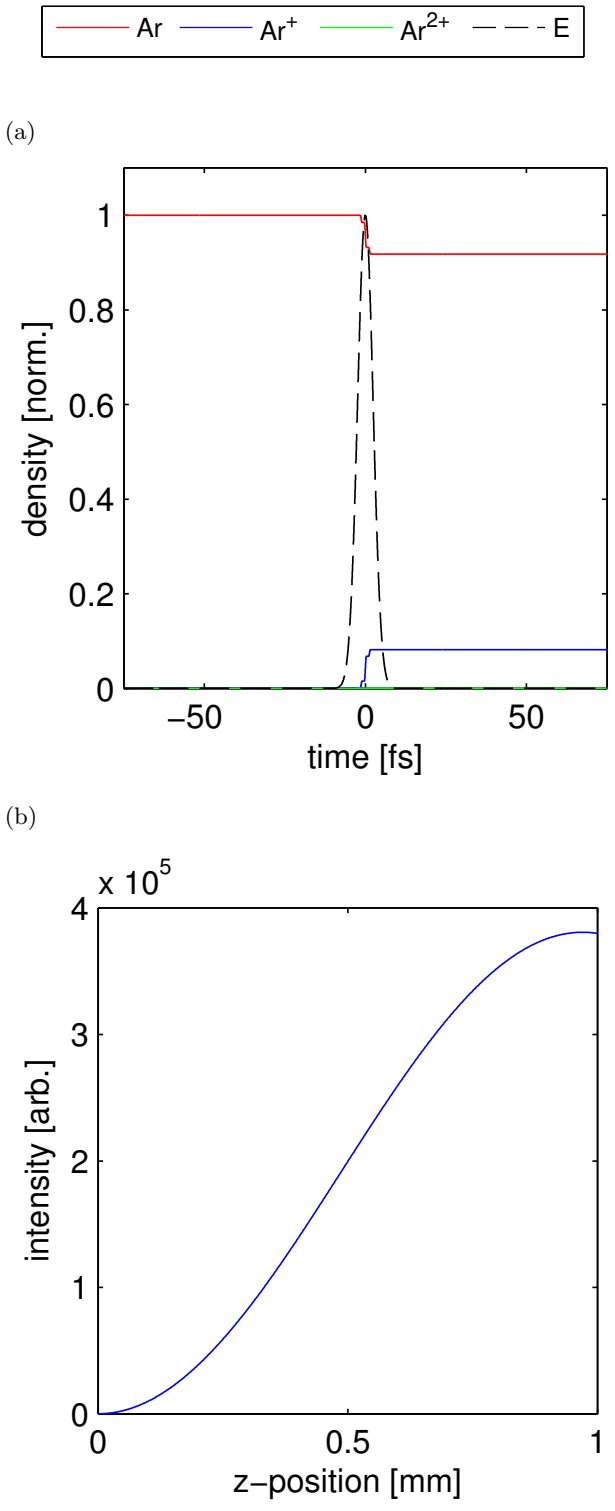

Figure 5.2: Replica of 5.1 for a few-cycle driving pulse of equal peak intensity. The reduced free electron density makes it possible to extend the coherence length towards the absorption length of the gas.

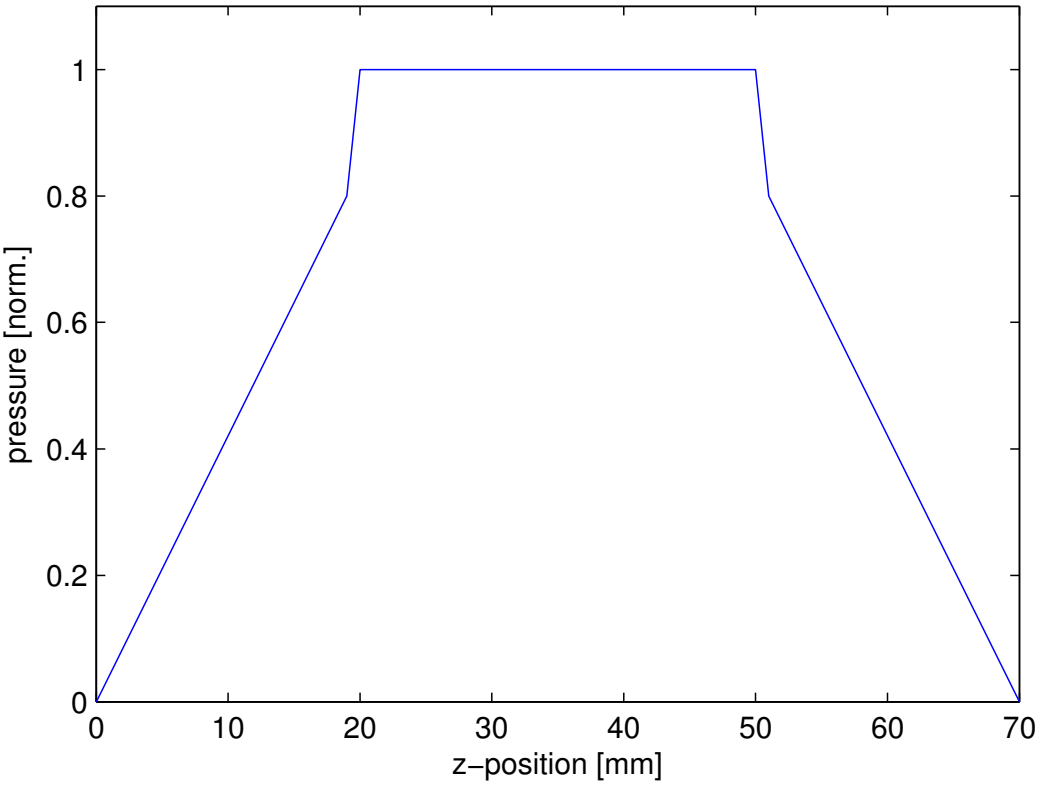

Figure 5.3: The typical gas density profile used when simulating a real fibre. The two steep features arise at the gas inlets and the pressure falls linearly towards the entrance and exit of the fibre.

agreement with images taken of the argon ion florescence along the length of the fibre [39].

The positioning of the gas inlets is a free parameter when designing a new fibre so the influence of a gas density gradient on the spatio-temporal reshaping was explored. Fig. 5.4 (a) and (b) show the on-axis FWHM duration and peak intensity as a function of z-position for an 800 μJ, 40 fs NIR pulse launched predominantly into the fundamental mode of a fibre with a 75 μm core radius uniformly filled with 100 mbar of argon. These figures are similar to those in chapter 4 and again the discontinuities arise from analysing the most intense feature at each z-position. Fig. 5.4 (c) and (d) are identical except for a gas density gradient being applied from the entrance of the fibre to its exit. This changes the dynamics within the fibre considerably. Extensive mode coupling can no longer take place early in the fibre and many of the features, such as the positioning of the transition to a few-cycle duration are altered making this an interesting parameter in any optimisation procedure.

In contrast Fig. 5.4 (e) and (f) show that the dynamics are fairly consistent when a gradient is induced from the entrance of the fibre to its exit. This helps simplify the optimisation procedure, and the gas inlet should be located as close as possible to the fibres exit in order to maintain a high gas density. This is essential for achieving a flux

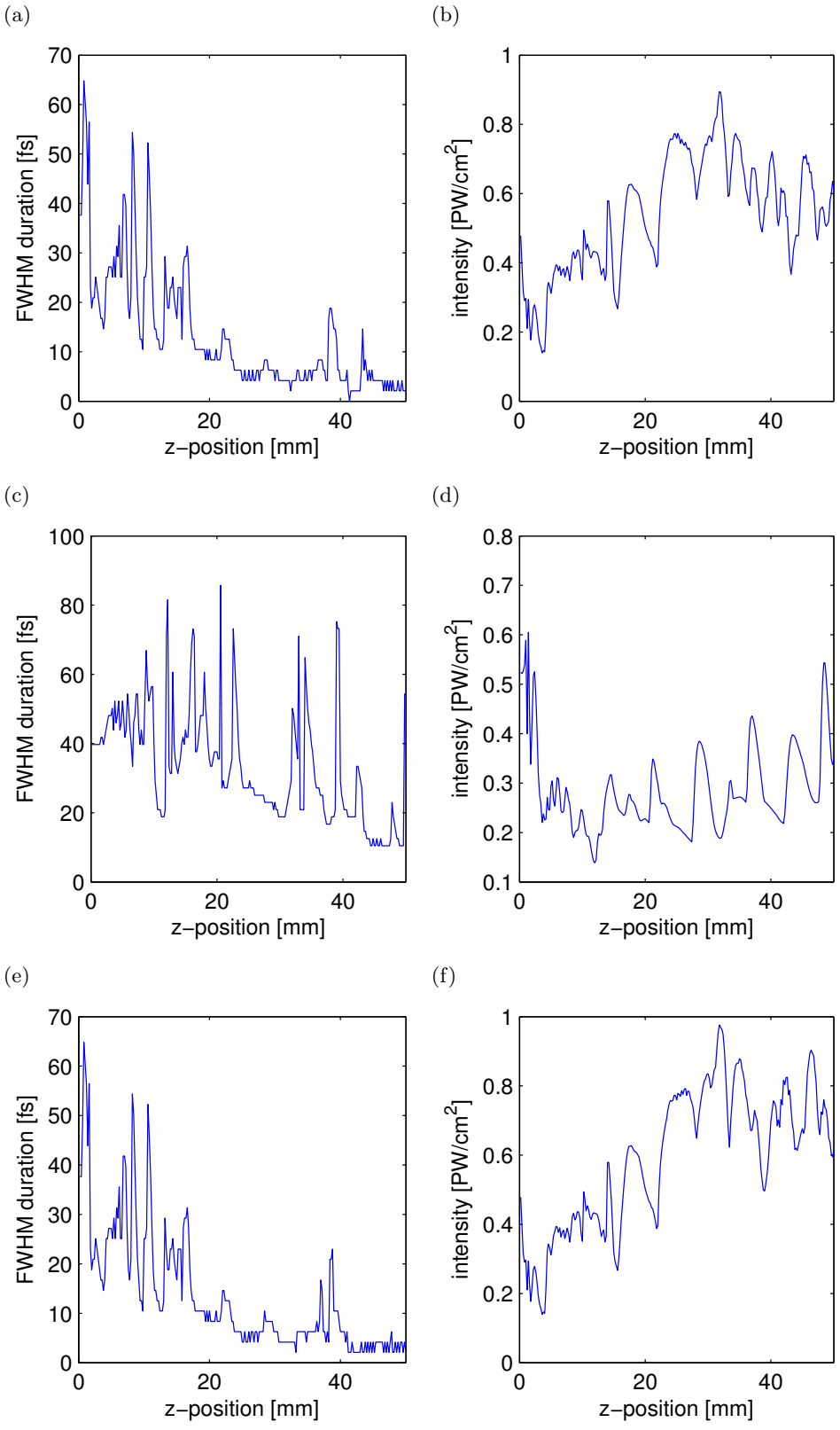

Figure 5.4: The on-axis FWHM duration (a) and peak intensity (b) of a 800 μJ, 40 fs NIR pulse coupled predominantly into the fundamental mode of a fibre with a 75 μm core radius filled uniformly with 100 mbar of argon. (c) and (d) Here, the gas density rises linearly from the fibre entrance to the fibre exit. (e) and (f) In this case the gas density falls linearly from the fibre entrance to the fibre exit.

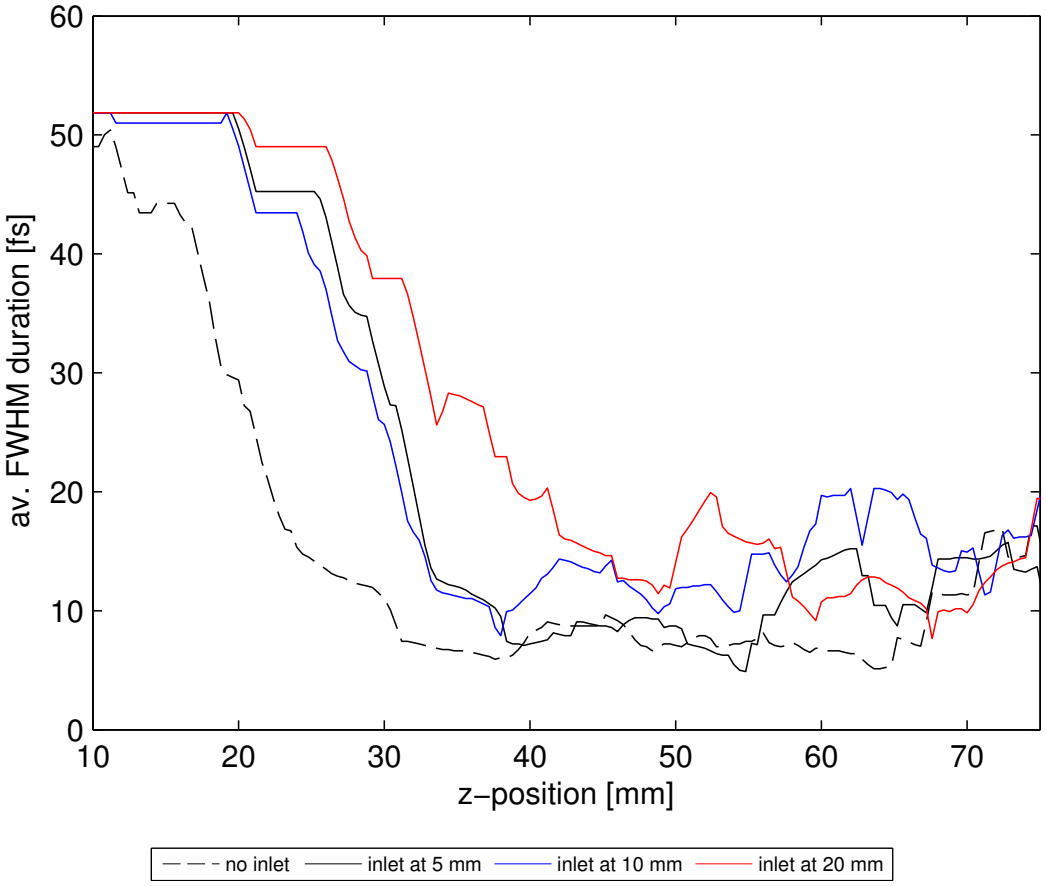

Figure 5.5: The optimisation procedure used to design a new fibre with enhanced phase-matching. Here the curves show the FWHM duration (averaged over 2.5 mm) of the first feature within the pulse with a field sufficiently stong to satisfy the semi-classical cut-off law for generating 30 nm XUV. The dashed curve is for a constant gas density of 150 mbar, and the inlet is then introduced and its location optimised to minimise the duration. The fibre is then terminated at this position.

that approaches its absorption limited value. In practice the positioning of this inlet was limited by fabrication capabilities and it was placed 3 mm from the exit of the fibre.

5.1.2.2 Synthesising an optimal driving pulse

The following procedure was taken to optimise the fibre design for enhanced phase-matching by driving HHG with a few-cycle pulse throughout an absorption limited length at the exit of the fibre. First, a high gas pressure of 150 mbar was selected so that the distance over which a few-cycle pulse needed to be maintained was minimised. Higher gas pressures were considered but extracting it from the various vacuum chambers becomes challenging, potentially leading to re-absorption. Next, MM-GNLSE simulations were performed for a long length of fibre and a large selection of inlet positions. The data

was then analysed to perform the optimisation. The FWHM duration (averaged over 2.5 mm of propagation) of the first feature with a sufficiently strong E-field to satisfy the semi-classical cut-off law for generating 30 nm XUV was plotted as a function of z-position. This was repeated for each inlet position and the plots were superimposed (Fig. 5.5) enabling the fibre to be terminated and an inlet position selected such that the duration is minimised at the exit.

From this optimisation procedure a 45 mm long fibre with a gas inlet positioned 5 mm from its entrance was selected. This combination was selected because of the short pulse in this region, the stability of the pulse duration and relative ease of manufacture. This compromise was an important one, as machining and mounting fibres with inlets positioned 3 mm or less from both ends was found to be very challenging.

5.1.3 Experiment and analysis

Once the design process was complete the 45 mm fibre with gas inlets positioned 5 mm from the entrance and 3 mm from the exit was fabricated using the methods outlined in chapter 3. As the gas inlets were so close to the fibre ends the X-ring method was used to seal the fibre inside the T-piece. This new assembly replaced the existing one in the gas-filled fibre beamline and $\sim$ 800 μJ pulses were coupled into the fibre using the same procedure as before. It was obvious by viewing the fluorescence and the far-field ring pattern that the propagation here was very different to the 70 mm fibre. The fluorescence extended towards the exit of the fibre and the far-field ring pattern was extensively broadened. These were both excellent indicators that the optimisation process had been successful, and the XUV beam was then allowed to pass through a pair of aluminium filters and into the chamber containing the diagnostic instruments.

5.1.3.1 XUV flux measurements

The first set of measurements taken were near-field images of the XUV beam. These are shown in Fig. 5.6 after 50 (a), 100 (b), 150 (c) and 200 (d) mbar of argon is allowed into the fibre core. As in chapter 3 the dark spots and speckle are damage and oil droplets on the surface of the detector, and the 5 mm aperture of the filters is clearly visible here giving an indication of the spot size. When compared to images taken of the XUV output of the 70 mm fibre an increase in counts of almost 2 orders of magnitude is observed. Also, at the higher pressures where the fibre design was optimised the spatial profile is far more uniform. This is in line with what one would expect when enhanced phase-matching is achieved, and an XUV beam of this quality would be ideal for applications in imaging.

Next, the XUV flux was calculated by back propagating through the filters (as described in chapter 3) and is plotted as a function of pressure in Fig. 5.7 (a). This shape is

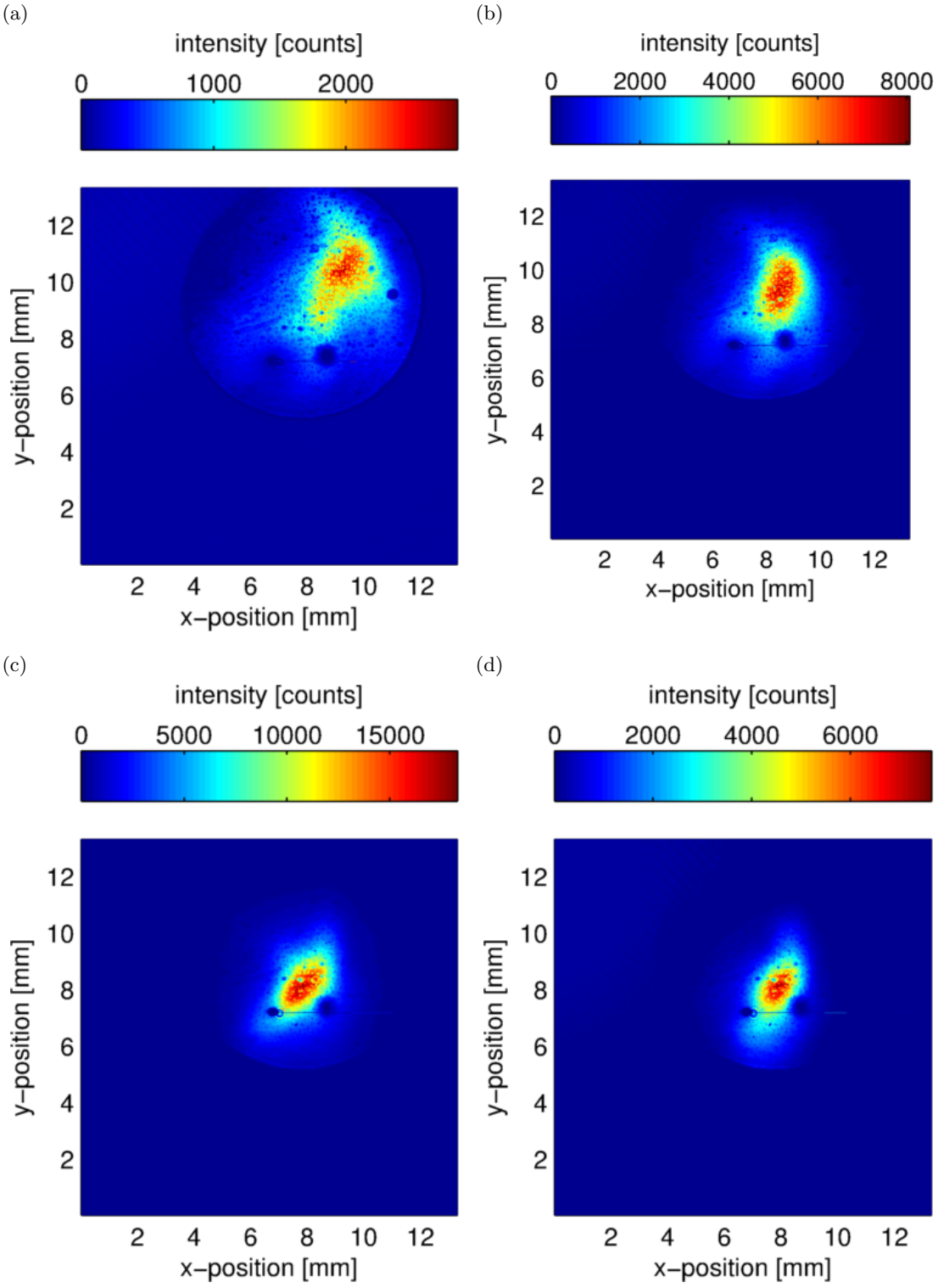

Figure 5.6: Near-field images of the XUV beam recorded with 50 (a), 100 (b), 150 (c) and (d) 200 mbar of argon injected into the core of the fibre. The beam has passed through a pair of aluminium filters and their 5 mm aperture is imprinted in the images.

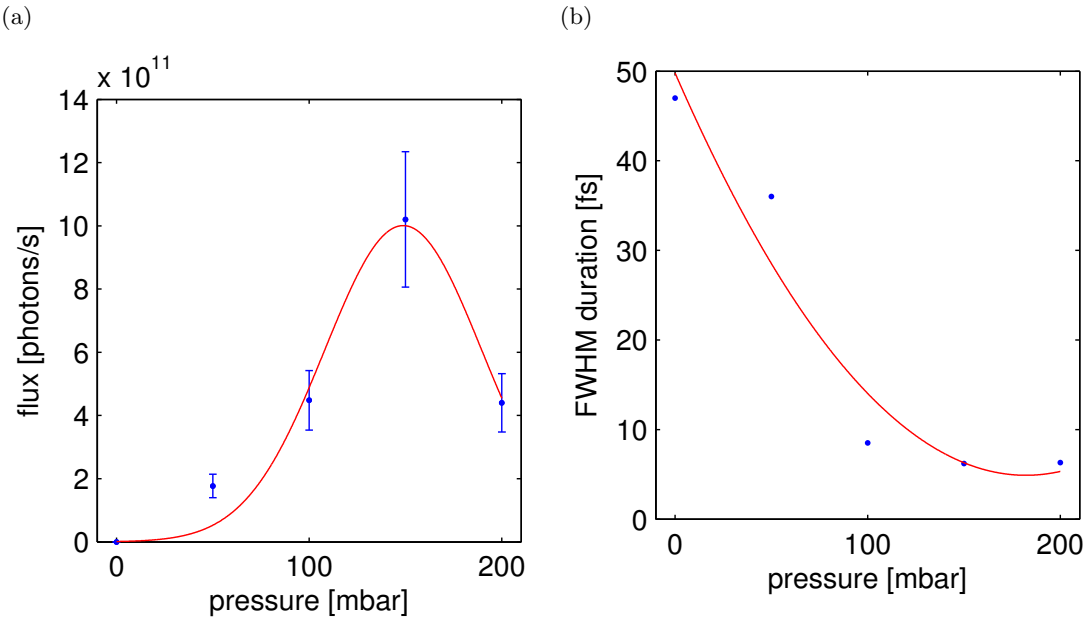

Figure 5.7: (a) The XUV flux exiting the fibre as a function of pressure. This was calculated from the CCD data, detector quantum efficiency and measured filter transmission. (b) The FWHM extracted from the optimisation as a function of the pressure. The maximum flux is found to coincide with the pressure at which the fibre design was optimised.

reminiscent of the pressure dependent phase-matching typically observed at low gas pressures. However in this case, phase-matching is enhanced by a reduced free electron density as the pressure approaches the value at which the design was optimised. This is confirmed in Fig. 5.7 (b) where the FWHM duration used in the optimisation is plotted as a function of gas pressure. The flux follows this curve nicely, and the deviation at the highest pressure is thought to be caused by re-absorption after the fibre as the vacuum pumps begin to struggle to remove the gas. Unfortunately, simulations of absolute flux were not possible at these wavelengths when working with argon as reliable absorption data was not available.

5.1.3.2 XUV Spectra

Once near-field data had been collected for photon counting purposes the X-ray CCD camera was moved out of the way and the XUV beam emerging from the fibre was allowed to illuminate the slit of the XUV spectrometer described in chapter 3. The recorded spectra are shown in Fig. 5.8 for argon pressures of 50 (a), 100 (b), 150 (c) and 200 (d) mbar. Note that the color axis has been manipulated to improve the contrast, and the spectral calibration of the instrument has been performed using a single absorption feature leading to an uncertainty of several nm in the wavelength axis. When compared to the spectra recoded with the 70 mm fibre (chapter 3) the most noticeable difference

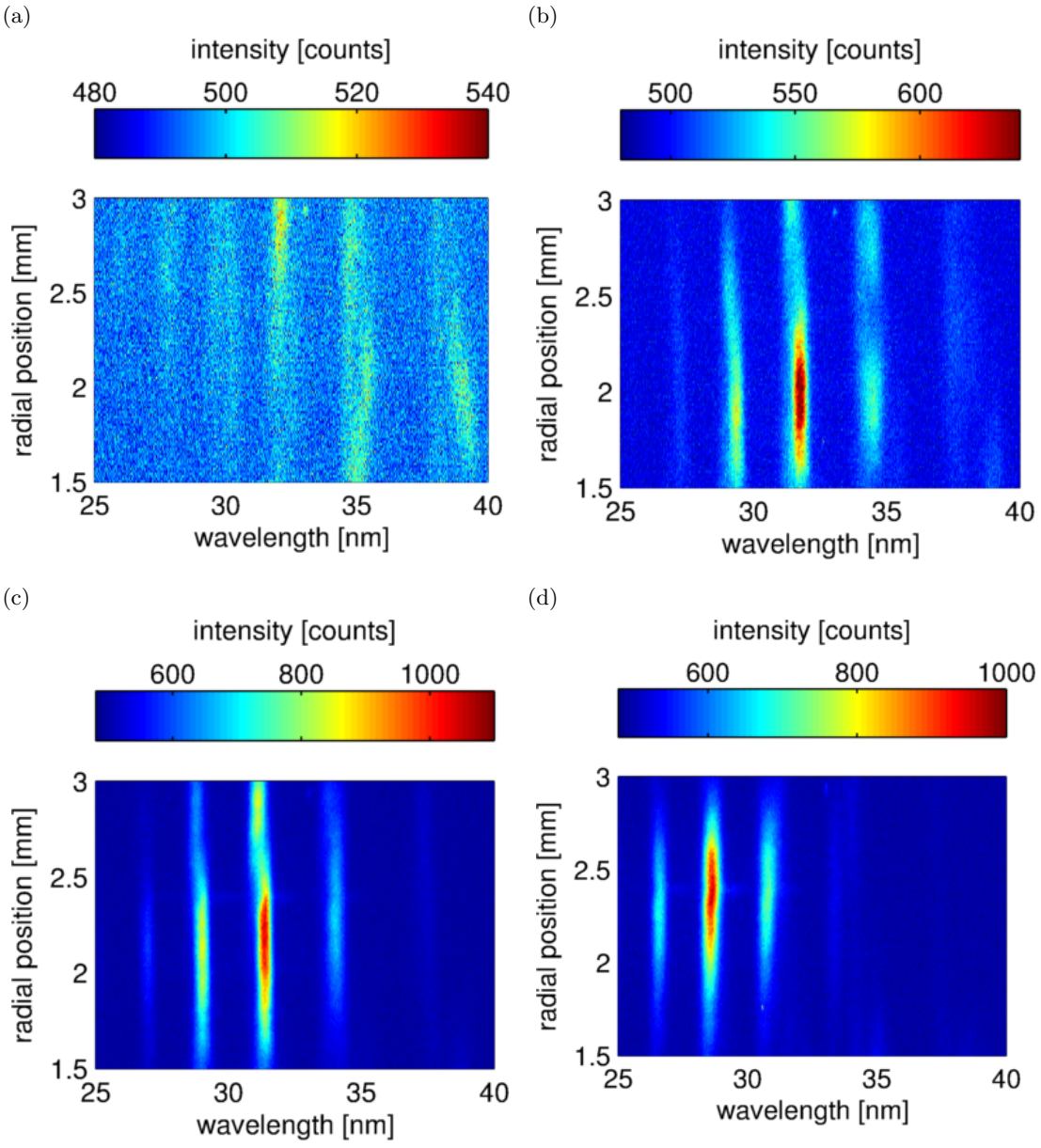

Figure 5.8: The XUV spectra recorded at 50 (a), 100 (b), 150 (c) and 200 (d) mbar. Unfortunatly, as only a single calibration point was availible and the central wavelength of the laser varies dynamically there is an uncertainty of several nm in the wavelength axis.

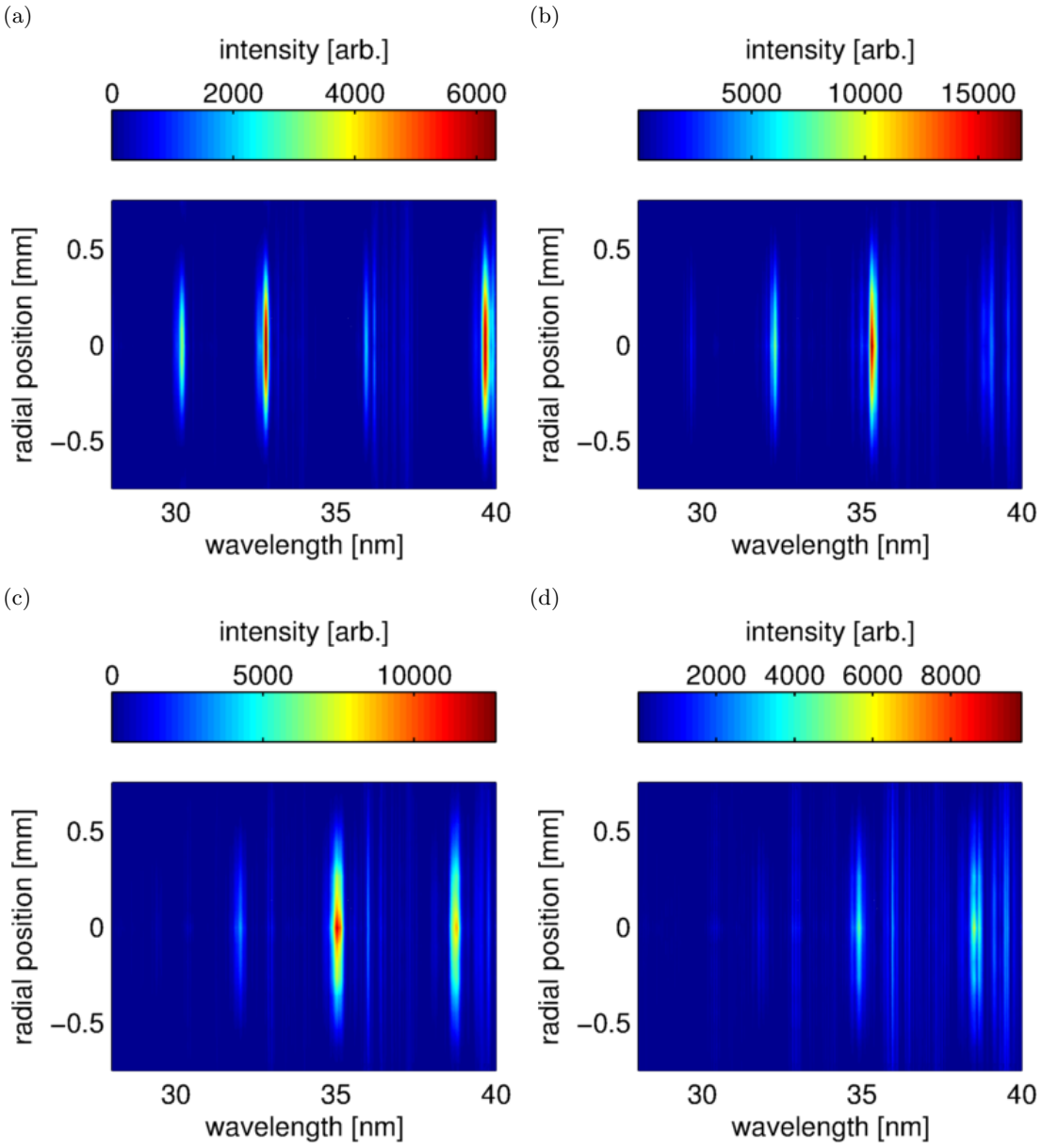

Figure 5.9: Spectra calculated using the UPPE-TDSE model for the same input parameters used in the experiment. Despite the weighting of the relative harmonics not being a perfect match, the reduction in interference between these and the earlier set of simulations is replicated. This is an expected outcome of the optimisation procedure.

is that the complex spectral structure is almost absent here. This is reproduced in the corresponding UPPE-TDSE simulations shown in Fig. 5.9, and the source of this change can be extracted from the optimisation procedure. The complex spectra were attributed to HHG being driven by two (or more) time delayed pulses. When selecting the length and gas inlet positions for the new fibre the stability of the optimised parameter was also considered. It turns out that such stability is an indicator of enhanced pulse contrast, and as a result interferences are minimised and the spectra take a more conventional form.

5.1.4 Figures of merit

Making comparisons between the flux of different HHG sources is complicated because of the vast array of driving lasers used throughout the community and the many possible figures of merit. From a source development viewpoint efficiency is of utmost importance, but the energy of the driving pulse must also be considered as multi-mJ lasers become increasingly expensive and typically have lower repetition rates, decreasing the flux per unit time.

As the range of XUV wavelengths generated within the new fibre is known the photon number extracted from the CCD images can be converted into an efficiency. This value is found to be $5 \pm 1 \times 10^{-6}$, which is ~ 8 times higher than for a similar configuration that is supposedly phase-matched [10]. When comparing this value to HHG sources based on an extended gas cell geometry (like the one developed at Artemis in chapter 3) the conversion efficiency is shown to be an order of magnitude higher [45]. In order to surpass the efficiency of this new source either very large focal volumes or energetic VIS/UV pulses are required [86, 74]. These geometries both use very high energy (10-100 mJ) NIR lasers to either drive a gas cell directly or to drive a harmonic generation module. This technology is not available to the vast majority of groups so optimised phase-matching via self-compression is the preferred choice at present.

5.2 Towards isolated attosecond pulses

When HHG is driven by a Gaussian few-cycle pulse the E-field is only sufficiently strong to generate the highest harmonic orders for half an optical cycle provided the carrier envelope phase (CEP) is optimised. This results in the harmonic structure being lost and an attosecond pulse isolated in time. This is demonstrated via a TDSE simulation in Fig. 5.10 where a 3 fs NIR Gaussian pulse with a peak intensity of 3×10^{14} W/cm^2 interacts with an individual argon atom. The harmonic spectrum is shown in Fig. 5.10 (a) and a high-pass filter is applied (dashed line) to the broad continuum spanning the cut-off region. Upon transformation to the time domain the XUV is found to be restricted to a single pulse with a duration of 350 as (Fig. 5.10 (b)). This is the standard

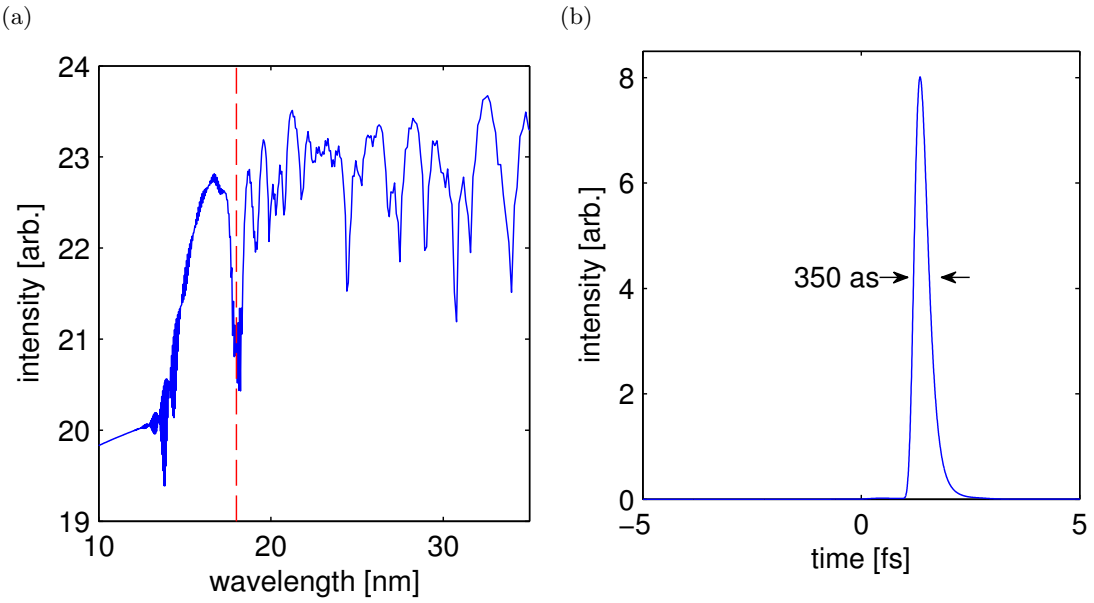

Figure 5.10: (a) The HH spectrum produced when a 3 fs NIR Gaussian pulse with a peak intensity of 3×10^{14} W/cm^2 interacts with an argon atom (calculated via the TDSE). (b) After applying a high-pass filter (dashed line in (a)) this is transformed into the time domain and the shortest wavelengths are found to be restricted to an isolated pulse with a FWHM duration of 350 as.

method for generating isolated attosecond pulses (IAPs) and the driving pulses are typically compressed to few-cycle durations within a conventional hollow fibre compressor apparatus [81].

Recently, simulations have been performed that predict isolated 560 as pulses may be generated in a low pressure region after a self-compressed filament [20]. This result is interesting, but realising it experimentally will be challenging as the optimised driving pulse will have to be extracted from the high pressure filament cell and delivered to the gas cell where HHG is performed without experiencing any reshaping. This is where the gas-filled fibre geometry developed in this thesis comes into its own, as the potential exists to perform the pulse compression and IAP generation within the same short fibre. Preliminary theoretical results are now discussed.

5.2.1 Optimal conditions for isolated attosecond pulses

Synthesising a driving pulse within the fibre that causes an IAP to emerge is a challenging process, and it is made more difficult by the extreme computational resources required by the model. Thankfully the major limiting factor was found to be the contrast of the driving pulse, so this could be optimised on its own prior to any further TDSE calculations. The procedure developed in the previous section is not appropriate here, as the contrast is rarely sufficient to completely suppress generation on the trailing edge

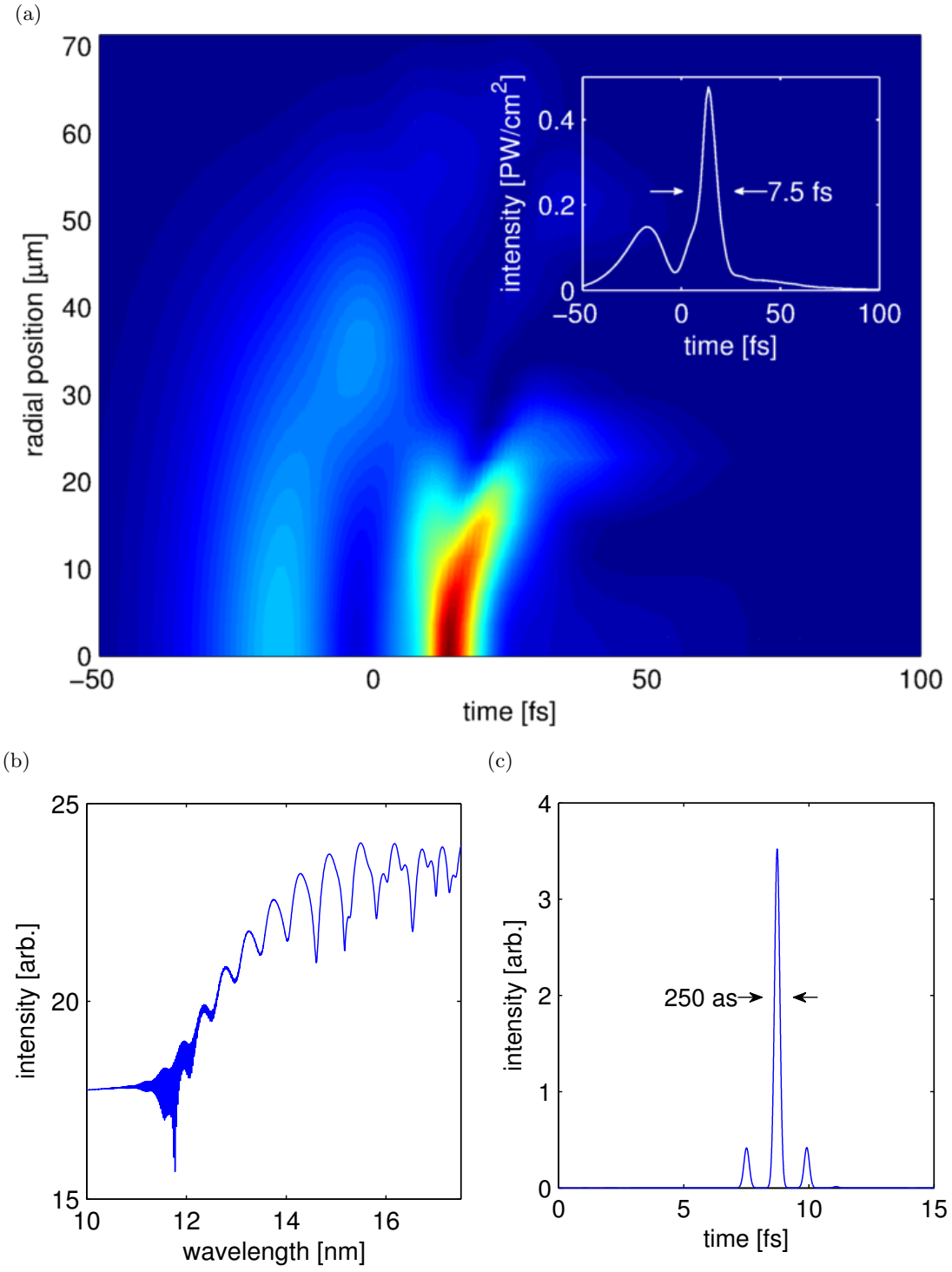

Figure 5.11: (a) The high contrast pulse synthesised within the fibre for the purpose of generating an isolated attosecond pulse. To achieve this the pulse energy was lowered to 600 μJ and the fibre was replaced with a 27.6 mm length uniformly filled with 200 mbar of argon. (b) The on-axis high harmonic spectrum calculated using the UPPE-TDSE model. (c) After propagating through a thin titanium filter a 250 as near-isolated pulse is found.

of the pulse. To overcome this the automated optimisation is replaced by a human one, and a pulse is propagated through a fibre for a given set of parameters and then studied as a function of z-position looking for a high contrast few-cycle pulse. One such pulse is shown in Fig. 5.11 (a). Here, the input pulse energy was lowered to 600 μJ and the 28 mm fibre is filled uniformly with 200 mbar of argon. These parameters were then used in the full UPPE-TDSE model and the on-axis HH spectrum is shown in Fig. 5.11 (b). The cut-off region begins to lose its harmonic structure, and when propagated through a thin titanium filter (note that filter dispersion has been neglected) a near-isolated XUV pulse with a duration of $\sim$ 250 as is the result. Note that the high frequency oscillations near the cut-off are not physical and are instead an artefact of a discrete time window.

5.3 Conclusions and outlook

For the final chapter of results the self-compression mechanism developed in the previous chapter was exploited to enhance the phase-matching of HHG at the exit of an argon-filled fibre. An optimisation procedure was developed, and the chosen fibre design consisted of a 45 mm length with gas inlets positioned 5 mm from the entrance and 3 mm from the exit respectively. This was fabricated and inserted into the gas-filled fibre beamline and flux measurements and XUV spectra were recorded at a series of pressures. The optimisation process was found to be very successful, and to my knowledge this fibre outperforms all XUV sources of this type developed to date.

Finally, the results of some preliminary UPPE-TDSE simulations were presented that suggest it should be possible to extract isolated attosecond pulses from these short fibres. This work is ongoing and a new optimisation procedure is being developed and CEP effects are being explored before commencing experimental work.

Chapter 6

Conclusions

The first key achievement of this thesis was the development of a sophisticated set of models capable of predicting both the propagation of the driving pulse and (if required) the HH output of the fibre. The latter is accomplished by de-coupling the driving field from the harmonics such that the calculation of the nonlinear polarization via the TDSE can be parallelised in both the radial and longitudinal coordinate. These models represent the cutting-edge of computational nonlinear optics, but there are still many features to add. These include the addition of a feedback step to improve the consistency of two medium response models, and the development of a new driving pulse propagation model that relaxes the requirement of a circular symmetry as interesting behaviour has been observed in the laboratory in this regime.

Next, the gas-filled fibre beamline at the University of Southampton was introduced. The procedures developed to process, mount and launch into a fibre were described in detail before discussing the results of a simple source characterisation experiment. While the flux measurements weren't particularly impressive, the XUV spectra recorded were found to be particularly interesting. These were then compared to UPPE-TDSE simulations and the complex spatial and spectral structure observed in the XUV beam could be attributed to the highly nonlinear propagation of the pump laser. The second source developed and characterised was a very different one of 13.5 nm XUV constructed at the Artemis facility. The first part of this experiment involved finding the optimum conditions for generating 13.5 nm XUV at the Artemis laser facility. Many parameters were explored including MIR and VIS driving wavelengths but the most efficient combination was found when focusing 2 mJ NIR pulses into a neon gas cell. For the second half of the experiment, thin film technology was developed to reject the residual driving laser, isolate a single harmonic at ~ 13.5 nm. Finally the beam was brought to a focus focal spot and when characterised this was found to be well suited to CXDI. Visiting scientists have started to use this apparatus to image test objects and biological samples. The next clear step in the source development work at both Southampton and Artemis is to use a fibre based source for CXDI on a daily basis. For this to be successful the pointing

stability of the laser will need to be enhanced and an entirely new mounting, launching and alignment strategy implemented.

In the penultimate piece of work the propagation of the driving pulse is studied in depth and a new mechanism is discovered to self-compress energetic many-cycle laser pulses to few cycle durations within short gas filled-fibres. The mechanism leads to pulse contrasts similar to those observed from filaments but at significantly lower gas pressures, enabling HHG to be performed within the compressor device itself. Spectrometer and SHG FROG measurements were recorded in the far-field, and once the exact initial conditions had been measured and replicated in the model an excellent match between theory and experiment was achieved. For the final part of this work novel wavelengths (VIS to MIR) and pulses delivered by high repetition rate fibre laser systems were explored. The compression mechanism can be extended to both of these regimes, but high fibre losses were found to become a limiting factor at long wavelengths and small core radii. In the future this will be addressed by replacing the simple capillary-type fibre with a Southampton fabricated microstructured fibre, where losses can be as much as three orders of magnitude lower. These fibres have now been incorporated into the MM-GNLSE and UPPE models and the impact of the low loss on the compression mechanism and HHG are being examined.

In the final chapter the new self-compression mechanism was used to optimise the characteristics of the harmonic field generated in-situ. First, an optimisation procedure was developed to the enhance phase-matching by maintaining a few-cycle driving pulse throughout the fibres exit. The chosen design consisted of a 45 mm length of fibre with gas inlets positioned 5 mm from the entrance and 3 mm from the exit respectively. Such a fibre was processed and positioned in the gas-filled fibre beamline and flux measurements and XUV spectra were recorded at a series of pressures. The optimisation procedure was very successful and to my knowledge this is the brightest source of its type developed to date. The thesis is then concluded with some fascinating UPPE-TDSE simulations that suggest it may be possible to extract isolated attosecond pulses from these short fibres. This work is ongoing and CEP effects are being explored before designing any experiments.

Appendix A

FROG traces

The following figures contain the measured and reconstructed SHG FROG traces obtained in the GRENOUILLE and FROG experiments described in chapter 4. Fig. A.1 shows the traces used to produce Fig. 4.10 (b) and (c). Fig. A.2 then presents the traces used to produce Fig. 4.13 (a), (c) and (e).

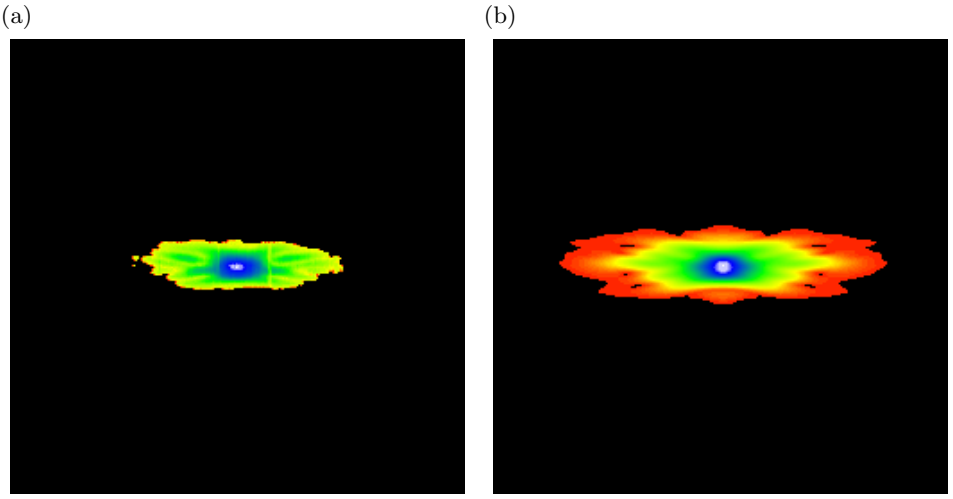

Figure A.1: The measured (a) and reconstructed (b) GRENOUILLE trace analysed to produce Fig. 4.10 (b) and (c). The retrieval error here is 0.00995.

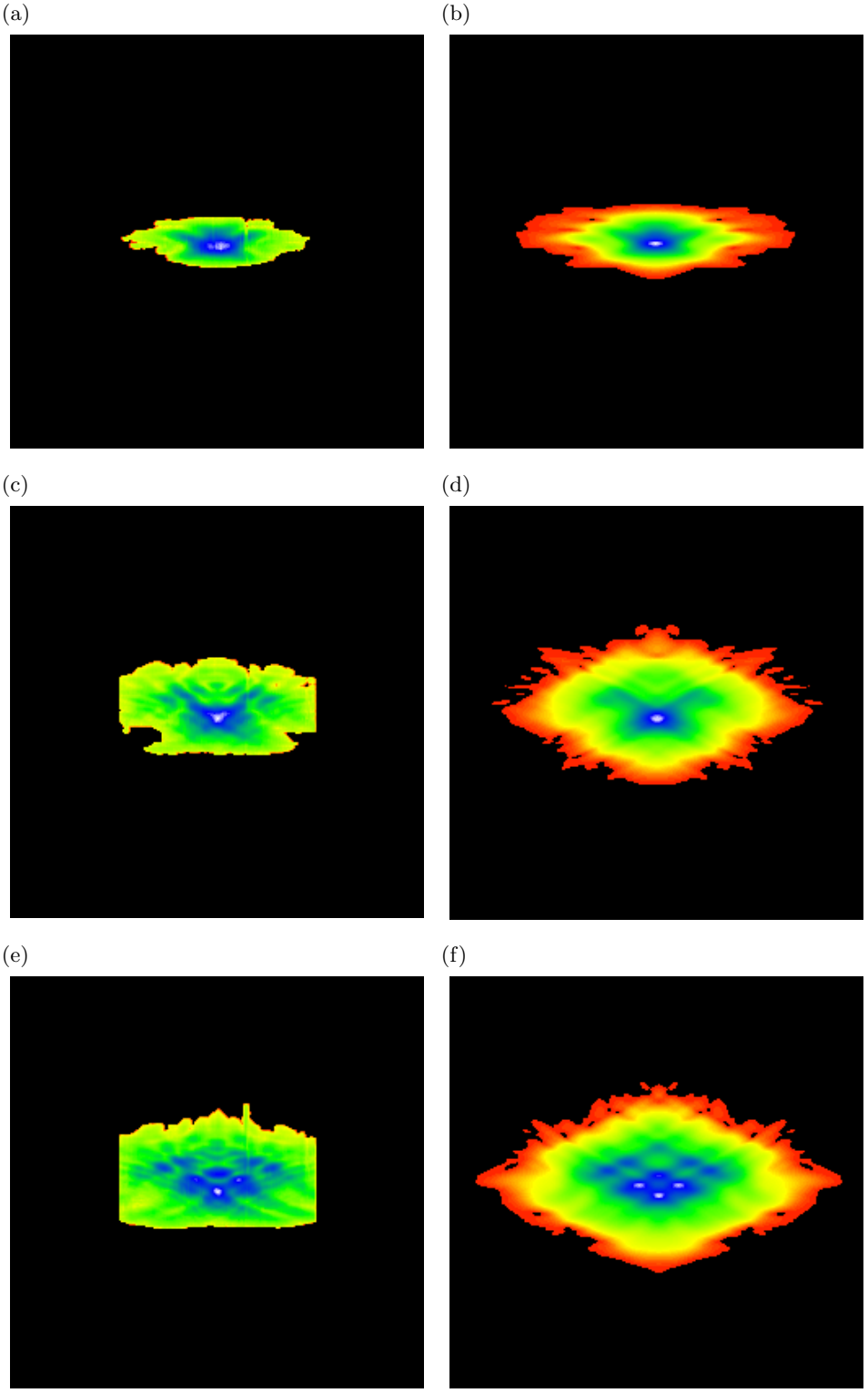

Figure A.2: The measured (a, c and e) and reconstructed (b, d and f) SHG FROG traces used to produce Fig. 4.13 (a), (c) and (e). The retrieval errors at the 3 input energies are 0.01004, 0.01973 and 0.0258.

References

[1] S. Akturk, C. L. Arnold, B. Zhou, and A. Mysyrowicz. High-energy ultrashort laser pulse compression in hollow planar waveguides. *Optics Letters*, 34(9):1462–1464, 2009.

[2] P. N. Anderson. https://github.com/patrickanderson1/XNLO. 2015.

[3] P. N. Anderson, T. J. Butcher, P. Horak, J. G. Frey, and W. S. Brocklesby. Experimental demonstration of a high-flux capillary based XUV source in the high ionisation regime. *Intense field, Short Wavelength Atomic and Molecular Processes (I-SWAMP)*, 2011.

[4] P. N. Anderson, T. J. Butcher, P. Horak, J. G. Frey, and W. S. Brocklesby. High-flux capillary based XUV source via the direct engineering of a laser induced ionization profile. *CLEO-Europe/IQEC*, 2011.

[5] P. N. Anderson, T. J. Butcher, P. Horak, J. G. Frey, and W. S. Brocklesby. Few-cycle self-compression via multimode nonlinear optics in gas filled waveguides. *CLEO/QELS*, 2012.

[6] P. N. Anderson, P. Horak, J. G. Frey, and W. S. Brocklesby. Isolated attosecond pulses by self-compression in short gas-filled fibers. *CLEO-Europe/IQEC*, 2013.

[7] P. N. Anderson, P. Horak, J. G. Frey, and W. S. Brocklesby. High-energy laser-pulse self-compression in short gas-filled fibers. *Physical Review A*, 89(1):013819, 2014.

[8] J. Andreasen and M. Kolesik. Midinfrared femtosecond laser pulse filamentation in hollow waveguides: A comparison of simulation methods. *Physical Review E*, 87(5):053303, 2013.

[9] P. Arpin, T. Popmintchev, N. L. Wagner, A. L. Lytle, O. Cohen, H. C. Kapteyn, and M. M. Murnane. Enhanced high harmonic generation from multiply ionized argon above 500 eV through laser pulse self-compression. *Physical Review Letters*, 103(14):143901, 2009.

[10] R. A. Bartels, A. Paul, H. Green, H. C. Kapteyn, M. M. Murnane, S. Backus, I. P. Christov, Y. Liu, D. Attwood, and C. Jacobsen. Generation of spatially coherent light at extreme ultraviolet wavelengths. *Science*, 297:376–378, 2002.

[11] L. Bergé, S. Skupin, F. Lederer, G. Méjean, J. Yu, J. Kasparian, E. Salmon, J. P. Wolf, M. Rodriguez, L. Wöste, R. Bourayou, and R. Sauerbrey. Multiple filamentation of terawatt laser pulses in air. *Physical Review Letters*, 92(22):225002, 2004.

[12] B. Bernhardt, A. Ozawa, A. Vernaleken, I. Pupeza, J. Kaster, Y. Kobayashi, R. Holzwarth, E. Fill, F. Krausz, T. W. Hänsch, and T. Udem. Vacuum ultraviolet frequency combs generated by a femtosecond enhancement cavity in the visible. *Optics Letters*, 37(4):503–505, 2012.

[13] A. Bideau-Mehu, Y. Guern, R. Abjean, and A. Johannin-Gilles. Measurement of refractive indices of neon, argon, krypton and xenon in the 253.7140.4 nm wavelength range. Dispersion relations and estimated oscillator strengths of the resonance lines. *Journal of Quantitative Spectroscopy and Radiative Transfer*, 25(5):395–402, 1981.

[14] S. Bohman, A. Suda, T. Kanai, S. Yamaguchi, and K. Midorikawa. Generation of 5.0 fs, 5.0 mJ pulses at 1kHz using hollow-fiber pulse compression. *Optics Letters*, 35(11):1887–1889, 2010.

[15] P. Bowlan, P. Gabolde, and R. Trebino. Directly measuring the spatio-temporal electric field of focusing ultrashort pulses. *Optics Express*, 15(16):10219–10230, 2007.

[16] R. W. Boyd. *Nonlinear optics*. Academic Press, Burlington, 2nd edition, 2008.

[17] J. M. Brown, A. Lotti, A. Teleki, and M. Kolesik. Exactly solvable model for nonlinear light-matter interaction in an arbitrary time-dependent field. *Physical Review A*, 84(6):063424, 2011.

[18] T. J. Butcher, P. N. Anderson, R. T. Chapman, P. Horak, J. G. Frey, and W. S. Brocklesby. Bright extreme-ultraviolet high-order-harmonic radiation from optimized pulse compression in short hollow waveguides. *Physical Review A*, 87(4):043822, 2013.

[19] T. J. Butcher, P. N. Anderson, P. Horak, J. G. Frey, and W. S. Brocklesby. High intensity pulse self- compression in short hollow core capillaries. *CLEO-Europe/IQEC*, 2011.

[20] H. S. Chakraborty, M. B. Gaarde, and A. Couairon. Single attosecond pulses from high harmonics driven by self-compressed filaments. *Optics Letters*, 31(24):3662–3664, 2006.

[21] R. T. Chapman, T. J. Butcher, P. Horak, F. Poletti, J. G. Frey, and W. S. Brocklesby. Modal effects on pump-pulse propagation in an Ar-filled capillary. *Optics Express*, 18(12):13279–13284, 2010.

[22] I. P. Christov. Control of high harmonic and attosecond pulse generation in aperiodic modulated waveguides. *Journal of the Optical Society of America B*, 18(12):1877–1881, 2001.

[23] E. Constant, D. Garzella, P. Breger, E. Mével, C. Dorrer, C. Le Blanc, F. Salin, and P. Agostini. Optimizing high harmonic generation in absorbing gases: model and experiment. *Physical Review Letters*, 82(8):1668–1671, 1999.

[24] P. B. Corkum. Plasma perspective on strong-field multiphoton ionization. *Physical Review Letters*, 71(13):1994–1997, 1993.

[25] A. Couairon, E. Brambilla, T. Corti, D. Majus, O. J. Ramírez-Góngora, and M. Kolesik. Practitioners guide to laser pulse propagation models and simulation. *The European Physical Journal Special Topics*, 199:5–76, 2011.

[26] A. Couairon and A. Mysyrowicz. Femtosecond filamentation in transparent media. *Physics Reports*, 441:47–189, 2007.

[27] F. Couny, F. Benabid, and P. S. Light. Large-pitch kagome-structured hollow-core photonic crystal fiber. *Optics Letters*, 31(24):3574–3576, 2006.

[28] C. Courtois, A. Couairon, B. Cros, J. R. Marques, and G. Matthieussent. Propagation of intense ultrashort laser pulses in a plasma filled capillary tube: Simulations and experiments. *Physics of Plasmas*, 8(7):3445–3456, 2001.

[29] R. F. Cregan, B. J. Mangan, J. C. Knight, T. A. Birks, P. S. J. Russell, P. J. Roberts, and D. C. Allan. Single-mode photonic band gap guidance of light in air. *Science*, 285:1537–1539, 1999.

[30] CXRO. http://henke.lbl.gov/optical_constants/. 2014.

[31] J. C. Dainty and J. R. Fienup. Phase Retrieval and Image Reconstruction for Astronomy. In *Image Recovery: Theory and Application*, pages 231–275. 1987.

[32] P. L. DeVries and J. Hasbun. *A first course in computational physics*. Jones and Bartlett, Sudbury, 2nd edition, 2011.

[33] C. Dorrer, E. M. Kosik, and I. A. Walmsley. Direct space time-characterization of the electric fields of ultrashort optical pulses. *Optics Letters*, 27(7):548–550, 2002.

[34] M. Drescher, M. Hentschel, R. Kienberger, G. Tempea, C. Spielmann, G. A. Reider, P. B. Corkum, and F. Krausz. X-ray pulses approaching the attosecond frontier. *Science*, 291:1923–1927, 2001.

[35] ELI. http://www.eli-laser.eu/. 2014.

[36] E. L. Falcao-Filho, C. Lai, K. Hong, V. Gkortsas, S. Huang, L. Chen, and F. X. Kartner. Scaling of high-order harmonic efficiencies with visible wavelength drivers: A route to efficient extreme ultraviolet sources. *Applied Physics Letters*, 97(6):061107, 2010.

[37] M. Ferray, A. L. L'Huillier, X. F. Li, L. A. Lompre, G. Mainfray, and C. Manus. Multiple-harmonic conversion of 1064 nm radiation in rare gases. *Journal of Physics B: Atomic, Molecular and Optical Physics*, 21:31–35, 1988.

[38] J. R. Fienup. Phase retrieval algorithms: a comparison. *Applied Optics*, 21(15):2758–2769, 1982.

[39] C. A. Froud, R. T. Chapman, E. T. F. Rogers, M. Praeger, B. Mills, J. Grant-Jacob, T. J. Butcher, S. L. Stebbings, A. M. de Paula, J. G. Frey, and W. S. Brocklesby. Spatially resolved Ar * and Ar +* imaging as a diagnostic for capillary-based high harmonic generation. *Journal of Optics A: Pure and Applied Optics*, 11:054011, 2009.

[40] M. B. Gaarde and K. J. Schafer. Quantum path distributions for high-order harmonics in rare gas atoms. *Physical Review A*, 65(3):031406, 2002.

[41] F. Gérôme, R. Jamier, J. Auguste, G. Humbert, and J. Blondy. Simplified hollow-core photonic crystal fiber. *Optics Letters*, 35(8):1157–1159, 2010.

[42] E. A. Gibson, A. Paul, N. Wagner, R. Tobey, D. Gaudiosi, S. Backus, I. P. Christov, A. Aquila, E. M. Gullikson, D. T. Attwood, M. M. Murnane, and H. C. Kapteyn. Coherent soft x-ray generation in the water window with quasi-phase matching. *Science*, 302:95–98, 2003.

[43] B. L. Henke, E. M. Gullikson, and J. C. Davis. X-ray interactions: photoabsorption, scattering, transmission, and reflection at E = 50-30,000 eV, Z = 1-92. *Atomic Data and Nuclear Data Tables*, 54(2):181–342, 1993.

[44] M. Hentschel, R. Kienberger, C. Spielmann, G. A. Reider, N. Milosevic, T. Brabec, P. Corkum, U. Heinzmann, M. Drescher, and F. Krausz. Attosecond metrology. *Nature*, 414:509–513, 2001.

[45] J.-F. Hergott, M. Kovacev, H. Merdji, C. Hubert, Y. Mairesse, E. Jean, P. Breger, P. Agostini, B. Carré, and P. Salières. Extreme-ultraviolet high-order harmonic pulses in the microjoule range. *Physical Review A*, 66(2):021801, 2002.

[46] P. Horak, P. N. Anderson, T. J. Butcher, J. G. Frey, and W. S. Brocklesby. High-power laser pulse compression for optimized high-harmonic generation in short hollow fibers. *PIERS*, 2013.

[47] P. Horak and F. Poletti. Multimode nonlinear fibre optics: theory and applications. In M. Yasin, S. W. Harun, and H. Arof, editors, *Recent Progress in Optical Fiber Research*, pages 3–25. Intech, 2012.

[48] L. V. Keldysh. Ionization in the field of a strong electromagnatic wave. *Soviet Physics JETP*, 20(5):1307–1314, 1965.

[49] V. G. Kohn. On the theory of reflectivity by an x-ray multilayer mirror. *Physica Status Solidi (B)*, 187:61–70, 1995.

[50] M. Kolesik, P. Jakobsen, and J. V. Moloney. Quantifying the limits of unidirectional ultrashort optical pulse propagation. *Physical Review A*, 86(3):035801, 2012.

[51] M. Kolesik and J. V. Moloney. Nonlinear optical pulse propagation simulation: From Maxwell's to unidirectional equations. *Physical Review E*, 70(3):36604, 2004.

[52] M. Kolesik and J. V. Moloney. Modeling and simulation techniques in extreme nonlinear optics of gaseous and condensed media. *Reports on Progress in Physics*, 77:016401, 2013.

[53] M. Kolesik, E. M. Wright, and J. V. Moloney. Simulation of femtosecond pulse propagation in sub-micron diameter tapered fibers. *Applied Physics B*, 79:293–300, 2004.

[54] J. L. Krause, K. J. Schafer, and K. C. Kulander. High-order harmonic generation from atoms and ions in the high intensity regime. *Physical Review Letters*, 68(24):3535–3538, 1992.

[55] H. R. Lange, J. F. Ripoche, A. A. Chiron, B. Lamouroux, M. A. Franco, B. Prade, E. T. J. Nibbering, and A. Mysyrowicz. Time-space self-compression of femtosecond laser pulse in air. *CLEO/IQEC*, 1998.

[56] M. Lewenstein, P. Balcou, M. Y. Ivanov, A. L. Huillier, and P. B. Corkum. Theory of high-harmonic generation by low-frequency laser fields. *Physical Review A*, 49(3):2117–2132, 1994.

[57] F. Lindner, G. G. Paulus, H. Walther, A. Baltuška, E. Goulielmakis, M. Lezius, and F. Krausz. Gouy phase shift for few-cycle laser pulses. *Physical Review Letters*, 92(11):113001, 2004.

[58] L. Z. Liu, K. O'Keeffe, and S. M. Hooker. Quasi-phase-matching of high-order-harmonic generation using polarization beating in optical waveguides. *Physical Review A*, 85(5):053823, 2012.

[59] E. Lorin, S. Chelkowski, and A. Bandrauk. A numerical MaxwellSchrödinger model for intense lasermatter interaction and propagation. *Computer Physics Communications*, 177:908–932, 2007.

[60] T. H. Maiman. Stimulated optical radiation in ruby. *Nature*, 187:493 – 494, 1960.

[61] E. A. J. Marcatili and R. A. Schmeltzer. Hollow metallic and dielectric waveguides for long distance optical transmission and lasers. *The Bell Sysyem Technical Journal*, 43:1783–1809, 1964.

[62] S. Marchesini, H. He, H. N. Chapman, S. P. Hau-Riege, A. Noy, M. R. Howells, U. Weierstall, and J. C. H. Spence. X-ray image reconstruction from a diffraction pattern alone. *Physical Review B*, 68(14):140101, 2003.

[63] J. Miao, P. Charalambous, J. Kirz, and D. Sayre. Extending the methodology of X-ray crystallography to allow imaging of micrometre-sized non-crystalline specimens. *Nature*, 400:342–344, 1999.

[64] M. Nisoli, S. De Silvestri, and O. Svelto. Generation of high energy 10 fs pulses by a new pulse compression technique. *Applied Physics Letters*, 68(20):2793–2795, 1996.

[65] R. K. Nubling and J. A. Harrington. Launch conditions and mode coupling in hollow-glass waveguides. *Optical Engineering*, 37(9):2454–2458, 1998.

[66] M. Nurhuda, A. Suda, S. Bohman, S. Yamaguchi, and K. Midorikawa. Optical pulse compression of ultrashort laser pulses in an argon-filled planar waveguide. *Physical Review Letters*, 97(15):153902, 2006.

[67] P. O'Shea, M. Kimmel, X. Gu, and R. Trebino. Highly simplified device for ultrashort-pulse measurement. *Optics Letters*, 26(12):932–934, 2001.

[68] P. OShea, S. Akturk, M. Kimmel, and R. Trebino. Practical issues in ultra-short-pulse measurements with GRENOUILLE. *Applied Physics B*, 79:683–691, 2004.

[69] A. Paul, R. A. Bartels, R. Tobey, H. Green, S. Weiman, I. P. Christov, M. M. Murnane, H. C. Kapteyn, and S. Backus. Quasi-phase-matched generation of coherent extreme-ultraviolet light. *Nature*, 421:51–54, 2003.

[70] B. C. Platt and R. Shack. History and principles of shack-hartmann wavefront sensing. *Journal of Refractive Surgery*, 17:573–577, 2001.

[71] F. Poletti, J. R. Hayes, and D. J. Richardson. Optimising the performances of hollow antiresonant fibres. *ECOC*, 2011.

[72] F. Poletti and P. Horak. Description of ultrashort pulse propagation in multimode optical fibers. *Journal of the Optical Society of America B*, 25(10):1645–1654, 2008.

[73] P. Polynkin, M. Kolesik, E. M. Wright, and J. V. Moloney. Experimental tests of the new paradigm for laser filamentation in gases. *Physical Review Letters*, 106(15):153902, 2011.

[74] D. Popmintchev, M. Chen, C. Hernández-garcía, J. A. Pérez-hernández, S. Brown, F. Dollar, P. Grytchtol, B. Walker, L. Plaja, M. M. Murnane, H. C. Kapteyn, and T. Popmintchev. Ultrahigh-efficiency high harmonic generation driven by UV lasers. *CLEO/QELS*, 2013.

[75] T. Popmintchev, M. Chen, D. Popmintchev, P. Arpin, S. Brown, S. Alisauskas, G. Andriukaitis, T. Balciunas, O. D. Mücke, A. Pugzlys, A. Baltuska, B. Shim, S. E. Schrauth, A. Gaeta, C. Hernández-García, L. Plaja, A. Becker, A. Jaron-Becker, M. M. Murnane, and H. C. Kapteyn. Bright coherent ultrahigh harmonics in the keV x-ray regime from mid-infrared femtosecond lasers. *Science*, 336:1287–1291, 2012.

[76] V. S. Popov. Tunnel and multiphoton ionization of atoms and ions in a strong laser field (Keldysh theory). *Physics-Uspekhi*, 47(9):855–885, 2004.

[77] J. Primot and L. Sogno. Achromatic three-wave (or more) lateral shearing interferometer. *Journal of the Optical Society of America A*, 12(12):2679–2685, 1995.

[78] S. C. Rae, X. Chen, and K. Burnett. Saturation of harmonic generation in one- and three-dimensional atoms. *Physical Review A*, 50(2):1946–1949, 1994.

[79] A. Rundquist, C. G. Durfee, Z. Chang, C. Herne, S. Backus, M. M. Murnane, and H. C. Kapteyn. Phase-matched generation of coherent soft x-rays. *Science*, 280:1412–1415, 1998.

[80] R. L. Sandberg, A. Paul, D. A. Raymondson, S. Hädrich, D. M. Gaudiosi, J. Holtsnider, R. I. Tobey, O. Cohen, M. M. Murnane, H. C. Kapteyn, C. Song, J. Miao, Y. Liu, and F. Salmassi. Lensless diffractive imaging using tabletop coherent high-harmonic soft-x-ray beams. *Physical Review Letters*, 99(9):098103, 2007.

[81] G. Sansone, E. Benedetti, F. Calegari, C. Vozzi, L. Avaldi, R. Flammini, L. Poletto, P. Villoresi, C. Altucci, R. Velotta, S. Stagira, S. De Silvestri, and M. Nisoli. Isolated single-cycle attosecond pulses. *Science*, 314:443–446, 2006.

[82] G. Sansone, F. Kelkensberg, J. F. Pérez-Torres, F. Morales, M. F. Kling, W. Siu, O. Ghafur, P. Johnsson, M. Swoboda, E. Benedetti, F. Ferrari, F. Lépine, J. L. Sanz-Vicario, S. Zherebtsov, I. Znakovskaya, A. L'huillier, M. Y. Ivanov, M. Nisoli, F. Martín, and M. J. J. Vrakking. Electron localization following attosecond molecular photoionization. *Nature*, 465:763–766, 2010.

[83] B. Shim, S. E. Schrauth, and A. L. Gaeta. Filamentation in air with ultrashort mid-infrared pulses. *Optics Express*, 19(10):9118–9126, 2011.

[84] G. Stibenz, N. Zhavoronkov, and G. Steinmeyer. Self-compression of millijoule pulses to 7.8 fs duration in a white-light filament. *Optics Letters*, 31(2):274–276, 2006.

[85] D. Strickland and G. Mourou. Compression of amplified chirped optical pulses. *Optics Communications*, 56(3):219–221, 1985.

[86] E. Takahashi, Y. Nabekawa, and K. Midorikawa. Generation of 10- microJ coherent extreme-ultraviolet light by use of high-order harmonics. *Optics Letters*, 27(21):1920–1922, 2002.

[87] G. Tempea and T. Brabec. Theory of self-focusing in a hollow waveguide. *Optics Letters*, 23(10):762–764, 1998.

[88] R. Torres, T. Siegel, L. Brugnera, I. Procino, J. G. Underwood, C. Altucci, R. Velotta, E. Springate, C. Froud, I. C. E. Turcu, S. Patchkovskii, M. Y. Ivanov, O. Smirnova, and J. P. Marangos. Revealing molecular structure and dynamics through high-order harmonic generation driven by mid-IR fields. *Physical Review A*, 81(5):051802, 2010.

[89] R. Trebino, K. W. DeLong, D. N. Fittinghoff, J. N. Sweetser, M. A. Krumbugel, B. A. Richman, and D. J. Kane. Measuring ultrashort laser pulses in the time-frequency domain using frequency-resolved optical gating. *Review of Scientific Instruments*, 68(9):3277–3295, 1997.

[90] N. L. Wagner, E. A. Gibson, T. Popmintchev, I. P. Christov, M. Murnane, M, and H. C. Kapteyn. Self-compression of ultrashort pulses through ionization-induced spatiotemporal reshaping. *Physical Review Letters*, 93(17):173902, 2004.

[91] T. Witting, F. Frank, W. A. Okell, C. A. Arrell, J. P. Marangos, and J. W. G. Tisch. Sub-4-fs laser pulse characterization by spatially resolved spectral shearing interferometry and attosecond streaking. *Journal of Physics B: Atomic, Molecular and Optical Physics*, 45:074014, 2012.

[92] M. Zepf, B. Dromey, M. Landreman, P. Foster, and S. M. Hooker. Bright quasi-phase-matched soft-x-ray harmonic radiation from argon ions. *Physical Review Letters*, 99(14):143901, 2007.

[93] X. Zhang, A. L. Lytle, T. Popmintchev, X. Zhou, H. C. Kapteyn, M. M. Murnane, and O. Cohen. Quasi-phase-matching and quantum-path control of high-harmonic generation using counterpropagating light. *Nature Physics*, 3:270–275, 2007.

[94] K. Zhao, Q. Zhang, M. Chini, Y. Wu, X. Wang, and Z. Chang. Tailoring a 67 attosecond pulse through advantageous phase-mismatch. *Optics Letters*, 37(18):3891–3893, 2012.